# Reflection signatures in bright Seyfert 1 galaxies observed with Suzaku and NuSTAR

**Giulia Mantovani**

München 2016

# Reflection signatures in bright Seyfert 1 galaxies observed with Suzaku and NuSTAR

**Giulia Mantovani**

Dissertation
an der Fakultät für Physik
der Ludwig–Maximilians–Universität
München

vorgelegt von
Giulia Mantovani
aus Rom, Italien

München, den 01.06.2016

Erstgutachter: Prof. Dr. Kirpal Nandra
Zweitgutachter: Prof. Dr. Andreas Burkert
Tag der mündlichen Prüfung: 13.07.2016

# Contents

**Zusammenfassung** **xi**

**Abstract** **xiv**

**1 Introduction** **1**

1.1 Active Galactic Nuclei . . . . . . . . . . . . . . . . . . . . . . . . . . . 1
  1.1.1 Black hole mass estimation . . . . . . . . . . . . . . . . . . . . . 2
1.2 Accretion Physics . . . . . . . . . . . . . . . . . . . . . . . . . . . . . . 4
  1.2.1 Standard Model . . . . . . . . . . . . . . . . . . . . . . . . . . . 5
1.3 Unified Model for Seyfert Galaxies . . . . . . . . . . . . . . . . . . . . 8
  1.3.1 Observational Evidences of Seyfert Galaxies . . . . . . . . . . . . 8
  1.3.2 Unified Model . . . . . . . . . . . . . . . . . . . . . . . . . . . . 8
1.4 X-ray emission from AGN . . . . . . . . . . . . . . . . . . . . . . . . . 10
1.5 Reflection Spectrum . . . . . . . . . . . . . . . . . . . . . . . . . . . . 11
  1.5.1 Relativistic Effects . . . . . . . . . . . . . . . . . . . . . . . . . 18
  1.5.2 The Effects of Gravitational Light Bending . . . . . . . . . . . . . 22
1.6 This thesis . . . . . . . . . . . . . . . . . . . . . . . . . . . . . . . . . 23

**2 Data Reduction** **25**

2.1 Introduction . . . . . . . . . . . . . . . . . . . . . . . . . . . . . . . . . 25
2.2 Suzaku . . . . . . . . . . . . . . . . . . . . . . . . . . . . . . . . . . . . 25
  2.2.1 Overview . . . . . . . . . . . . . . . . . . . . . . . . . . . . . . . 25
  2.2.2 X-ray Telescope (XRT) . . . . . . . . . . . . . . . . . . . . . . . 26
  2.2.3 X-ray Imaging Spectrometer (XIS) . . . . . . . . . . . . . . . . . 27
  2.2.4 Hard X-ray Detector (HXD) . . . . . . . . . . . . . . . . . . . . . 30
2.3 *Suzaku* Data Reduction . . . . . . . . . . . . . . . . . . . . . . . . . . 32
2.4 *NuSTAR* . . . . . . . . . . . . . . . . . . . . . . . . . . . . . . . . . . 34
  2.4.1 Optics . . . . . . . . . . . . . . . . . . . . . . . . . . . . . . . . 35
  2.4.2 Detectors . . . . . . . . . . . . . . . . . . . . . . . . . . . . . . 36
2.5 *NuSTAR* Data Reduction . . . . . . . . . . . . . . . . . . . . . . . . . 37

**3 Relativistic Reflection Signature in IC 4329A 39**
3.1 Introduction . . . . . . . . 39
3.1.1 IC 4329A . . . . . . . . 39
3.2 Data Analysis . . . . . . . . 41
3.2.1 Baseline Model . . . . . . . . 42
3.2.2 Line models . . . . . . . . 43
3.2.3 Reflection model . . . . . . . . 46
3.2.4 Spectral variability . . . . . . . . 48
3.3 Discussion . . . . . . . . 51
3.4 Conclusion . . . . . . . . 53

**4 Relativistic Reflection in a Sample of Seyfert 1 galaxies 55**
4.1 Introduction . . . . . . . . 55
4.2 Sample Selection . . . . . . . . 56
4.3 Data Analysis . . . . . . . . 57
4.3.1 Baseline model . . . . . . . . 57
4.3.2 Narrow Line Model . . . . . . . . 59
4.3.3 Relativistic Fe K$\alpha$ analysis . . . . . . . . 65
4.4 A Self-Consistent Reflection Model . . . . . . . . 70
4.4.1 The case of MCG +8-11-11 and IC 4329A . . . . . . . . 72
4.5 Discussion . . . . . . . . 75
4.6 Conclusion . . . . . . . . 78

**5 Evidence for gravitational light-bending in two Seyfert galaxies 81**
5.1 Introduction . . . . . . . . 81
5.2 Sample Selection . . . . . . . . 81
5.3 Sample Data Analysis . . . . . . . . 82
5.4 MCG -6-30-15 and NGC 4051 . . . . . . . . 85
5.4.1 Introduction . . . . . . . . 85
5.4.2 Light Bending Model . . . . . . . . 87
5.4.3 Data Analysis . . . . . . . . 91
5.5 Discussion . . . . . . . . 104
5.6 Conclusion . . . . . . . . 106

**6 Conclusions 109**

**Acknowledgements 123**

# List of Figures

1.1 Spectrum of a steady, geometrically thin and optically thick accretion disk. 7
1.2 Scheme of the Unified Model for AGN. . . . . . . . . . . . . . . . . . . . . 9
1.3 Picture of the transitions occurring in the fluorescence process. . . . . . . . 12
1.4 X-ray reflection spectrum. . . . . . . . . . . . . . . . . . . . . . . . . . . 13
1.5 Fe K$\alpha$ energy lines and fluorescence yield as a function of the ionization. . 14
1.6 EW as a function of the inclination of the accretion disk. . . . . . . . . . . 16
1.7 Theoretical ionized reflection spectra for different ionisation parameter. . . 17
1.8 Individual effects contributing to the broadening of narrow emission lines. . 18
1.9 Relativistic Fe line profiles for a non-rotating black hole. . . . . . . . . . . 19
1.10 Relativistic line profile for the Schwarzschild and Kerr BH. . . . . . . . . . 20
1.11 Relativistic line profile dependance on the emissivity profile. . . . . . . . . 21

2.1 Graphic representations of *Suzaku* (left) and its left side (right). . . . . . . 26
2.2 Representation of the XRTs onboard *Suzaku* . . . . . . . . . . . . . . . . . 27
2.3 Scheme of the Wolter type I reflecting optics. . . . . . . . . . . . . . . . . . 27
2.4 Total effective area of the four XRT-I instruments . . . . . . . . . . . . . . 28
2.5 Scheme of the XIS CCD . . . . . . . . . . . . . . . . . . . . . . . . . . . . 29
2.6 Schematic view of the HXD detector . . . . . . . . . . . . . . . . . . . . . 31
2.7 Total effective area of the HXD detectors, PIN and GSO . . . . . . . . . . 31
2.8 Example image from the XIS instrument. . . . . . . . . . . . . . . . . . . . 33
2.9 Scheme of the *NuSTAR* principal components. . . . . . . . . . . . . . . . . 35
2.10 Point Spread Function of *NuSTAR* . . . . . . . . . . . . . . . . . . . . . . 36
2.11 *NuSTAR* effective collecting area. . . . . . . . . . . . . . . . . . . . . . . 37

3.1 *Suzaku* XIS image of IC 4329A . . . . . . . . . . . . . . . . . . . . . . . . 41
3.2 IC 4329A light curves for each observation. . . . . . . . . . . . . . . . . . . 42
3.3 Data to model ratio of each *Suzaku* observations of IC 4329A . . . . . . . . 44
3.4 Combined data to model ratio of all the 5 observations . . . . . . . . . . . 45
3.5 Power law slope and 2-10 keV flux as a function of time. . . . . . . . . . . 48
3.6 Compton reflection component and Fe line fluxes as a function of time. . . 49
3.7 Reflection fraction and Fe line equivalent width as a function of time. . . . 49
3.8 Correlation plots between the important parameters. . . . . . . . . . . . . 50

4.1 Data to model ratio of each source in the sample observed with *Suzaku* . . 61
4.2 Data to model Ratio of the XIS spectrum for NGC 7469 . . . . . . . . . . 68
4.3 EW of the relativistic Fe line as a function of the counts in the Fe band . . 69
4.4 Unfolded spectrum for MCG +8-11-11 . . . . . . . . . . . . . . . . . . . . 73
4.5 Unfolded spectrum for IC 4329A (Obs. ID 702113020 . . . . . . . . . . . . 74

5.1 EW, PLC and RDC components as a function of $h_s$ for 30°. . . . . . . . . 88
5.2 EW, PLC and RDC components as a function of $h_s$ for 60° . . . . . . . . . 88
5.3 Fe line flux as a function of the direct continuum for 30°. . . . . . . . . . . 90
5.4 Fe line flux as a function of the direct continuum for 60°. . . . . . . . . . . 90
5.5 Reflection fraction as a function of the primary source height. . . . . . . . 91
5.6 Data to model ratio of each *NuSTAR* observation of MCG -6-30-15 . . . . 92
5.7 Data to model ratio of each *NuSTAR* observation of NGC 4051 . . . . . . 93
5.8 *NuSTAR* light curves for the observations of MCG -6-30-15 . . . . . . . . . 95
5.9 *NuSTAR* light curves for the observations of NGC 4051 . . . . . . . . . . . 96
5.10 Broad Fe line EW as a function of the 3-10 keV flux for MCG -6-30-15. . . 98
5.11 Broad Fe line as a function of the 3-10 keV flux for NGC 4051. . . . . . . . 99
5.12 Relativistic Fe line flux as a function of the 3-10 keV flux for MCG -6-30-15. 100
5.13 Relativistic Fe line flux as a function of the 3-10 keV flux for NGC 4051. . 101
5.14 Broad R as a function of the corona height for MCG -6-30-15. . . . . . . . 102
5.15 Broad R as a function of the corona height for NGC 4051. . . . . . . . . . 103
5.16 Relativistic R as a function of the 3-10 keV flux for MCG -6-30-15. . . . . 104
5.17 Relativistic R as a function of the 3-10 keV flux for NGC 4051. . . . . . . 105

# List of Tables

2.1 Design parameters and performances of the XRT instrument. . . . . . . . . 28
2.2 Design parameters and performance of the XIS instrument. . . . . . . . . . 30
2.3 Performance of the HXD instrument. . . . . . . . . . . . . . . . . . . . . . 30
2.4 XIS screening criteria . . . . . . . . . . . . . . . . . . . . . . . . . . . . 32
2.5 PIN screening criteria . . . . . . . . . . . . . . . . . . . . . . . . . . . . 34
2.6 Key parameters of *NuSTAR*. . . . . . . . . . . . . . . . . . . . . . . . . . 35
2.7 Encircled energy fraction for *NuSTAR* optics. . . . . . . . . . . . . . . . . 36

3.1 Best-fit parameters for the Gaussian model. . . . . . . . . . . . . . . . . 45
3.2 Best-fit parameters for Reflection model. . . . . . . . . . . . . . . . . . . 47
3.3 $\Delta\chi^2$ between the Gaussian and the Reflection model. . . . . . . . . . . . 47

4.1 Sources missing relativistic Fe K$\alpha$ line in the *XMM-Newton* observations . 57
4.2 PIN energy ranges used in the analysis. . . . . . . . . . . . . . . . . . . . 58
4.3 Observations where the Fe XXV and the Fe XXVI lines were detected. . . . 60
4.4 Best-fit parameters for the Narrow Line Model. . . . . . . . . . . . . . . . 64
4.5 Results of the simulations for $\Delta\chi^2$ at the 95% confidence level. . . . . . . . 66
4.6 Best-fit parameters for the Relativistic Relline model. . . . . . . . . . . . . 67
4.7 $\Delta\chi^2$ between the Relativistic Relline and the Relativistic Pexmon model. . 71

5.1 Sample of Seyfert 1 with *NuSTAR* observations in archive . . . . . . . . . 82
5.2 Best fit parameters for the Gaussian Model . . . . . . . . . . . . . . . . . 84
5.3 Best Fit parameters of the Relativistic Relline model. . . . . . . . . . . . . 97
5.4 Best fit parameters of the Relativistic Pexmon Model . . . . . . . . . . . . 97
5.5 Ranges in corona height considered for each regime and source. . . . . . . 100

# Zusammenfassung

Aktive Galaktische Nuklei (AGN) sind die leistungsstärksten beständig strahlenden Quellen des Himmels. Die Strahlung dieser Objekte wird durch Akkretion von Materie auf ein supermassives Schwarzes Loch (SL) erzeugt, das sich im Zentrum einer Galaxie befindet. Das SL ist umgeben von Gas, welches aufgrund seines Drehimpulses in einer Akkretionsscheibe das SL umkreist. Diese Materie verliert durch viskose Wechselwirkungen an Drehimpuls und bewegt sich langsam in die inneren Regionen der Scheibe, wobei Strahlung freigesetzt wird (Shakura & Sunyaev 1973). Wie von der Standardtheorie der Akkretionsscheiben vorhergesagt, wird beobachtet, dass das AGN Spektrum von optischer/UV Strahlung dominiert wird. Das Röntgenspektrum hingegen hat die Form eines Potenzgesetzes und es wird davon ausgegangen, dass es durch inverse Compton Streuung der optischen/UV Photonen in einer heißen Corona oberhalb des SL entsteht. Nimmt man an, dass die Scheibe von der Corona umgeben ist und letztere Strahlung isotrop emittiert (und Effekte der gravitativen Lichtablenkung vernachlässigbar sind), so erreicht die eine Hälfte der Röntgen Photonen den Beobachter, während die andere Hälfte mit der Akkretionsscheibe wechselwirkt und eine Reflexionskomponente erzeugt. Dieses Spektrum ist charakterisiert durch die Präsenz einer starken Fe K$\alpha$ Linie bei 6.4 keV und einem breitbandigen Peak bei $\sim$20-30 keV, dem sogenannten "Compton Huckel", der durch Compton Rückstreuung der Röntgen Photonen verursacht wird. Das Profil der Fe K$\alpha$ Linie ist intrinsisch schmal. Wird die Linie jedoch von den inneren Regionen der Akkretionsscheibe emittiert, so verändern starke Gravitationseffekte ihre Form, wodurch ein schiefes, asymmetrisches und stark verbreitertes Profil entsteht. Dieses Profil hängt von der Geometrie der Akkretionsscheibe und den Eigenschaften des zentralen SL ab. Aus diesem Grund sind Röntgenbeobachtungen von Seyfert 1 Galaxien das geeignetste Mittel, um die Physik der innersten Regionen dieser Objekte zu untersuchen. Tatsächlich werden Objekte dieser Klasse (im Gegensatz zu Seyfert 2 Galaxien) unter einem derartigen Blickwinkel beobachtet, so dass der zentrale Motor nicht durch den staubigen Torus verdeckt wird. Zahlreiche Arbeiten haben mit Hilfe einer spektroskopischen Analyse der Röntgendaten die Physik der Akkretionsprozesse auf Schwarze Löcher untersucht. Um jedoch die Präsenz relativistischer Reflexion nachweisen zu können, werden tiefe Beobachtungen einer großen Stichprobe von AGN und hochentwickelte Datenanalyseverfahren benötigt. Aus diesen Gründen sind die statistische Häufigkeit der relativistischen Reflexion und die exakte Geometrie der Compton Region bisher unzureichend verstanden.

Das Ziel dieser Arbeit war es daher, dieses seit langem bestehende Problem zu lösen,

wobei verstanden werden sollte, ob die relativistische Fe K$\alpha$ Linie in einigen Quellen tatsächlich nicht existiert, oder ob das Fehlen der Linie auf die niedrige Zählstatistik der Einzelbeobachtungen zurückzuführen ist. Hierfür wählten wir eine Stichprobe von Seyfert 1 Galaxien, die in früheren *XMM-Newton* Beobachtungen keine breite Komponente der Fe Linie zeigten (Nandra et al. 2007). Für diese Analyse nutzten wir den erweiterten Energiebereich der *Suzaku* Spektren, der es uns erlaubte, die Fe Emissionslinien und gleichzeitig den zugehörigen Compton Huckel zu fitten und zu analysieren. Wir verwendeten öffentlich zugängliche *Suzaku* Spektren und fitteten alle Quellen mit einer Reihe von Modellen verschiedener Komplexität, um die Präsenz relativistischer Fe Linien zu prüfen. Selbst dann, wenn eines der hellsten Seyfert 1 Objekte, IC 4329A, analysiert wird, kann die breite Linie nicht mit hoher Signifikanz in einer kurzen einzelnen Beobachtung ($\sim$26 ks) detektiert werden. Werden jedoch die *Suzaku* Daten hinzugefügt, um ein höheres Signal-zu-Rausch Verhältnis zu erzielen, konnten wir die relativistische Fe Linie sicher nachweisen. Die Analyse der gesamten Stichprobe demonstriert, dass mindestens eine Beobachtung aller Quellen, und 12 von 22 Beobachtungen insgesamt, eine signifikante Verbesserung zeigt, wenn eine breite Linie zur Fitprozedur hinzugefügt wird, was nahe legt, dass dieses Merkmal möglicherweise in allen betrachteten Quellen existiert. Im Allgemeinen zeigt sich, dass die relativistische Fe K$\alpha$ Linie nur in Spektren mit großer Photonenzahl im Fe Energieband mit hoher Signifikanz ($> 95\%$) detektiert werden kann (Mantovani et al. 2016). Dieses Resultat steht im Einklang mit der Idee, dass diese breite Linie allgegenwärtig in Seyfert 1 Objekten ist, aber in einigen Fällen aufgrund der niedrigen Zählstatistik nicht detektierbar ist.

Des Weiteren versuchten wir in dieser Arbeit den Zusammenhang zwischen der Fe Linie und dem Compton Huckel bei hohen Energien besser zu verstehen. Da beide Komponenten Teil desselben Reflexionsspektrums sind, sollten sie gleichzeitig auf die Variationen des primären Kontinuums reagieren. Hierzu verwendeten wir für die Daten aller Quellen der Stichprobe ein selbstkonsistentes Modell (*pexmon*, Nandra et al. 2007), welches die wichtigsten Merkmale der Reflexionsspektren von entferntem Material und der inneren Akkretionsscheibe reproduziert. Das Resultat dieser Analyse zeigt Übereinstimmung zwischen der Stärke des Strahlungsflusses der Fe Linie und des Compton Huckels, was suggeriert, dass beide von demselben Material stammen.

Die Fokussierungskraft im harten Röntgenband des neuen *NuSTAR* Instruments erlaubt es uns, den instrumentellen Untergrund zu reduzieren und das Reflexionsspektrum mit noch größerer Präzision zu studieren. Wir wählten eine Stichprobe von Seyfert 1 Objekten, die mit *NuSTAR* beobachtet wurden, aber keine breite Fe Linie in vorherigen *XMM-Newton* Beobachtungen zeigten (Nandra et al. 2007). Für die Datenanalyse verwendeten wir dieselbe Methode wie für die *Suzaku* Daten, um das Reflexionsspektrum zu untersuchen. In dieser Studie stachen zwei Objekte, MCG-6-30-15 und NGC 4051, unmittelbar durch eine außergewöhnliche Besonderheit hervor. Insbesondere wird, verglichen mit dem Standardparadigma (George & Fabian 1991), ein besonders stark hervortretendes Reflexionsspektrum gemessen. Dieser Nachweis kann unter der Annahme von starken Effekten der gravitativen Lichtablenkung in diesen Quellen erklärt werden. Falls sich die primäre Lichtquelle nur wenige Gravitationsradien über dem Schwarzen Loch befindet, so werden die Röntgen Photonen auf die Akkretionsscheibe abgelenkt. Dies bewirkt eine Verstärkung des Strahlungsflusses der relativistischen Fe Linie und eine Verminderung des primären Röntgen Strahlungsflusses, der im Unendlichen detektiert wird. Nimmt man an, dass die Variabilität des Kontinuums nur mit den Variationen der Coronahöhe über einem Kerr Schwarzen Loch assoziiert ist, so ist es möglich, die Höhe der primären Strahlungsquelle über dem Schwarzen Loch selbst abzuschätzen. Daher verglichen wir die zeitlichen Variationen des primären Kontinuums und der Reflexionskomponenten in den *NuSTAR* Daten mit den erwarteten Vorhersagen des Lichtablenkungsmodells (Miniutti & Fabian 2004). Wir fanden heraus, dass die primäre Strahlungsquelle in MCG-6-30-15 im Bereich von 9-19 $r_g$ variiert, wohingegen sie in NGC 4051 zwischen 5-20 $r_g$ variiert.

Zusammenfassend bleibt festzuhalten, dass die in dieser Arbeit durchgeführte aufwendige Analyse der Röntgenspektren die Präsenz der relativistischen Fe Linie in allen Spektren mit ausreichendem Signal-zu-Rausch Verhältnis im Fe Band aufgedeckt hat. Darüber hinaus war es, dank der unübertroffenen Empfindlichkeit von *NuSTAR*, zum ersten Mal möglich, robuste Aussagen über die Geometrie und Größe der Röntgenstrahlungsregionen in einem Abstand weniger Gravitationsradien von den Schwarzen Löchern zu treffen.

# Abstract

Active Galactic Nuclei (AGN) are the most powerful and persistent sources in the sky. The radiation of these objects is caused by accretion of matter onto the supermassive black hole (BH) located in the center of the host galaxy. The BH is surrounded by gas which orbits in an accretion disk because of its angular momentum. Due to the presence of viscosity, this material loses angular momentum and moves slowly toward the inner regions of the disk, releasing radiation (Shakura & Sunyaev 1973). As predicted by the standard accretion disk theory, it is observed that the AGN spectrum is dominated by optical/UV radiation. The X-ray spectrum instead is thought to be produced by inverse Compton scattering of the optical/UV photons in a 'hot' corona placed above the BH and it has a power law shape. Assuming a slab geometry of the disk, if the corona emits isotropically (and gravitational light bending effects are negligible), half of the X-ray photons reach the observer, while the other half interact with the accretion disk, producing a reflection component. This spectrum is characterized by the presence of a strong Fe K$\alpha$ line at 6.4 keV and a broad feature peaking at $\sim$20-30 keV, the so-called Compton hump, produced by Compton backscattering of the X-ray photons. The profile of the Fe K$\alpha$ line is intrinsically narrow. However, when the line is emitted from the inner parts of the accretion disk, strong gravity effects will modify its shape, producing a skewed, asymmetric and highly broadened profile. This profile depends on the geometry of the accretion disk and the properties of the central BH. Therefore, X-ray observations of Seyfert 1 galaxies are the most suitable tool to probe the physics of the innermost regions of these objects. Indeed, this class of objects (as opposed to Seyfert 2) are observed at a viewing angle such that the central engine is not obscured by the dusty torus. Several works have used a spectroscopic analysis of the X-ray data to investigate the physics of accretion processes onto black holes. However, investigating the presence of relativistic reflection requires deep observations of large samples of AGN and sophisticated data analysis techniques. For these reasons the statistical occurrence of the relativistic reflection and the exact geometry of the comptonizing region remained elusive.

In this thesis, we aimed at solving this long standing issue by understanding whether the relativistic Fe K$\alpha$ line is truly absent in some sources or the lack of detection is due to the low statistics of the single observations. To do so, we selected a sample of Seyfert 1 galaxies among those that did not show a broad Fe line component in previous *XMM-Newton* observations (Nandra et al. 2007). For this analysis, we took advantage of the extended energy band of the *Suzaku* spectra, which allowed us to simultaneously fit and analyze the Fe emission lines and the associated Compton hump. We used publicly available

spectra from *Suzaku* and fitted all the sources with a series of models of varying complexity, testing the presence of relativistic Fe lines. Even when one of the brightest Seyfert 1 objects, IC 4329A is analysed, the broad line is not detected with high significance in short single epoch observations ($\sim$ 26 ks). However, when the *Suzaku* data are combined to achieve higher signal-to-noise ratio, we robustly detected a relativistic Fe line. The analysis of the entire sample shows that at least one observation of all the sources, and 12 out of 22 observations in total, shows a significant improvement when a broad line is added in the fitting procedure, suggesting that this feature might be present in all the objects considered. The overall picture shows that the relativistic Fe K$\alpha$ line is detected with high significance ($> 95\%$) only in spectra with high counts in the Fe energy band (Mantovani et al. 2016). This result is consistent with the idea that this broad line is ubiquitous in Seyfert 1 objects, but is, in some cases, not detected because of the low statistics of the data.

With this work we also aimed at investigate the relationship between the emission of the Fe line and the Compton hump at high energies. Being both parts of the same reflection spectrum, they should respond at the same time to the variations of the primary continuum. To do so, we applied to the data of all the sources in the sample a self-consistent model (*pexmon*, Nandra et al. 2007), which reproduces the main features of the reflection spectra produced from distant material and from the inner accretion disk. The result of this analysis shows consistency between the strength of the Fe line and the Compton hump flux, suggesting that they both arise from the same material.

The focusing capability in the hard X-ray band of the new *NuSTAR* instrument allows us to reduce the instrument background and to study the reflection spectrum with even more precision. We selected a sample of Seyfert 1 objects observed with *NuSTAR* lacking a broad Fe line in previous *XMM-Newton* observations (Nandra et al. 2007). We applied to these data the same analysis we did for the *Suzaku* observations to investigate the relativistic reflection. From this study, the striking peculiarity of two objects, MCG -6-30-15 and NGC 4051, immediately arose. In particular, a prominent reflection spectrum is measured, compared to the standard picture (George & Fabian 1991). This evidence can be explained by assuming the presence of gravitational light bending effects in those sources. If the primary source is placed above the black hole at a few gravitational radii, the X-ray photons will be bent onto the disk. This produces an enhancement of the relativistic Fe line flux and a decrease of the primary X-ray flux detected at infinity. Assuming that the variability of the continuum is associated only with the variations of the corona height above a Kerr black hole, it is possible to estimate the height of the primary source above the black hole itself. Therefore, we compared the time variations of the primary continuum and the reflection components in the *NuSTAR* data to the trends expected from the light bending model (Miniutti & Fabian 2004). We found that for MCG -6-30-15 the primary source varies in the 9-19 $r_g$ range, while for NGC 4051 it varies in the 5-20 $r_g$ range.

In conclusion, the sophisticated analysis of X-ray spectra presented in this work unveiled the presence of relativistic Fe K$\alpha$ line in all the spectra with sufficient signal-to-noise in the Fe band. Moreover, thanks to the superior sensitivity of *NuSTAR*, it has been possible for the first time to derive robust constraints on the geometry and size of the X-ray emitting regions located at a few gravitational radii from the black holes.

# Chapter 1

# Introduction

## 1.1 Active Galactic Nuclei

The term 'Active Galactic Nuclei' (AGN) refers to a few percent of galaxies whose nuclear/central emission can not be due to stellar thermonuclear emission (Schmidt 1963). AGN are the most powerful, persistent sources in the sky (see Risaliti & Elvis 2004 for a review). This definition includes a wide variety of phenomenologies. The resulting classification is rather complex and mainly based on luminosity and spectral features (Krolik 1999). The most important feature characterising the class of AGN is their enormous luminosity which spans a wide range, $10^{42}$ - $10^{48}$ erg s$^{-1}$ (Risaliti & Elvis 2004). The maximum luminosity these objects can achieve is based on the balance between the radiation force acting outward and the gravitational force acting inward and it is called Eddington Luminosity:

$$L_{Edd} = \frac{4\pi G M m_p c}{\sigma_T} \cong 1.3 \times 10^{38} \left(\frac{M}{M_\odot}\right) \frac{erg}{s} \tag{1.1}$$

where $M$ is the mass of the central object, $m_p$ the proton mass, $c$ the speed of light, $G$ is the universal gravitational constant, $M_\odot$ the solar mass and $\sigma_T$ the Thomson scattering cross-section for the electron. Assuming that AGN accrete at the maximum luminosity (i.e. the Eddington Luminosity presented in Eq. 1.1) and given the observed values of luminosities, the corresponding black hole mass is large, of the order of $M \approx 10^{4-10}$ M$_\odot$.

The so called "Supermassive black hole (SMBH) paradigm" is nearly unanimously accepted by the scientific community and represents the starting point to understand AGN physics (Rees 1984). It asserts that the SMBH is situated in the dynamical center of the host galaxy. It is surrounded by gas with angular momentum which is orbiting around the BH itself in a form of a disk (Shakura & Sunyaev 1973, see also section 1.2.1). Because of the presence of viscosity in the accretion disk, this material loses angular momentum and moves to the inner regions of the disk, releasing radiation. The conversion of mass into energy is done with some efficiency $\mu$, as in stars, so the energy available for a mass m is $E = \mu m c^2$. The luminosity can then be expressed as:

$$L = \mu \dot{m} c^2 \tag{1.2}$$

where $\dot{m} = \mathrm{d}m/\mathrm{d}t$ is the accretion rate and $\mu$ the efficiency of the disk. The efficiency of the stellar nuclear processes is too low in order to justify the high luminosity observed in AGN in such compact regions, without invoking high rate at which the mass is processed in the source. In fact, in this case, the rate would exceed 250 $M_{\odot} yr^{-1}$. This consideration confirms the idea of the accretion onto a compact object, such as a SMBH, in the active galactic nuclei. In this case, the efficiency depends on the spin of the black hole (see section 1.2 for more details). Moreover, it has been revealed that an extreme variability in flux is observed in the X-ray band. Variability on time scales of the order of days is observed when the luminosity is varying by a factor of $\gtrsim 2$ (Mushotzky et al. 1993). This allows us to put an appropriate limit on the compactness of the emitting source in order to justify the observed variation time-scales:

$$R_{source} \approx c \times t_{days} < 1pc \ll R_{Galaxy} \approx 10^4 pc. \tag{1.3}$$

In this way, the emitting region of the source is constrained to be of the order of few gravitational radii, $r_g$, where $r_g = GM/c^2$. Thus, only a very efficient process (such as accretion onto a BH) can explain such large luminosities produced within such small regions.

### 1.1.1 Black hole mass estimation

Different techniques have been developed to estimate and/or directly measure the mass of the central object in AGN (see Peterson 2014 for a review). These measurements lead to a range of masses of $10^5$ - $10^{9.5}$ $M_{\odot}$ (e.g. Peterson et al. 2004, Gültekin et al. 2009, Woo et al. 2010, McConnell & Ma 2013 among many others).

The most accurate and reliable technique for measuring the black hole masses is based on the study of the motions of individual objects, such as stars, orbiting in the gravitational potential of the black hole itself. The most well-determined mass is that of Sgr A$^*$ placed in the Galactic center (Eckart & Genzel 1996). Several observations of proper motions and radial velocities of individual stars around Sgr A$^*$ have been analysed (e.g. Genzel et al. 2010, Meyer et al. 2012). Advanced infrared detectors and adaptive optics on large telescopes allowed a precise estimation of the Galactic black hole mass of $4.1 \pm 0.4 \times 10^6$ $M_{\odot}$.

Black hole masses can also be derived from the effects of their gravitational potential on systems of stars or gas (see Ferrarese & Ford 2005 for a review on these methods). The use of stellar mass dynamics has the advantage that stars respond only to the gravitational force. In this case, it is easier to determine the radius of influence of a BH, defined as $R_{BH} = GM_{BH}/\sigma_*^2$, where $M_{BH}$ is the BH mass and $\sigma_*$ the velocity dispersion of the stars in the hosting galaxy bulge. However, high angular resolution is required for this type of analysis. On the other hand, methods based on gas dynamics have the advantage of being simpler. This is mainly because the gas is viscous and arranges into a rotating structure of a disk-like form quickly compared to the relaxation time of the stars in a galactic nucleus. These methods allowed the measurements of over 70 supermassive black hole masses (McConnell & Ma 2013). However, this number is not likely to increase in the near future because it is difficult to resolve the black hole radius of influence in objects further than the Virgo Cluster at 17 Mpc from us (Peterson 2014).

Reverberation mapping represents a viable alternative to these methods. It allows measurements of BH masses at larger cosmological distance using time variability. This technique is used to determine the size of the broad emission line region and the central black hole mass, connecting the variations of the direct continuum with the variations of the line intensity-shape (see Zu et al. 2011 for the most up-to-date methodology). Emission line lags have been measured for about 50 AGN in the last decades, mainly using the H$\beta$ emission line (Peterson et al. 2004). Once the line width ($\Delta V$) is measured from the optical spectra, it is possible to estimate the black hole mass with the following relation:

$$M_{BH} = f\left(\frac{\Delta V^2 R}{G}\right) \tag{1.4}$$

where $R$ is the reverberation radius and $f$ a dimensionless factor, different for each AGN, which is expected to be of the order of unity. Reverberation mapping has the disadvantage of being time-consuming. In fact, a reliable reverberation measurement requires a large number of observations for each source, typically of the order of 30-50 at minimum.

Simpler techniques have also been developed to determine the BH mass. In particular, reverberation mapping studies revealed the presence of a relationship between the radius of the Broad Line Region (BLR) and the luminosity of the AGN (Koratkar & Gaskell 1991, Kaspi et al. 2000, 2005, Bentz et al. 2006a, 2009a). This can be expressed as:

$$R_{BLR} \propto L^{1/2} \tag{1.5}$$

Combining this relation with a simple virial mass equation, it is possible to estimate the black hole masses in AGN, where broad emission lines are present in their spectra, using a single-epoch spectrum. This relation is an important tool which has been used to estimate the BH mass of several AGN (Laor 1998, Wandel et al. 1999, McLure & Jarvis 2002, Vestergaard & Peterson 2006).

Additional ways to determine the black hole masses have been developed, but used less frequently, either because they need special circumstances or lead to imprecise estimations. First, the masses can be measured from the gravitational redshift of the broad emission lines (Kollatschny 2003) using the relation:

$$c\Delta z = \frac{GM_{BH}}{cR_{BLR}} \tag{1.6}$$

where $\Delta z$ is the redshift and $R_{BLR}$ the size of the broad line region. Another method employs the temperature of the accretion disk, which can be derived by fitting the observed continuum, to measure the black hole mass. In fact, this parameter depends on the BH mass and on the mass accretion rate (Gliozzi et al. 2011).

X-ray observations have also been used to estimate this important parameter in AGN. In particular, Iwasawa et al. (2004) measured the BH mass associating the variations of the Fe K$\alpha$ emission line flux with the orbital motion of the accretion disk. Fabian et al. (2009) used the reverberation lags between the direct X-ray continuum and the reflection on the accretion disk for measuring the mass of the central object. Finally, the power spectral density is also used for these measurements. It shows a characteristic 'break frequency', being steeper at higher frequencies (Markowitz et al. 2003b, Papadakis 2004, McHardy et al. 2006). The break frequency depends on both the BH mass and the mass accretion rate and can be used to estimate these quantities.

## 1.2 Accretion Physics

Accretion can take place in different ways and the final result depends on many factors such as the geometry of the system, the presence of magnetic field and many others (Treves et al. 1988). The simplest model of accretion was developed by Bondi in 1952. The hypothesis of this model is spherical accretion onto a BH, dictated by the assumption that the accreting matter has an angular momentum which is everywhere smaller than the Keplerian one, and thus negligible. However, in AGN the accreting matter has substantial angular momentum that breaks the spherical symmetry (Treves et al. 1988). The more realistic scenario is therefore the one that we briefly discussed in the previous section where the most important process, governing the accretion of rotating matter, is the action of viscous stresses (Shakura & Sunyaev 1973). With these assumptions, the gas in the accretion disk will lose angular momentum. This process allows the matter to slowly move towards the inner parts of the accretion disk and eventually accrete (Shakura & Sunyaev 1973). The result is the production of electromagnetic radiation at the expense of the gravitational potential.

The potential energy $U$ of a mass $m$ at distance $r$ from the central source of mass $M$ is:

$$U = \frac{GMm}{r} \tag{1.7}$$

The rate at which the potential energy of falling material can be converted to radiation is given by:

$$L \approx \frac{dU}{dt} = \frac{GM}{r}\frac{dm}{dt} = \frac{GM\dot{m}}{r} \tag{1.8}$$

Comparing this relation with Eq. 1.2, it is possible to deduce that:

$$\mu \propto \frac{M}{r} \tag{1.9}$$

which is a measure of the compactness of the system. In particular, this is maximized in the case of a black hole, whose size can be expressed through the Schwarzschild radius $R_S$. This is the event horizon of a non-rotating black hole and is defined as:

$$R_S = \frac{2GM}{c^2} \tag{1.10}$$

For a non-rotating black hole, described by the Schwarzschild metric, the efficiency is $\mu\ (a = 0) \simeq 0.057$ (Shakura & Sunyaev 1973), while for a maximally rotating BH (Kerr metric) the efficiency is higher, $\mu\ (a \approx 1) \simeq 0.42$ (Novikov & Thorne 1973, Page & Thorne 1974). The spin of the BH is expressed from the dimensionless parameter $a$. In the latter case, the surrounding portion of spacetime is forced to co-rotate with the BH itself because of the presence of the frame dragging effect (Lense & Thirring 1918). In this case, the accretion disk can reach an inner radius which is about five times smaller than in the case of a non-rotating BH and the efficiency can increase by almost an order of magnitude.

Although the broad picture appears clear, there are still several open problems. For example, it is a matter of debate how to describe the loss of angular momentum of the accreting gas and the conversion of gravitational potential into radiation. The nature of this mechanism is still unclear, but useful results can be obtained considering the 'standard accretion disk model' proposed by Shakura & Sunyaev (1973). This model assumes a dimensionless parameter $\alpha$, which is characterizing a turbulent viscosity of some kind. We briefly present this model in the next section.

### 1.2.1 Standard Model

In this section, we introduce the standard model for accretion physics in a disk surrounding a black hole. This was proposed for the first time by Shakura & Sunyaev (1973). We consider a mass rotating around a black hole with mass $M$. In this situation, we assume the loss of angular momentum caused by the presence of the viscosity $\nu$. We also assume that the time scale of redistribution of the angular momentum is longer than the orbital time scale. Under these assumptions, around the BH the gas forms a geometrically thin disk with vertical height $h$. In this disk, the gas elements are orbiting in an almost circular orbit with angular velocity $\Omega_k = (GM/r^3)^{1/2}$. The small radial velocity $v_r$(r,t) corresponds to the accretion flow. Introducing the surface mass density of the disk as $\Sigma$(r,t), we can express the conservation of mass and angular momentum as

$$r\frac{\partial \Sigma}{\partial t} + \frac{\partial}{\partial r}(r\Sigma v_r) = 0 \tag{1.11}$$

and

$$r\frac{\partial}{\partial t}(\Sigma r^2 \Omega) + \frac{\partial}{\partial r}(r^3 \Sigma v_r \Omega) = \frac{1}{2\pi}\frac{\partial \mathscr{G}}{\partial r} \tag{1.12}$$

where

$$\mathscr{G}(r,t) = 2\pi r^3 \nu \Sigma \frac{\partial \Omega}{\partial r} \tag{1.13}$$

is the torque applied on the disk at radius $r$ from the flow coming outside this radius. Combining these equations and considering the definition of the angular velocity presented above, it is possible to express the radial velocity as a function of the surface mass density

$$v_r = -\frac{3}{\Sigma r^{1/2}}\frac{\partial}{\partial r}(\nu \Sigma r^{1/2}) \tag{1.14}$$

The viscous dissipation per unity area of the disk is

$$D(r) = \frac{3GM\dot{M}}{8\pi r^3}\left[1 - \left(\frac{r_{in}}{r}\right)^{1/2}\right] \tag{1.15}$$

and integrating over the whole disk, the total luminosity produced by the disk is

$$L_{disk} = \frac{GM\dot{M}}{2r_{in}} \tag{1.16}$$

Assuming that the energy dissipated by viscosity is emitted as a black body spectrum, we can derive the temperature of the disk surface as a function of the radius. Considering the conservation of the energy, i.e. $\sigma_{SB}T(r)^4 = D(r)$, where $\sigma_{SB}$ is the Stephan-Boltzman constant, the temperature can be written as:

$$T(r) = \left(\frac{3GM\dot{M}}{8\pi\sigma_{SB}r^3}\left[1 - \left(\frac{r_{in}}{r}\right)^{1/2}\right]\right)^{1/4} \tag{1.17}$$

For a fixed accretion rate $\dot{M}$ which scales with mass and a scaled radius $r/M$, the temperature of the disk depends on the mass $M$ of the black hole as $T \propto M^{-1/4}$. For a supermassive black hole, the derived temperature of the disk is $T \sim 10^5$ - $10^6$ K, which means that the disk emits in the optical and ultraviolet wavelengths.

One of the assumptions of the standard model is that the disk is geometrically thin. In this situation, the motions or accelerations in the vertical direction are negligible. The vertical structure of the disk is then regulated by the hydrostatic equilibrium between the vertical component of the gravity and the internal pressure of the gas:

$$h \sim \frac{c_s r}{v_K} \tag{1.18}$$

where $c_s$ is the sound speed ($c_s^2 = p/\rho$, with $p$ being the pressure and $\rho$ the density) and $v_K$ the local Keplerian velocity ($v_K = (GM/r)^{1/2}$). Thus, an accretion disk is geometrically thin when the local Keplerian velocity is supersonic ($h/r \ll 1 \Rightarrow v_K \gg c_s$).

From Equation 1.17, it is possible to easily calculate the overall spectrum emitted from the disk. This is obtained considering the radiation emitted from each elemental area of the disk according to the temperature specific to its radius:

$$B_\nu\left[T(r)\right] \propto \frac{\nu^3}{e^{\frac{k\nu}{kT(r)}} - 1} \tag{1.19}$$

In order to calculate the spectrum produced by a geometrically thin, optically thick accretion disk, we need to integrate Eq. 1.19 over the entire disk surface, obtaining:

$$S_\nu \propto \int_{r_{in}}^{r_{out}} B_\nu\left[T(r)\right] 2\pi r dr \tag{1.20}$$

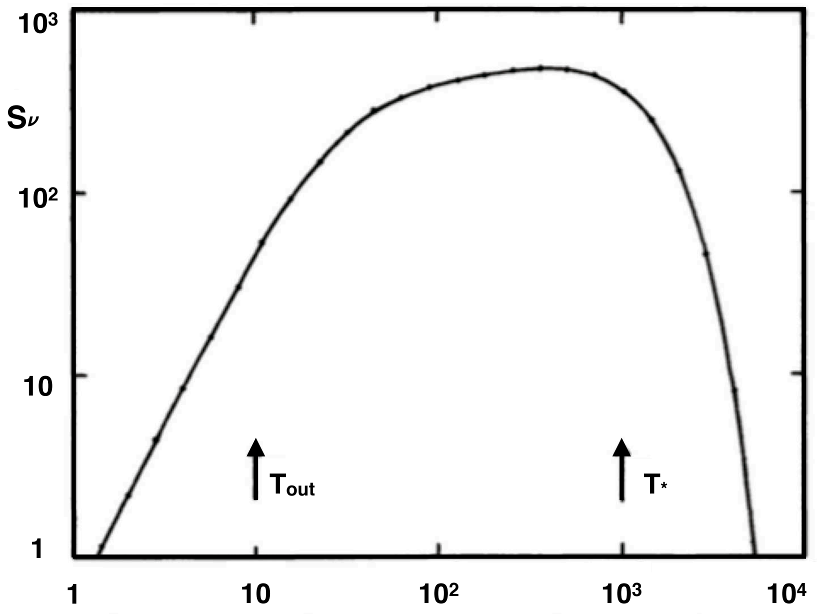

Figure 1.1: Integrated spectrum of a steady, geometrically thin and optically thick accretion disk. The units are arbitrary but the frequencies corresponding to $T_{out}$ and $T_*$ are labelled (we refer for detail to Pringle 1981).

where $r_{out}$ is the external radius of the disk and $B_\nu$ the Planckian photon distribution presented in Figure 1.1.

Simple considerations can easily explain the shape of the spectrum plotted in Figure 1.1. When $\nu \gg \mathrm{k}T_*/h$, the spectrum falls exponentially. This trend can be justified considering that the observed radiation is the high energy tail of the Planck distribution produced in the inner parts of the accretion disk. On the other hand, when $\nu \ll \mathrm{k}T_*/h$, the radiation comes from the outer region of the disk where the annuli have radii $r \gg r_{in}$. In this case the equation of the temperature for these regions (see Eq. 1.17) can be approximated as $T(r) = T_*\ (r/r_{in})^{-3/4}$. Defining $x = h\nu/\mathrm{k}T$ and $x_{out} = h\nu/\mathrm{k}T_{out}$, it is possible to rewrite Equation 1.20 as:

$$S_\nu \propto \nu^{\frac{1}{3}} \int_0^{x_{out}} \frac{x^{\frac{5}{3}} dx}{e^x - 1} \tag{1.21}$$

For frequencies in the range between $\mathrm{k}T_{out}/h$ and $\mathrm{k}T_*/h$, $x_{out} \gg 1$ and therefore $S_\nu \propto \nu^{\frac{1}{3}}$. This is the characteristic spectrum of an accretion disk, presented in Lynden-Bell (1969). For lower frequencies ($\nu \ll \mathrm{k}T_{out}/h$), the spectrum is dominated by the tail of the Rayleigh-Jeans distribution. This radiation is emitted from the outer regions of the accretion disk and leads to $S_\nu \propto \nu^2$.

## 1.3 Unified Model for Seyfert Galaxies

Among the large variety of AGN types, the study in this thesis is focussed on a sample of so-called Seyfert 1 galaxies. In the next sub-section, we briefly present the observational differences between the type 1 and 2 AGN, which is related to the unification model for AGN.

### 1.3.1 Observational Evidences of Seyfert Galaxies

Seyfert galaxies are one of the two largest groups of Active Galactic Nuclei, together with quasars (Greenstein & Schmidt 1964). The former class of AGN is defined by the seminal work of Seyfert (1943) who studied six sources that had peculiar properties. They showed strong and high-ionization emission lines superimposed over a stellar-like absorption spectrum. However, unlike quasars, the host galaxies are clearly detectable (Peterson 1997). Moreover, Seyfert (1943) found that these objects have broad emission lines with widths up to 8500 km/s and that this broadening correlates with the absolute magnitude of the central regions. Seyfert galaxies are then defined as low-luminosity AGN, compared to quasars, with magnitude of $M_B \geq$ -21.5 + 5 log $h_0$ and luminosity of the order of $L \sim 10^{39}$ - $10^{44}$ erg s$^{-1}$ (Schmidt & Green 1983, Meurs & Wilson 1984). This class of object represents about 16% of local galaxies (Maiolino & Rieke 1995). From a spectroscopic point of view, Seyfert galaxies show optical spectra with strong emission lines and weak absorption lines, the latter due to late-type giant stars. Khachikian & Weedman (1971) found that Seyfert galaxies can be separated into two different sub-classes, based on the emission lines observed in the optical/UV spectra. The so-called Seyfert 1 galaxies show both narrow lines and broad lines (Khachikian & Weedman 1971). The narrow emission lines are forbidden (e.g. $[OIII]$, $[NII]$) and permitted lines (e.g. H$\beta$, H$\alpha$) with widths of several hundreds of km/s and produced in the so-called Narrow Line Region (NLR), while the broad components are permitted lines only and the widths are observed to lay in the range between few thousands up to more than 10 000 km/s (Khachikian & Weedman 1974). The latter are emitted from the Broad Line Region (BLR) (see Peterson 2006 for a review). On the other hand, Seyfert 2 galaxies show only narrow emission lines in their spectra (Dahari & De Robertis 1988).

### 1.3.2 Unified Model

When Seyfert galaxies were first detected, it was initially believed that type 1 and 2 were objects of different nature. A turning point was the spectral analysis of the Seyfert 2 galaxy NGC 1068 (Antonucci & Miller 1985). The authors discovered that the broad lines, originally observed only in Seyfert 1 galaxies, were clearly visible in polarized light, but not in the total spectrum of NGC 1068. This result suggested that type 1 and 2 galaxies are essentially the same object, hosting identical nuclei. The difference is due to the presence of intervening dust which is obscuring the central source in type 2. The nucleus may be indirectly observed in polarized light thanks to reflecting gas which scatters the primary emission towards the line of sight of the observer (Antonucci & Miller 1985). Thus, the basic idea of the 'Unified Model' is that Seyfert 1 and 2 are the same objects, the only difference lies on the viewing angle and thus on the presence or not of absorbing particles along the line of sight, which obscures the nuclear radiation (Osterbrock 1978). In this scenario, the absorbing medium assumes clearly a fundamental role. This is usually considered as an optically thick 'torus', surrounding the nucleus and the BLR (Mathews & Capriotti 1985). In Figure 1.2, we present a scheme of the Unified Model for AGN (Beckmann & Shrader 2012). The AGN are divided in two main classes, radio-loud and radio-quiet AGN, depending on their emission in the radio band, and Seyfert galaxies are a sub-class of the radio-quiet ones. The BLR is located inside the rim of the torus, while the NLR further away from the central engine. In this scenario, when the system is observed edge-on, the torus covers all the radiation coming from the nucleus, including lines from the BLR. In this case the source is classified as a type 2. The narrow emission lines instead are still detected because the NLR is located outside the torus (Osterbrock & Mathews 1986). On the other hand, if the object is observed face-on and the torus does not intercept the line of sight, the observer can still detect every component in the spectrum and the object is classified as a type 1 (Osterbrock 1978).

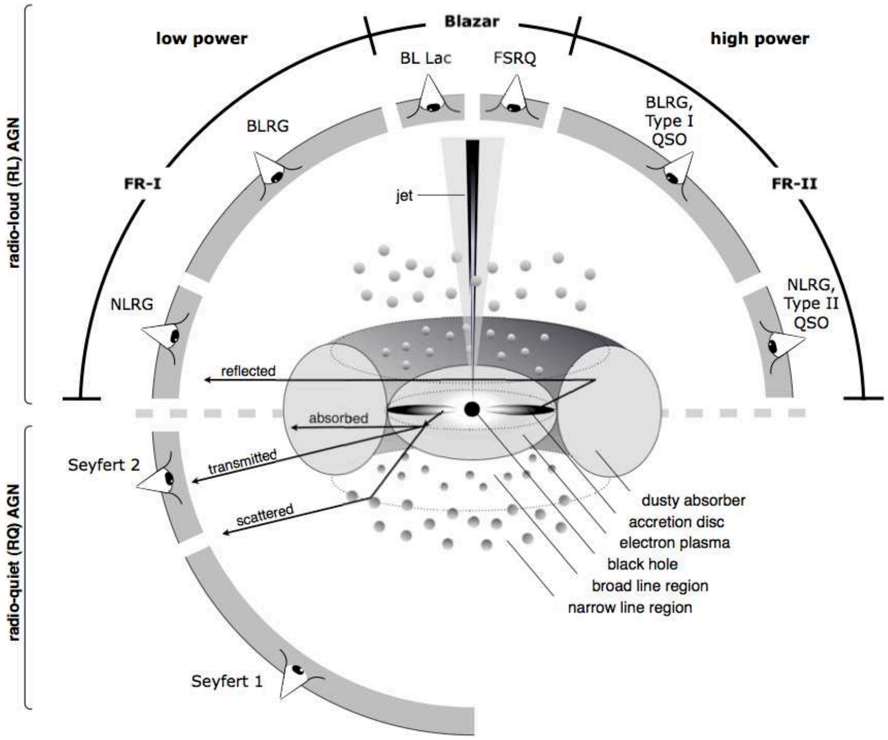

Figure 1.2: Scheme of the unified model for AGN (Beckmann & Shrader 2012, graphic courtesy of Marie-Luise Menzel (MPE)). The AGN are divided into two main classes depending on the radio emission, the so-called radio-loud and radio-quite AGN. The Seyfert galaxies are a sub-class of the radio-quite objects which are not emitting radio jet.

## 1.4 X-ray emission from AGN

If we consider the standard model for an accretion disk (Shakura & Sunyaev 1973), the AGN spectrum will be dominated by optical/UV radiation, because the emission from an optically thick, geometrically thin disk peaks in these energy bands. However, in accreting black hole systems, a power law component is observed in the X-ray spectra, extending to hard energies with exponential cut-off lying in the 80-300 keV energy range (Fabian et al. 1989, Perola et al. 2002, Fabian et al. 2015). This spectrum is not consistent with the black body emission predicted in the Shakura & Sunyaev (1973) standard accretion disk model. Instead, it is supposed to be emitted in the very inner parts of an AGN in a region called corona, by analogy with the sun (Ballantyne et al. 2001, Ballantyne & Fabian 2005). The analysis of X-ray observations is a powerful tool for investigating and understanding the black hole and AGN physics (Fabian et al. 2000). As we mentioned above, the typical X-ray spectrum of a Seyfert 1 galaxy has a power law shape. The typical values of the power law spectral index lie in the $\Gamma$ = 1.5 - 2.5 range (Nandra & Pounds 1994, Reeves & Turner 2000, Piconcelli et al. 2005, Page et al. 2005). The mechanism supposed to produce such a spectrum is the inverse Compton scattering (Fabian et al. 1989, Haardt & Maraschi 1991, Zdziarski et al. 1994, Fabian et al. 2000). In this process the optical/UV photons coming from the disk are scattered from the more energetic electrons in the 'hot' corona gaining energy, therefore being scattered to higher energies (Zdziarski et al. 1994). This process can occur as long as the photons have energies somewhat less than the electron thermal energy. As the photons approach the electron thermal energy, they no longer gain energy from the scattering and a sharp drop is expected in the spectrum, appearing as a high energy cut-off (Thorne & Price 1975, Sunyaev & Truemper 1979). This high energy cut-off are indeed observed in the spectra of AGN (see e.g. Fabian et al. 2015), indicating that thermal comptonization is at work. The observed cut-off gives information about the temperature of the electron in the corona (Rybicki & Lightman 1979, Pozdnyakov et al. 1983, Fabian et al. 2015).

Assuming the thermal comptonization process acting in the corona, a wide range of the power law spectral index is expected. However, the observations revealed values of $\Gamma$ which lie in a narrower range, between 1.5 and 2.5 as mentioned above, suggesting the presence of a mechanism which regulates the slope of the primary X-ray spectrum. In particular, a coupling between the emission from the corona and the accretion disk can explain the observed values of $\Gamma$. A simple model, based on these considerations, was proposed by Haardt & Maraschi (1991). This model is called the 'two phase model' and assumes the presence of thermal distribution of electrons in equilibrium with a certain temperature $T_e$. The geometry proposed is a sandwich system where the standard accretion disk (the 'cold phase') is completely surrounded by the corona (the 'hot' phase). The two phases are coupled, i.e. the optically thick emission of the cold disk provides the soft photon input for the Comptonization in the hot corona, and hard Comptonized photons contributes to the heating of the thick phase (the accretion disk). The effect that the Comptonization will have on the spectrum depends on the temperature of the corona $T_e$ and on the number of electrons encountered by each photon which is usually expressed by the optical depth to Thomson scattering $\tau_e$ (Lightman & Zdziarski 1987). The overall impact on the X-ray spectrum is conveniently described by the $y$ parameter, which for a non relativistic distribution of electrons is given by:

$$y = \frac{4kT_e}{m_e c^2} max\left(\tau_e, \tau_e^2\right) \tag{1.22}$$

An important tool to investigate the origin of the X-ray emission is the study of its variability, which can aid understanding the geometry of the systems. As we mentioned above, in the two phase model the spectral index $\Gamma$ is a function of the optical depth $\tau$ and the temperature of the corona $T_e$. In particular, Zdziarski et al. (1996) parametrized this dependence as:

$$\Gamma = \sqrt{\frac{9}{4} + \frac{3m_e c^2}{kT_e\left[\left(\tau_e + \frac{3}{2}\right)^2 - \frac{9}{4}\right]}} - \frac{1}{2} \tag{1.23}$$

The anti-correlation between the $\Gamma$ parameter and the corona temperature $T_e$ expressed in the previous equation (Eq. 1.23) has been also detected in several sources. In particular, observations of long time scale variability (i.e. $> 1$ day) show that the photon index increases as the 2-10 keV flux increases (see Perola et al. 1986, Petrucci et al. 2000, De Rosa et al. 2002b, Ponti et al. 2006). These results support the thermal Comptonization model, since this behaviour is expected if the variation of the UV flux is responsible for the X-ray variability. Moreover, correlations are sometimes observed between UV and X-ray variability (Clavel et al. 1992, Uttley et al. 2000, Shemmer et al. 2001) and UV flux and $\Gamma$ (Nandra et al. 2000), together with an anti-correlation between the corona temperature and the slope of the power law $\Gamma$ (Nandra et al. 2000, Petrucci et al. 2003). However, when shorter time scales are investigated, such as few hours or less, it appears that the X-ray variability is not correlated with the UV emission anymore (Nandra et al. 1998). This behaviour could be explained considering local processes in the corona. For example, a magnetically structured corona, generated by buoyancy instability in the disk, can account for the observations of X-ray flare-like events in AGN (Di Matteo 1998, Merloni & Fabian 2001).

One open question of this model is the origin of the hot corona, which is not established yet. However, numerical simulations demonstrated that magnetohydrodynamic turbulence in the accretion disk could lead to dissipation outside the disk's photosphere producing regions much less dense than the disk itself, such as the hot corona (Balbus & Hawley 1998, Schnittman et al. 2013).

## 1.5 Reflection Spectrum

In the previous section, we described how the power law of the primary X-ray emission is produced and which are the physical processes involved. In this section, we want to investigate which processes the photons of the X-ray continuum undergo after they are emitted from the corona.

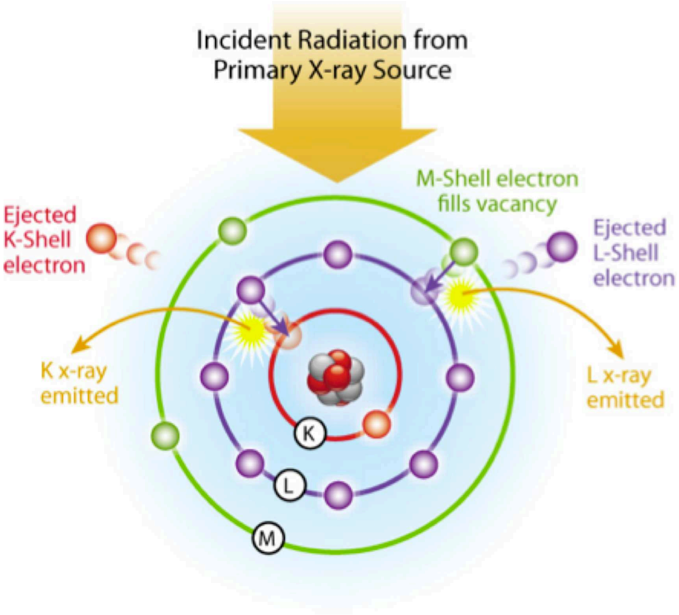

Figure 1.3: The picture shows the two types of transition which occur in the fluorescence process.

The important element of the two phase model presented above is the coupling between the accretion disk and the hot corona. We suppose that the surface of the accretion disk can be modelled as a semi-infinite slab of uniform gas. The disk is irradiated by the X-ray continuum spectrum produced in the corona (Haardt & Maraschi 1991, Haardt et al. 1994). If the corona emits isotropically, half of the photons fall on the accretion disk, while the other half reach the observer at infinity. We assume that the hydrogen and helium are fully ionized, but the other elements are neutral (Reynolds 1999). The X-ray photons can be Compton scattered by free-electrons or bound electrons of hydrogen and helium. Another possibility is that the photons are photoelectrically absorbed by the neutral material in the disk (Reynolds 1999, George & Fabian 1991). This process will take place only if the energies of the photons are above the threshold energy of the photoelectric transition invoked (Fermi 1950). In particular, the transition with the largest cross-section is the photo-ejection of a K-shell electron. Let's focus now on the emission of the Fe K$\alpha$ line. After the photo-ejection of the electron, the ion de-excites in one of two ways, both of which includes an electron from the L-shell dropping into the K-shell (Reynolds & Nowak 2003). In the first case, the extra energy is released trough the emission of a K$\alpha$ line photon, while in the second case the energy is carried away via the ejection of a second L-shell electron, i.e. autoionization or Auger effect (see Figure 1.3). The probability that one of the processes presented above will take place is given by the fluorescence yield Y.

This parameter is a function of the atomic number Z:

$$Y \approx \frac{Z^4}{Z^4 + 33^4} \tag{1.24}$$

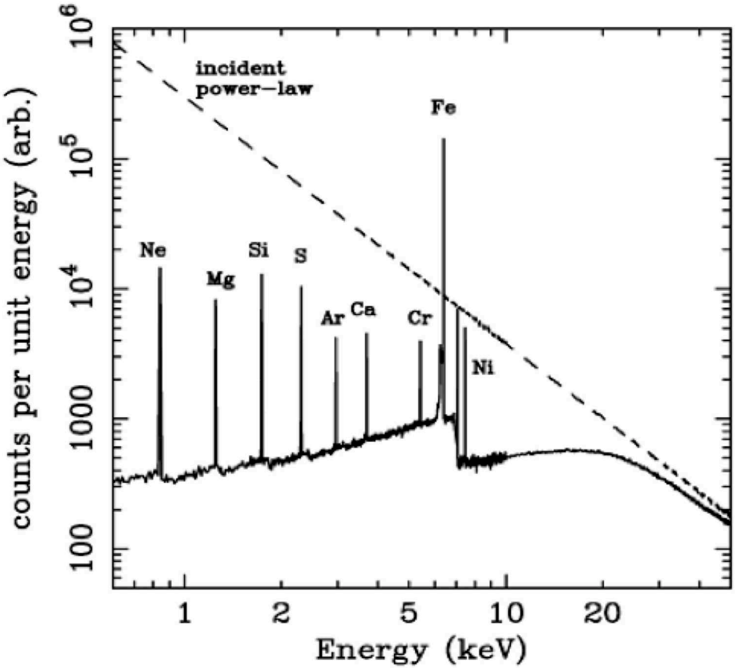

Figure 1.4: X-ray reflection spectrum produced by a power law from an optically thick material. The primary continuum is presented with the dashed line, while the continuos line shows the reprocessed spectrum, which includes the K$\alpha$ emission lines from the indicated elements (Reynolds 1999).

Figure 1.4 presents the results of Monte Carlo simulations of the reflection component produced when a disk with a slab geometry is illuminated by an incident power law with photon index of $\Gamma = 2$ (Reynolds 1999). At soft X-ray energies, the albedo of the slab is reduced by photoelectric absorption of the metals in the slab. On the other hand, at hard X-ray energies, this photo-absorption becomes less important and most of the incident photons are Compton back scattered out of the slab. This process produces a broad feature in the reflection spectrum peaking at $\sim$ 20-30 keV, the so-called 'Compton hump' (Lightman & White 1988, Nandra & Pounds 1994, Fabian & Ross 2010). The reflection spectrum includes the K$\alpha$ emission lines from the most abundant elements, as presented in Figure 1.4. Due to the combination of high fluorescent yield, large cosmic abundance and low photoelectric absorption, the strongest K$\alpha$ line is produced by the iron at 6.4 keV (Matt et al. 1997). The relevant energies for neutral iron are 6.391 keV and 6.404 keV for the K$\alpha_1$ and K$\alpha_2$ emission lines, respectively (Bearden 1967). Since the energy separation between these two lines is lower than the energy resolution available in present day X-ray detectors, it is usual to consider the value of 6.4 keV. This is the mean energy, weighted by the probability ratio 1:2 between the two transitions. Analogously, the mean value for the K$\beta$ doublet is 7.058 keV (Bearden 1967). In this case, the electron transition occurs between the M-shell and the K-shell. The flux of the Fe K$\beta$ line is expected to be 11.3 per cent of that of Fe K$\alpha$ one (Basko 1978, Palmeri et al. 2003a, Palmeri et al. 2003b, Molendi et al. 2003).

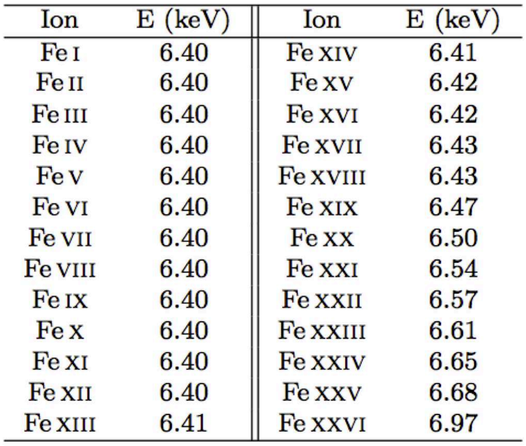

| Ion | E (keV) | Ion | E (keV) |
|---|---|---|---|
| Fe I | 6.40 | Fe XIV | 6.41 |
| Fe II | 6.40 | Fe XV | 6.42 |
| Fe III | 6.40 | Fe XVI | 6.42 |
| Fe IV | 6.40 | Fe XVII | 6.43 |
| Fe V | 6.40 | Fe XVIII | 6.43 |
| Fe VI | 6.40 | Fe XIX | 6.47 |
| Fe VII | 6.40 | Fe XX | 6.50 |
| Fe VIII | 6.40 | Fe XXI | 6.54 |
| Fe IX | 6.40 | Fe XXII | 6.57 |
| Fe X | 6.40 | Fe XXIII | 6.61 |
| Fe XI | 6.40 | Fe XXIV | 6.65 |
| Fe XII | 6.40 | Fe XXV | 6.68 |
| Fe XIII | 6.41 | Fe XXVI | 6.97 |

(a)

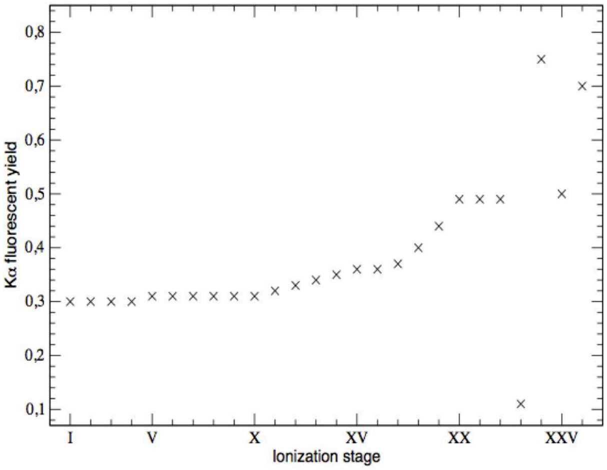

(b)

Figure 1.5: (a): Fe K$\alpha$ energy lines as a function of the ionization state of the iron (House 1969, Corliss & Sugar 1982). (b): Fe K$\alpha$ fluorescence yields as a function of the ionization state (Kaastra & Mewe 1993, Krolik & Kallman 1987).

The energy of the centroid of the Fe K$\alpha$ emission line depends on the ionisation state of the element. In particular, the energy is fairly stable up to Fe XVII - Fe XVIII, as presented in Figure 1.5a, when the M-shell is completely depleted. At this point the energy rises because of the lack of screening of the M-shell electrons, which leads to a higher binding energy of the inner shells. Finally, there is a sharp rise in energy when also the L-shell is void and this corresponds to the Fe XXV and Fe XXVI emission lines (House 1969, Corliss & Sugar 1982).

Not only the energy of the Fe K$\alpha$ transition, but also its fluorescence yield depends on the ionization state (Figure 1.5b). The yield becomes larger when the Fe XXIII emission lines are produced. In this case, due to the ionization state of the iron, the electrons configuration prevents the emission of the K$\alpha$ photon through a forbidden transition, requiring a more complex interaction which has low probability to occur (Chen et al. 1981). The fluorescence yields then rises sharply with Fe XXIV because no electrons are available for the Auger de-excitation. For Fe XXV and Fe XXVI no fluorescence is possible, because there are no electrons in the L-shell that can fall in the K-shell. Finally, it is interesting to note in Figure 1.4 a weak shoulder on the low-energy side of the Fe K$\alpha$ emission line. This feature is produced by line photons that have been Compton scattered and lost energy due to electron recoil, before escaping the disk. It is usually called 'Compton shoulder' (Matt 2002b).

Another important parameter that carries much information in the X-ray analysis of the AGN spectra is the Equivalent Width (EW) of an emission or absorption line. The EW depends on the underlying continuum and is defined as:

$$EW = \int \frac{F_\lambda - F_c(\lambda)}{F_c(\lambda)} d\lambda \tag{1.25}$$

where $F_\lambda$ is the observed flux of the line and $F_c$ ($\lambda$) is the corresponding continuum value at the same wavelength. Therefore, for a given primary X-ray continuum, the EW depends only on the physical properties of the gas which is emitting or absorbing the line. For example, if the line is produced in an accretion disk, the EW of the Fe emission line depends on the inclination of the disk. Ghisellini et al. (1994) have found that this dependence can be expressed as:

$$EW(\mu) = \frac{EW_{\mu=1}}{ln2} log \left(1 + \frac{1}{\mu}\right) \tag{1.26}$$

where $\mu = \cos(\mathrm{i})$ is the angle between the normal to the reflecting surface (i.e. the accretion disk) and the line of sight. Assuming the standard accretion disk model, where both the Fe line and the Compton reflection component are produced by the same material and they are parts of the same spectrum (see Fig. 1.4), the EW should correlate almost linearly with the amount of reflection. This is expressed in terms of the solid angle $R = \frac{\Omega}{2\pi}$ subtended by the reflector. Figure 1.6 shows that for a face-on disk with R =1, typical values for the EW of the Fe line are $\sim$ 150 eV, this value decreases for larger angles and smaller R.

The EW of the Fe line also depends on the iron abundance (Matt et al. 1997). This is because not only the different amount of iron ions must be taken into account, but also the L-shell and the M-shell iron self-absorption. Moreover, the iron K-edge rapidly saturates and few more photons are absorbed above a certain iron abundance. Matt et al. (1997) have parametrized all these effects in the formulae:

$$EW(A_{Fe}) = EW_{A_{Fe}=1}\ A_{Fe}^{\beta} \qquad\qquad 0.1 < A_{Fe} < 1 \tag{1.27}$$

$$EW(A_{Fe}) = EW_{A_{Fe}=1}\,(1 + b\ logA_{Fe}) \quad 1 < A_{Fe} < 20 \tag{1.28}$$

where $A_{Fe}$ is the iron abundance with respect to the solar values from Anders & Grevesse (1989) and $\beta$ and b are two parameters that increase with the inclination angle, being in the range 0.75 - 0.85 and 0.48 - 0.95, respectively.

For ionized disks, a useful parameter is the 'ionization parameter', which expresses the balance between the photoionazation and the recombination rate in the accretion disk (Ross & Fabian 1993). It can be defined as:

$$\xi = \frac{4\pi F_x(r)}{n(r)} \tag{1.29}$$

where $F_x$(r) is the X-ray flux incident on the disk per unit area at radius r and n(r) is the electron number density. As we already mentioned above, the centroid energy of the Fe

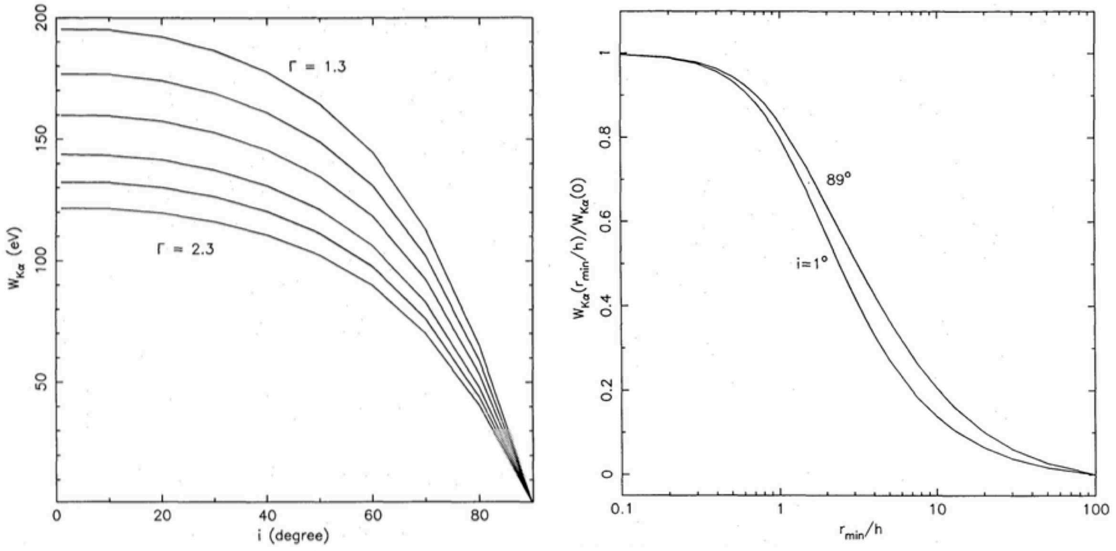

Figure 1.6: (a): the EW of the Fe line as a function of the inclination of the disk, for an incident power law photon index of (from the top) 1.3, 1.5, 1.7, 1.9, 2.1 and 2.3. The assumed geometry corresponds to R =1. (b): the EW as a function of the ratio between the inner radius of the accretion disk and the height of the illuminating source. The curves are normalized at $r_{min} = 0$ which corresponds to R =1 (see George & Fabian 1991 for more details).

K$\alpha$ emission line depends on the ionization state of this element. Matt et al. (1993, 1996) have performed detailed analysis on the reflection spectrum as a function of the ionization state of the reflecting material. The results suggest that, considering different ionization states (i.e. different values of the ionization parameter), four regimes can be delineated: the 'neutral reflection regime', 'intermediate ionization regime', ' high ionization regime' and 'fully ionized regime'. Figure 1.7 presents examples of reflection spectra models for different ionisation parameters (Ballantyne et al. 2001). From bottom to top, the reflection X-ray spectra for ionization parameters of log $\xi$ = 1.0, 1.5, 2.0, 2.5, 3.0, 3.5, 4.0, 4.5 and 5.0 are shown.

When $\xi < 100$ erg cm s$^{-1}$, the regime is called 'neutral reflection regime' and a 6.4 keV emission line from relatively cold material is present, together with the Compton hump emission at higher energies. At higher ionisation, when $100 < \xi < 500$ erg cm s$^{-1}$, the available iron ions are Fe xvii and Fe xxiii and the regime is called 'intermediate ionisation'. This range is crucial because the vacancy of the L-shell allows the resonant of the absorption of the K$\alpha$ photons and the following de-excitation follows the rule presented above for the fluorescence. The process of absorption and re-emission can eventually end in the loss of the photon through the Auger effect (Osterbrock 1989). Thus only few photons can escape resulting in a weaker Fe line flux and smaller EW compared to the previous regime (Ballantyne et al. 2001). In the 'high ionization regime', when $500 < \xi < 5000$ erg cm s$^{-1}$, the iron is mainly Fe xxv and Fe xxvi. The resonant scattering is still effective,

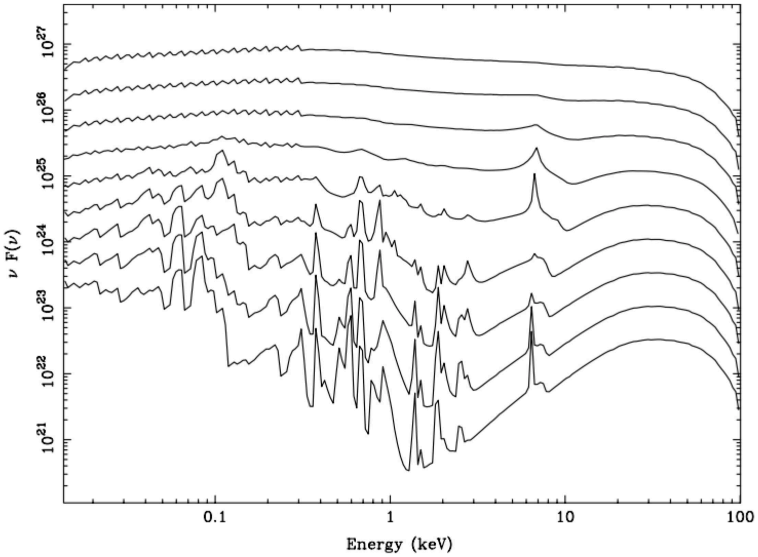

Figure 1.7: The plot shows the theoretical ionized reflection spectra for different ionisation parameter, as presented in Ballantyne et al. (2001). From bottom to top the curves show the spectra for ionisation parameters of log $\xi = 1.0$, 1.5, 2.0, 2.5, 3.0, 3.5, 4.0, 4.5 and 5.0.

but the photons of the Fe line are no longer lost, because the lack of L-shell electrons prevents the Auger effect to occur (Ballantyne et al. 2001). Strong Fe lines at 6.68 keV and 6.97 keV are present in the reflection spectrum. Finally, in the 'fully ionized regime', the disk is too ionized in order to produce any atomic features. Thus, there are no Fe emission lines or edges.

### Absorption in AGN

Once the X-ray photons are produced in the central region of the AGN, they can still be reprocessed by the various kind of circumnuclear matter lying around the central engine (Osterbrock & Mathews 1986). The most important effect is the possible absorption from material along the line of sight (Mathews & Capriotti 1985). For convenience AGN are typically divided in two sub-classes depending on the column density of the absorbing material. They are called 'Compton thick' if the column density of neutral (or weakly ionized) absorbing material along the line of sight exceeds the value of $\sigma_T^{-1} = 1.5 \times 10^{24}$ cm$^{-2}$ (Treister et al. 2009, Akylas et al. 2012). In this case the primary X-ray continuum is completely blocked up to 10 keV or more (Matt 2000). If the column density is lower, they are denominated as 'Compton thin' (Matt 2002a). In this case, only the photons having energies grater than a certain threshold proportional to the column density are allowed to pass through the material (Matt et al. 2003). On the other hand, if the source is completely unabsorbed, the spectrum detected by the observer is unaltered (Matt et al. 2003).

### 1.5.1 Relativistic Effects

The profile of the Fe K$\alpha$ line is intrinsically narrow, much lower than the resolution of the X-ray instruments, when the line is produced in regions far away from the central engine, such as the torus and/or the Narrow Line Region additional doppler broadening is indeed observed at a level of a few 100 $km\ s^{-1}$. However, when this feature is emitted from the inner accretion disk, its profile will be shaped by the high velocity movement of the material and by the presence of the black hole and be strongly broadened and skewed.

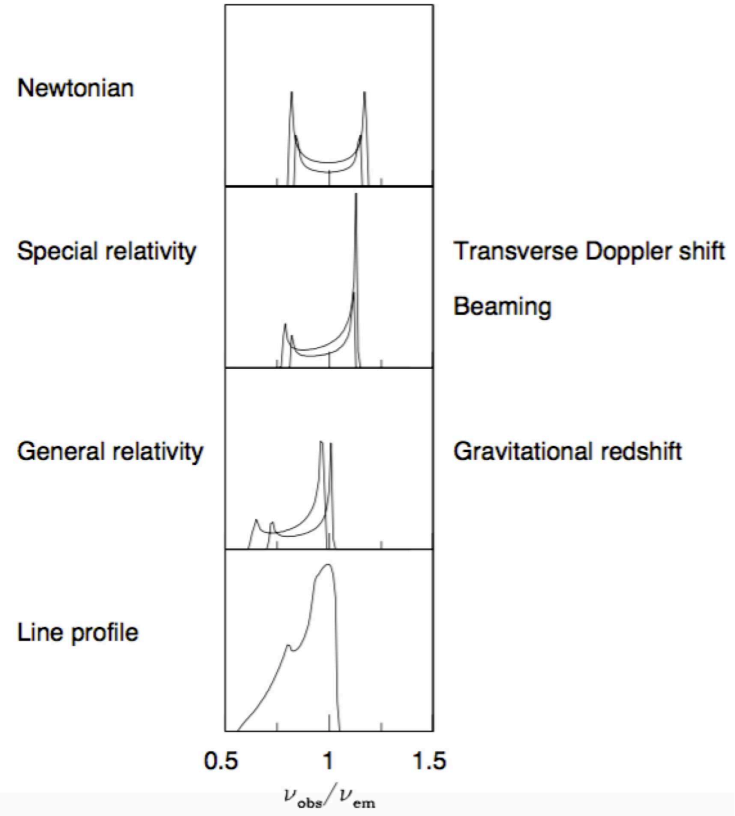

Figure 1.8: The plot presents all the individual effects contributing to the broadening of the narrow emission lines, resulting in the characteristic double-picked profile (Fabian et al. 2000).

A narrow line reflected by a Keplerian disk annulus will show a double peaked symmetric profile, as presented in the first panel of Figure 1.8 (Fabian et al. 2000). The blue peak is emitted from the regions of the accretion disk approaching the observer (blue shifted), while the red peak from the material receding (redshifted) in a keplerian disk. The inner regions of the accretion disk produce the broadest parts of the line because they move with higher velocities compared to the outer parts, eventually reaching relativistic speeds if the disk extends close to the innermost stable orbit. If so, because of relativistic beaming from the approaching regions, the blue peak will be enhanced with respect to the red one. Moreover, the transverse Doppler effect becomes important in the inner regions of the disk and the line profile is shifted to lower energies (second panel of Fig. 1.8). Finally, the presence of the black hole modifies the space time inducing a further shift and distortion of the line mostly due to gravitational redshift (third panel of Figure 1.8). Integrating the emission from all radii of the accretion disk, gives the characteristic skewed and highly broadened line profile presented in the last panel of Fig. 1.8.

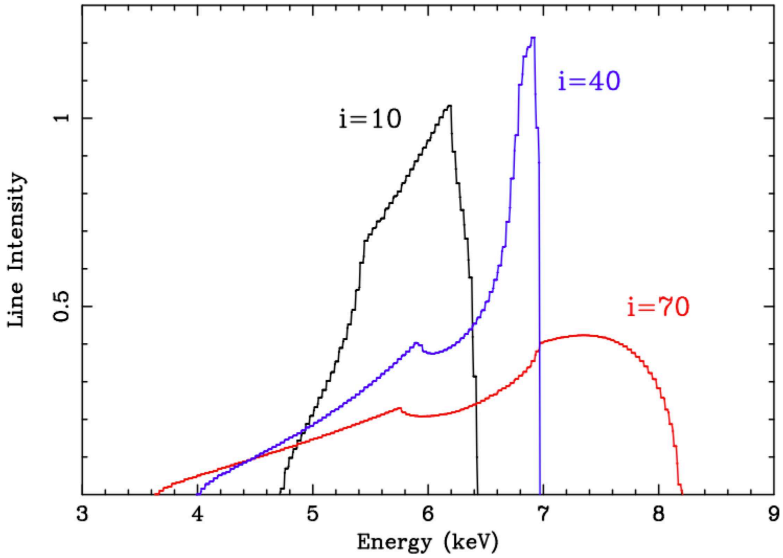

Figure 1.9: The plot show the relativistic Fe line profile in the case of a non-rotating BH (Schwarzschild metric). An emitting region extending from 6 $r_g$ to 30 $r_g$ was assumed. The model profiles are plotted for three different inclination angles: 10°, 40° and 70° (Fabian & Miniutti 2005).

The resulting profile of the relativistic Fe K$\alpha$ emission line is an important diagnostic of the properties of both the accretion disk and the central black hole (Fabian et al. 2000). Figure 1.9 and 1.10 show relativistic model line profile from the work of Fabian & Miniutti (2005). These plots summarize the results of fully relativistic computations of relativistic line model from Fabian et al. (1989), Laor (1991) and Dovčiak et al. (2004). In particular, Figure 1.9 shows the relativistic line profile emitted from an accretion disk around a non-rotating black hole, described by the Schwarzschild metric, assuming different inclination angles, 10°, 40° and 70° (Fabian & Miniutti 2005). The assumption is that the line is produced by an annulus of the disk extending between 6 $r_g$ and 30 $r_g$ from the black hole (where $r_g$ is the gravitational radius $r_g = GM/c^2$). The profile of the relativistic Fe line is highly sensitive to the inclination angle of the disk with respect to the line of sight. For example, the energy of the blue peak is a strong function of the inclination, providing an important tool to constrain this parameter. Moreover, the broadening of the profile increases with the inclination due to the fact that when the disk is face-on, only the transverse Doppler and gravitational redshift are affecting the line profile, i.e. there are no regions of the disk which are actually moving in the direction of the line of sight. As the inclination angle increases, the same happens to the velocity component along the line

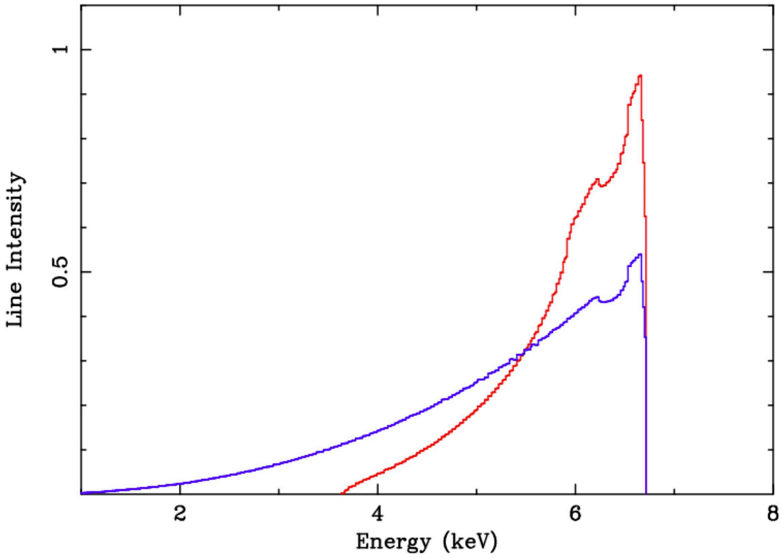

Figure 1.10: The plot shows the relativistic Fe line profile in the cases of a Schwarzschild black hole (red curve) and a Kerr black hole (blue curve). The emission regions is assumed to extend down to the radius of marginal stability: 6 $r_g$ and 1.24 $r_g$, respectively. The main difference in profile is due to the radius of marginal stability (Fabian & Miniutti 2005).

of sight of the approaching and receding regions of the disk. In this way the separation between the two peaks of the overall profile increases.

On the other hand, the red peak of the line profile is a sensitive function of the inner radius of the annulus where the line is emitted. Figure 1.10 presents the models of relativistic Fe line from a Schwarzschild back hole and a rapidly rotating one, which is described by the Kerr metric (Fabian et al. 2000). The assumption made for plotting these profiles is that the line emitting regions extend down to the last stable orbits for the two different metrics, i.e. 6 $r_g$ and 1.24 $r_g$. So the only difference between the two models is the inner disk radius. It is clear that the line profile is much broader in the Kerr metric case (blue line in the plot). This is due to the photons suffering stronger relativistic effects in the inner regions of the accretion disk compared to the ones emitted at larger radii (red line).

The relativistic Fe K$\alpha$ line depends also strongly on the spin of the black hole and the emissivity profile of the accretion disk. The first has important effects on the line profile because it is intrinsically correlated with the last stable orbit of the emitting disk. The radius of the last stable orbit ($r_{ms}$) is that radius where the orbits of the particles are no longer stable. The region $r < r_{ms}$ is called 'plunging region'. For a given black hole mass, this radius is a function of the angular momentum a = J/M and it can be expressed as:

$$r_{ms} = 3 + Z_2 - \left[(3 - Z_1)(3 + Z_1 + 2Z_2)\right]^{\frac{1}{2}} r_g \tag{1.30}$$

where

$$Z_1 = 1 + \left(1 - a^2\right)^{\frac{1}{3}} \left[(1+a)^{\frac{1}{3}} + (1-a)^{\frac{1}{3}}\right]; \quad Z_2 = \left(3a^2 + Z_1^2\right)^{\frac{1}{2}} \tag{1.31}$$

The values of the last stable orbit can vary from 1 $r_g$ for a = 1 to 6 $r_g$ when a = 0 (see Reynolds & Nowak 2003 for more details). However, it is believed that the maximal spin for a rotating black hole can not exceed 0.998 because of the capture of the disk photons by the black hole itself (Thorne 1974). This consideration implies that the smallest radius is $r_{ms} = 1.24$ $r_g$ (Thorne 1974). The results of the effect of the spin on the Fe line profile is a broader red wing compared to the Schwarzschild case, because the emission covers regions closer to the BH. Therefore, the gravitational redshift and the Doppler effect become important (Figure 1.10).

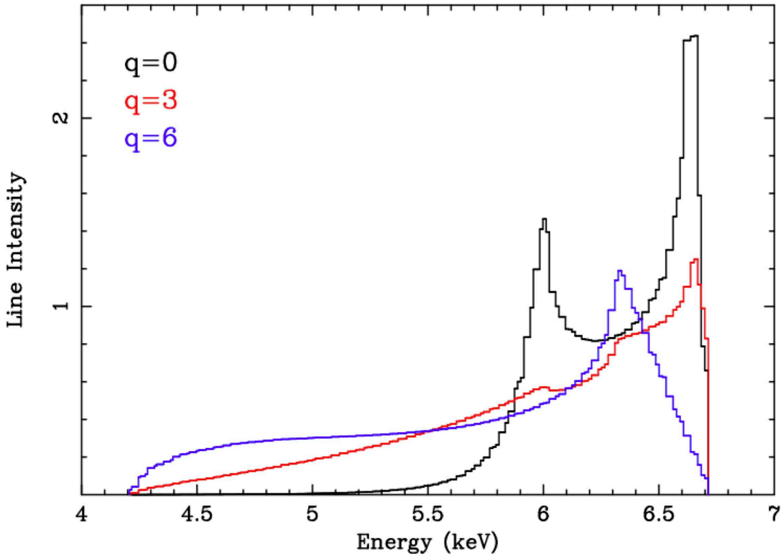

Figure 1.11: The plot shows the dependance of the relativistic line profile on the emissivity profile of the accretion disk. The emissivity is assumed to be a power law scaling with $r^{-q}$. When the profile is steeper, a broader and more redshifted line is produced, because the emission is concentrated in the inner regions where the gravity dominates (Fabian & Miniutti 2005).

As we mentioned above, the emissivity profile of the accretion disk plays a critical role in the emission of the relativistic Fe K$\alpha$ line. This function defines the reflected power per unit area as a function of the location on the disk and hence is related to the illumination pattern of the accretion disk. This is in term related to the energy dissipation in the disk and the heating of the corona. The emissivity profile is usually parametrized as a single or double power law $r^{-q}$. Assuming that the local intensity of X-ray reflection from the disk surface is proportional to the local dissipation in the underlying disk, the resulting emissivity index is q = 3 (e.g. Pringle 1981, Reynolds & Nowak 2003, Merloni & Fabian 2003). For high values of q, the emission is dominated by the inner regions of the accretion disk, resulting in a broader line (Fabian & Miniutti 2005). However, when this parameter is lower than 3, the emission from the outer parts becomes important and it is important to define the outer radius of the disk itself (Fabian & Miniutti 2005). The higher the outer radius, the smaller is the separation between the blue and red peaks of the emission line. This is due to the fact that a greater fraction of the line photons are produced in regions where the Doppler velocities are lower. We present the effects of different emissivity profiles in Figure 1.11 (Fabian & Miniutti 2005). The line intensities for a uniform (q = 0), standard (q = 3) and steep (q = 6) emissivity profiles are shown in the plot. The line profile varies as a function of the illumination pattern of the disk: the steeper the emissivity profile, the broader the emission line.

The relativistic Fe K$\alpha$ line profile, which depends on all the parameters presented above, is an important tool to measure these quantities in AGN. For this reasons, the analysis of the line profile can be used yo help understand the physics and inner geometry of this class of objects.

### 1.5.2 The Effects of Gravitational Light Bending

The X-ray temporal and spectral variability in AGN can be used to reveal the effects of gravitational light bending in black hole systems. If we assume that the primary source emitting the direct X-ray continuum is sufficiently far from the black hole so that the relativistic effects are negligible, we expect a direct correlation between the direct continuum and the reflection spectrum. The variability of the continuum is related to intrinsic luminosity variations of the corona. This results in a constant EW of the Fe K$\alpha$ line and a constant value for the reflection fraction. However, if the corona is close to the central object, the effects of gravitational light bending become important breaking the one-to-one correlation between the primary X-ray continuum and the reflection component. The strong gravitational potential produced by the black hole deviates the photons trajectory coming from the primary source. For example, the photons will be bent towards the BH itself (Miniutti et al. 2003). The result is a difference in flux between the primary continuum seen by the observer at infinity and the one reaching the accretion disk. The final result is that, if the primary source is located very close to the black hole, the correlation between the variation of the direct flux and the reflection spectrum will be modified.

Supporting the hypothesis of the presence of light bending effects close to the black hole, it has been observed that the variability of the reflection component, and in particular of the Fe line, is not correlated in a consistent way in all the studied objects (Lamer et al. 2000, Papadakis et al. 2002). In fact, the Fe K$\alpha$ emission line does not always responding to the variations of the primary continuum, as the simple reflection model predicts (Iwasawa et al. 1996, Miniutti & Fabian 2004). In some cases, an anti-correlation is present between the Fe line flux and the primary continuum, while in some sources the Fe line appears to be constant during large amplitude variations of the primary flux (see, for example, Markowitz et al. 2003a). Moreover, variations of the relativistic Fe line profile have been observed. In the case of MCG -6-30-15, the line tends to be very broad at low flux, while a strong narrow component appears at high flux (Iwasawa et al. 1996, Wilms et al. 2001, Fabian et al. 2002, Lee et al. 2002, Fabian & Vaughan 2003, Miniutti et al. 2003, Miniutti & Fabian 2004, Vaughan & Fabian 2004). In several sources it has been observed that the EW of the Fe line anti-correlates or remains constant with the variations of the primary X-ray continuum (Lamer et al. 2000, Papadakis et al. 2002). The lack of correlation could be attributed to reflection from distant material, such as the torus. However, the presence of a broad relativistic Fe line in the spectra conflicts with this hypothesis, suggesting the presence of an emission region close to the black hole. The light bending effects present in the vicinity of the central compact object might explain this scenario, as first investigated in Seyfert 1 galaxies by Miniutti et al. (2003).

## 1.6 This thesis

The main goal of this PhD project is the analysis of the relativistic Fe K$\alpha$ emission line in the X-ray spectra of Seyfert 1 galaxies. More specifically, we want to investigate the relationship between this emission line and the reflection component at higher energies. If the Fe line and the Compton hump are features of the same reflection spectrum and they are produced by the same material, they should respond at the same time to the variations of the illuminating X-ray primary continuum when the effects of gravitational light bending are negligible.

As we presented above in this chapter, the analysis of the relativistic Fe line is a powerful tool to investigate the inner regions of the accretion disk in AGN and the effects of strong gravity present in the central engine of these objects. The relativistic Fe K$\alpha$ line in AGN allows us to constrain the inner radius of the accretion disk, which is one of the critical parameters for characterizing the geometry of this class of objects, as well as the black hole spin. In fact, the innermost stable circular orbit depends on the spin of the black hole (see Eq. 1.30 in Section 1.5.1).

Assuming a standard accretion disk model, which is expected in the high efficiency systems such as bright Seyfert galaxies, relativistic Fe K$\alpha$ emission lines should always be detected in the X-ray spectra with sufficient signal-to-noise ratio. However, in samples of objects observed with *XMM-Newton* and *Suzaku* a significant fraction of sources and/or observations was missing this spectral feature. In particular, a relativistic Fe line component was not detected in the 65% of objects in Guainazzi et al. (2006), 30% of observations in Nandra et al. (2007), 60% of source in de La Calle Pérez et al. (2010) and 50% of observations in Patrick et al. (2012). The reason why this component is in some cases not detected is still unclear. Some hypothesis have been proposed in order to explain this puzzling picture. One possibility is that the signal-to-noise ratio plays an important role in the detectability of relativistic features. In fact, looking at samples compiled with *XMM-Newton* observations, it has been shown that this feature is preferentially observed in spectra with high statistics (e.g. Guainazzi et al. 2006, Nandra et al. 2007, de La Calle Pérez et al. 2010). Truncation of the inner accretion disk to large radii could also be responsible for the lack of clear relativistic line. Finally, if the relativistic effects are strong, such as in the case of a maximally spinning rotating black hole, the disk is ionized and/or the inclination is high, the profile of the Fe line would be sufficiently broadened and difficult to be disentangle from the underlying continuum (Bhayani & Nandra 2011).

The aim of this work is to investigate this phenomenon in more details, trying to understand if low statistical quality is the main reason preventing us to observe relativistic components. Moreover, we want to test for the presence of the Compton reflection in AGN using models which self-consistently reproduce the line and continuum, investigating the relationship between both the narrow and relativistic Fe line and the emission at higher energies, i.e. Compton hump. If they are features of the same reflection spectrum and they are produced by the same reflecting material, they should respond in the same way to the variations of the primary X-ray continuum. We will try to address these issues using *Suzaku* and *NuSTAR* data. With their extended energy ranges to higher energies compared to other missions, such as *XMM-Newton* and *Chandra*, these instruments allow us to better constrain the Compton hump emission and better model the primary continuum, which is critical to the analysis of relativistic emission lines.

In Chapter 2, we will give an overview of the *Suzaku* and *NuSTAR* missions, presenting also the data reduction for both instruments adopted in this work. In Chapter 3, the analysis of the bright Seyfert 1 galaxy IC 4329A is described. Chapter 4 presents a study of the relativistic Fe K$\alpha$ emission line in a sample of sources observed with *Suzaku.* Chapter (5) describes the data analysis on the objects we select with available *NuSTAR* archival observations.

# Chapter 2

# Data Reduction

## 2.1 Introduction

In this chapter, we present the two X-ray telescopes used in the following analysis: *Suzaku* and *NuSTAR*. The main goal of this thesis is to test the relativistic reflection in the Seyfert 1 galaxies. Compared to other satellites such as *Chandra* or *XMM-Newton*, these instruments allow us to directly study the high energy parts of the X-ray spectra. The energy ranges cover energies above 10 keV (i.e. the emission of the Compton hump), and it is also possible to better constrain the primary continuum.

In the first Section (2.2), we describe the instruments on board of *Suzaku* presenting the main characteristic of each detector. The data reduction of the spectra is presented in Section 2.3. Next, we present the *NuSTAR* telescope (Section 2.9) and the relative data reduction in Section 2.5.

## 2.2 Suzaku

### 2.2.1 Overview

The *Suzaku* telescope (formerly Astro-EII)[1] is the fifth Japanese x-ray astronomy satellite and it is a joint Japanese-US collaboration launched on 10 July 2005. *Suzaku* was designed with the aim of performing different kinds of observational studies of various X-ray sources. It is taking advantage of the high energy resolution and a higher sensitivity in the hard band than ever before, over the wide energy range of 0.4-600 keV. The satellite was launched into a nearly circular orbit with at 568 km altitude and an inclination of 31.9° to the equator and an orbital period of ∼96 minutes. Since it is close enough to the Earth, most of the sources are hidden by our planet for a determined fraction of the orbit period. The mean efficiency of the observations is $\sim 45\%$. This type of the orbit has the convenience of not crossing the Van Allen radiation belt, allowing faster and more efficient transmissions from

---

[1] The project was renamed *Suzaku* after the successful launch after the mythical Vermilion bird of the South, one of the four mythological guardian animals in the Chinese constellations.

and to earth and a lower particle background. This satellite weighs 1706 kg and is long 6.5 m on the telescope axis.

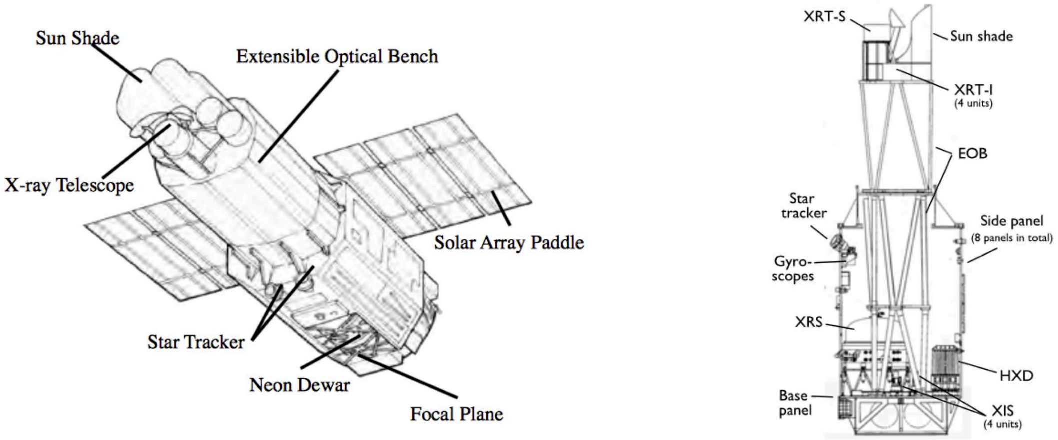

Figure 2.1: Graphic representations of *Suzaku* (left) and its left side (right).

Suzaku carries three different scientific detector systems: Hard X-ray Detector (HXD: Takahashi et al. 2007), X-ray Imaging Spectrometer (XIS: Koyama et al. 2007) and X-ray Spectrometer (XRS: Kelley et al. 2007). The spectrometers XIS and XRS are build in the focal plane of the X-ray Telescope (XRT: Serlemitsos et al. 2007). In Figure 2.1, a representation of the satellite configuration is presented. Just after a week from the launch, on 29 July 2005, a malfunction of the cooling system occurred, which caused on 8 August 2005 the entire reservoir of liquid helium to boil off into space. This determined the complete shut down of the XRS which was the primary instrument of the satellite. The other instruments, XIS and HXD, were unaffected by this malfunction and they were working properly delivering excellent science until 25 August 2015. JAXA announced that the communications with the satellite had been intermittent since 1 June. The recovery process of the scientific operations would be difficult to complete given the condition of the spacecraft. The operators of the mission decided to end the mission given also that *Suzaku* had exceeded the design lifespan by 8 years. The mission ended on 2 September 2015 when JAXA commanded the radio transmitters to witch themselves off.

We will present in the following sections the characteristic of each operating instrument.

### 2.2.2 X-ray Telescope (XRT)

The XRT is the mirror assembly on board of *Suzaku* (Serlemitsos et al. 2007). A representation of the XRT system is presented in Figure 2.2. It is composed of five thin-foil-nested Wolter-I type telescopes. The incident rays are reflected twice by a parabolic surface and then by a hyperbolic one. These surfaces focalise the rays on the focal plane (Figure 2.3). One of them is dedicated to the XRS and it is called XRS-S, while the other four are focused on the XIS. These are called XRT-I0, I1, I2 and I3 and they are co-aligned to image the same region of the sky. The XRTs are placed on the Extensible Optical Bench (EOB) on the spacecraft as shown in Figure 2.1.

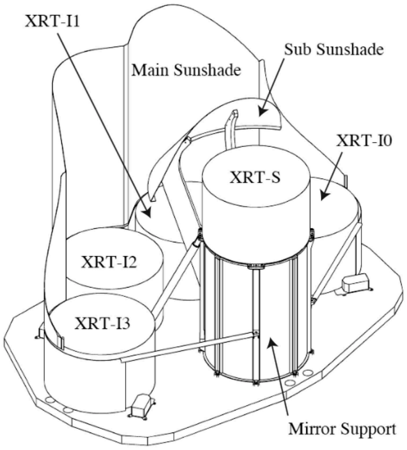

Figure 2.2: A representation of the XRTs onboard *Suzaku* is presented (Serlemitsos et al. 2007).

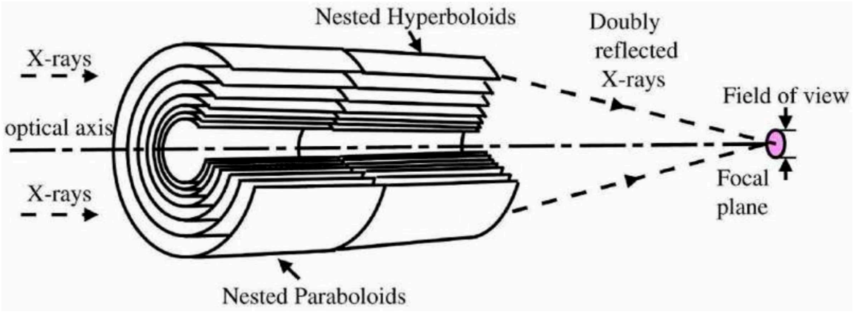

Figure 2.3: Scheme of the Wolter type I reflecting optics.

The focal length of the XRT-S is 4.50 m and that of the XRT-I is 4.75 m. The field of view for the XRT-Is is ∼20' at 1 keV and 14' at 7 keV. Figure 2.4 shows the total effective area of the XRT instrument. It is compared with that of *XMM-Newton* and *Chandra*. It is clear that the effective area is higher at the energies of the iron K$\alpha$ emission line and, in that range, it is comparable to that of *XMM-Newton*. However, at lower energies it appears to be lower than the other instruments. The XRT Point Spread Function (PSF) is approximately a Gaussian and is largely independent of the photon energy. The Half Power Diameters (HPD) are 1.8', 2.3' 2,.0' and 2.0' for the XRT 0, 1, 2 and 3, respectively. The design parameters and performance of the XRT instrument are presented in Table 2.1.

### 2.2.3 X-ray Imaging Spectrometer (XIS)

The four XIS instruments onboard *Suzaku* employ X-ray charge coupled devices (CCD). These are similar to those of the *ASCA* XIS, *Chandra* and *XMM-Newton* satellites. The

| | |
|---|---|
| Focal length | 4.75 m |
| Substrate | Aluminum (152 $\mu$m) |
| Reflector | Gold (> 0.1 $\mu$m) |
| Number of nesting | 175 |
| Inner / outer diameter | 118 mm / 399 mm |
| Incident angle | 0.18°-0.60° |
| Geometrical area | 873 cm$^2$ |
| Field of View | 20' at 1 keV / 14' at 7 keV |
| Effective Area | 450 cm$^2$ at 1.5 keV / 250 cm$^2$ at 7 keV |
| Half Power Diameter | 2.0' |

Table 2.1: Design parameters and performances of the XRT instrument (Serlemitsos et al. 2007).

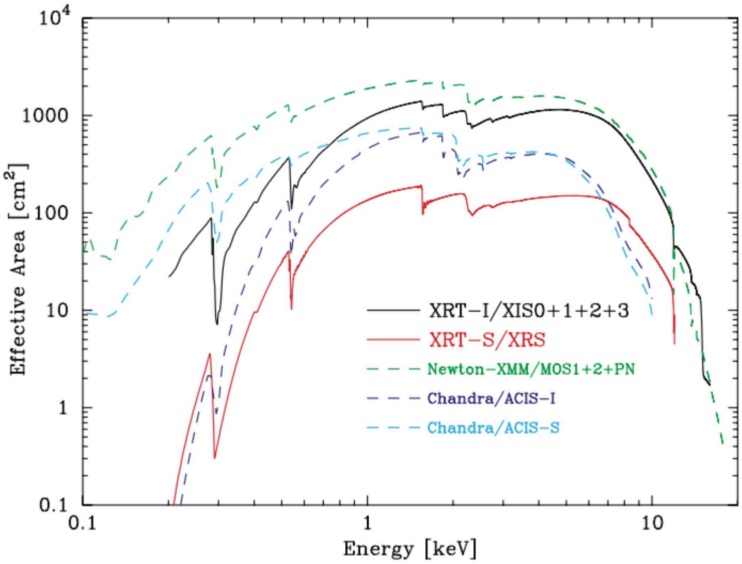

Figure 2.4: Total effective area of the four XRT-I instruments (Serlemitsos et al. 2007). They are compared with that of *XMM-Newton* and *Chandra*.

CCD are composed by integrated circuit engraved on a silicon surface. The photons incident on this surface produces free electrons through photoelectric absorption and the intensity of the electric cloud is proportional to the energy of the X-ray incident photon. The charge is then transferred onto the gate of an output transistor with a variation of the electrical potential. This process results in a voltage level (the so called "pulse height") which is proportional to the energy of the incident X-ray photon. The four instruments onboard *Suzaku* are called XIS0, 1, 2 and 3 and they are placed in the focal plane of an X-ray Telescope. After more than a year from the launch, in November 2006, a sudden increase of the "pixel number" occurred in the XIS2 sensor. The pixel number parameter shows the number of pixels in which the pixel level is larger than the event threshold (100

Analog to digital Unit, i.e. ADU). It was clear that a large amount of charge overflowed in the CCD, probably due to an impact of a micro-meteoroid on the CCD itself. Because it was difficult to recover the XIS2 sensor, the *Suzaku* team simply stopped operating the sensor. The same problem occurred for the XIS0 in June 2009. However, in this case the leak of charge was not serious, but a region of the XIS0 sensor, the A segment, cannot detect X-rays anymore.

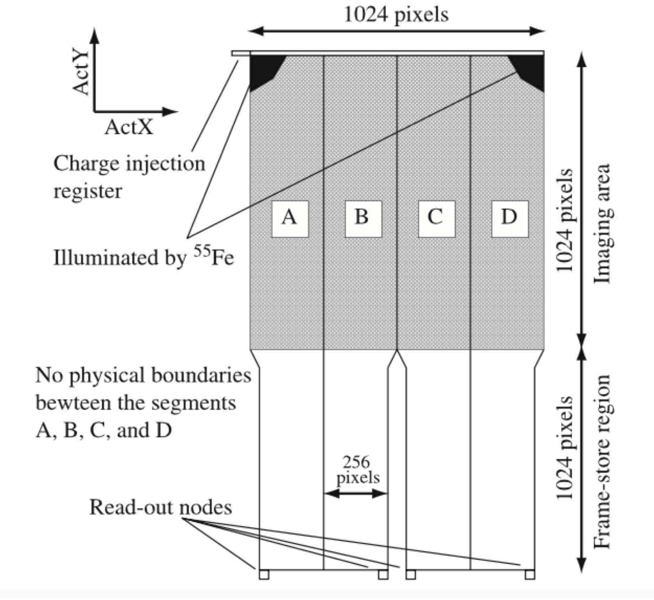

Figure 2.5: A scheme of the XIS CCD is presented (Koyama et al. 2007). It is composed by four segments and each one has is dedicated read-out node.

Figure 2.5 presents a schematic view of the structure of the XIS CCD. The CCD chip has an array of 1024×1024 pixels and it covers a field of view of 18’×18’. The pixel size of the imaging area is 24 $\mu$m × 24 $\mu$m and the size of the CCD is 25 mm × 25 mm. The CCD has four readout nodes (Node A-D) and each node reads the signals from 256 column of the chip. For calibration, each sensor has $^{55}$Fe calibration sources. Two sources are placed on the side wall of the housing and illuminate two corners of the imaging area (top of Segment A and D). Table 2.2 presents the design parameters and performance of the XIS. The XIS1 sensor uses a back-side illuminated CCD. This type of sensor receive the photons on the back side in order to increase the low-energy quantum detection efficiency (QDE). However, the QDE is slightly lower at high energies. On the other side, the XIS0, 2 and 3 use a front-side one. Note that the XIS has two CCD clocking modes: normal and parallel-sum (P-sum) modes. Normal mode has imaging capability with a resolution of 8 sec. On the other hand, the P-sum mode has good time resolution (7.8 msec), but it does not have imaging capability. In this work of this thesis the observations analyzed were taken in normal clocking mode and only the XIS0 and XIS3 spectra were considered in the spectral analysis, as the back-illuminated XIS1 has relatively high background.

The performance of the CCD usually degrades in space because of radiation damage

| | |
|---|---|
| Field of View | 18’ × 18’ |
| Energy range | 0.2-12 keV |
| Format | 1024 × 1024 pixels |
| Energy resolution | 130 eV (FWHM; at 5.9 keV) |
| Readout noise | ∼2.5 electrons |
| Time resolution | 8 s (normal) / 7.8 ms (p-sum) |

Table 2.2: Design parameters and performances of the XIS instrument (Serlemitsos et al. 2007).

produced by the cosmic rays. This happens due to charge traps produced by charged particles and they are accumulated in the CCD. The XIS has the capability to inject small amounts of charge into the pixels. The injection of charges is useful to fill the charge traps periodically and to make them almost innocuous. The spaced-row charge injection (SCI) method has been adopted as the standard method since Marc 2007 in order to reduce the radiation damage. The charge injection capability is also used to measure the charge transfer efficiency (CTE) of each CCD column for the no-SCI mode.

### 2.2.4 Hard X-ray Detector (HXD)

The Hard X-ray Detector (HXD) is a non imaging collimator instrument and a schematic view is presented in Figure 2.6. It is composed of silicon PIN diodes (PIN) and Gadolinium Silicate crystals scintillators (GSO) and it is covering an energy range of 10-600 keV. The main purpose of using this instrument is to extend the bandpass of *Suzaku* to high energies, allowing broad-band studies of astronomical objects. In our analysis we considered only the PIN data because the sources we considered were not bright enough in the GSO spectra in order to have enough statistics for the spectral analysis.

| | |
|---|---|
| Field of View | 34’ × 34’ ($\leq$ 100 keV) / 4.5° × 4.5° ($\geq$ 100 keV) |
| Bandpass | 10-70 keV (PIN) / 40-600 keV (GSO) |
| Energy resolution | ∼ 3.0 keV (PIN) / $7.6/\sqrt{E}\%$ (GSO) |
| Effective area | ∼160 cm$^2$ at 20 keV / ∼260 cm$^2$ at 100 keV |
| Time resolution | 61$\mu$s or 31 $\mu$s |

Table 2.3: Performances of the HXD instrument (Takahashi et al. 2007).

The HXD sensor is a compound-eye detector instrument. It is composed of 16 main detectors arranged as a 4 × 4 array and surrounding 20 crystal scintillators for active shielding. Each unit consists of two types of detectors: a Bismuth Germanate crystals phoswich counter (GSO/BGP) and a 2mm thick PIN silicon diodes placed inside the well, but in front of the GSO. The PIN diodes are sensitive below ∼60 keV, while the GSO counter above ∼40 keV. Figure 2.7 presents the total effective area of the PIN and GSO detectors, which are ∼160 cm$^2$ at 20 keV and ∼260 cm$^2$ at 100 keV, respectively. The energy resolution is ~4.0 keV (FWHM) for the PIN diodes and $7.6/\sqrt{E}\%$ (FWHM) for the scintillators, where E is the energy in MeV. The HXD time resolution is $61\mu$s. The HXD performance are presented in Table 2.3.

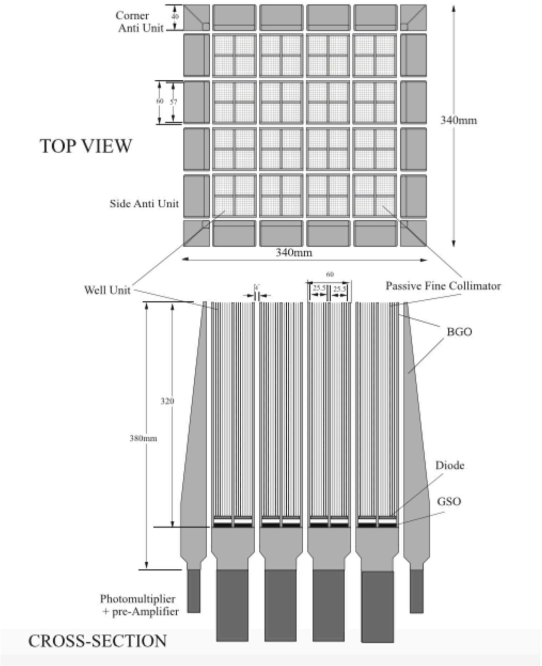

Figure 2.6: A scheme of the HXD detector is presented (Takahashi et al. 2007)

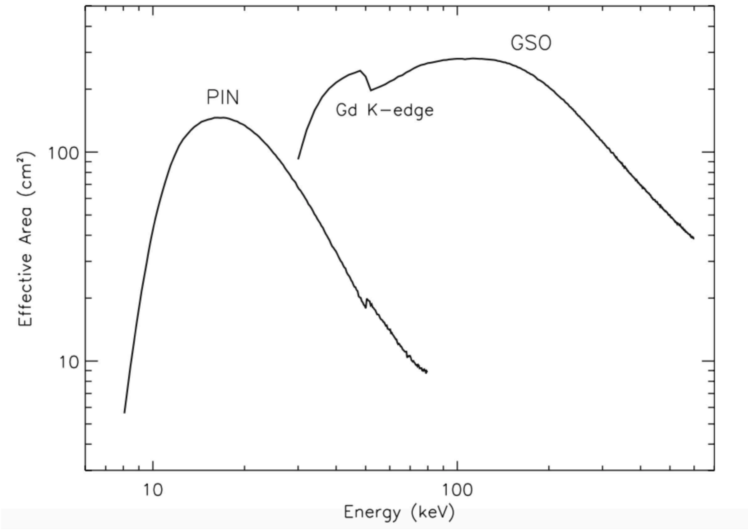

Figure 2.7: The total effective area of the HXD detectors, PIN and GSO, are presented as function of energy (Takahashi et al. 2007)

## 2.3 *Suzaku* Data Reduction

The data reduction presented in this section was applied to all the *Suzaku* observations of the sources analysed in this thesis. They were carried out with both the X-ray Imaging Spectrometer (XIS) and the Hard X-ray Detector (HXD). The targets were placed at the nominal center of the XIS field of view. The event files used in our analysis for each single XIS observation were reprocessed on-board in two different editing modes: 3 × 3 and 5 × 5. The editing modes specify how detected events are edited and determine the formats of the XIS data telemetry. In particular, in the 3 × 3 editing mode the pulse heights of the 9 pixels entering the event centre are sent to telemetry, while in the 5 × 5, the 25 pixels around the event centre are considered. The cleaned event files of both modes were combined in our analysis. We reprocessed the unfiltered event files of both the XIS and HXD by using the calibration files (CALDB) of 2013-01-10.

The standard reduction procedure was applied to the XIS data using the powerful *aepipeline* tool. This task runs all the standard calibration steps, in particular Assign Arrival times, Calibrate Sky Coordinates, Assigning Pixel Quality, Compute PI, Compute GTI and Add Microcode. After the calibrations, the `aepipeline` screens the event file following the criteria in Table 2.4.

| Type | Criterion | Comments |
|---|---|---|
| Event by event | `GRADE=0:0 2:4 6:6` | *ASCA* grades indicating X-ray events |
| | `STATUS=0 : 524287` | Bad columns, charge injection rows removed |
| | `cleansis` | Flickering pixels are removed |
| GTI | `AOCU_HK_CNT3_NML_P==1` | Attitude control in pointing mode |
| | `ANG_DIST` < `1.5` | Instantaneous pointing within 1.5 arcmin of mean |
| | `Sn_DRATE` < `3` | Telemetry rate SuperHigh, High or Medium |
| | `SAA_HXD==0` | Satellite is outside SAA |
| | `T_SAA_HXD` > `436` | time since SAA passage > 436 sec |
| | `ELV` > `5` | Pointing direction > 5 deg above Earth |
| | `DYE_ELV` > `20` | Pointing direction > 20 deg above sunlit limb of Earth |

Table 2.4: XIS screening criteria.

Using the *XSELECT* tool, XIS source spectra were extracted from circular regions with a radius of 250 arcsec, centered on the sources. This extraction radius encircles 99% of the point source flux and is recommended by the *Suzaku* team. The XIS background appears to be non-uniform over the CCD chip (Yamaguchi et al. 2006) because of the presence of several calibration sources, in particular at the chip corners. For this reason we decided to select the background regions as large as possible and avoiding the source, in order to have a better estimation of the background spectra. Figure 2.8 presents an example of images of IC 4329A. We show the extracting regions for the source spectrum (circle) and the background spectrum (rectangular), selected following the criteria presented above. As it is shown in Figure 2.8, no contaminating sources are present in the field of view of the XIS in any of the observations analyzed in this work.

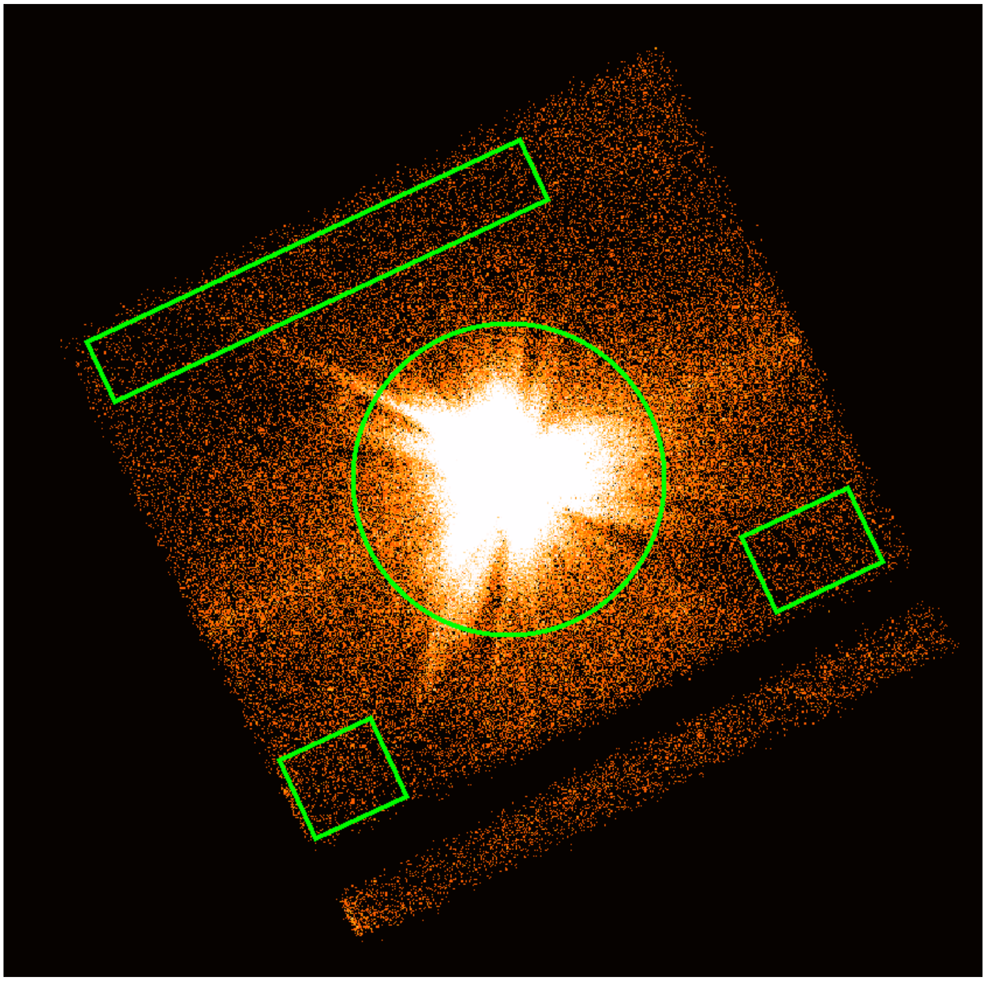

Figure 2.8: An example image of IC 4329A from the XIS instrument. The extracting regions for the source spectrum (circle) and the background spectrum (rectangle) are shown.

The `xisrmfgen` and `xissimarfgen` tools were used to create the Redistribution Matrix File (RMF) and the Ancillary Response Function (ARF). The first one is an instrument response file that describes how photons of different energy are redistributed into the various energy channels of the instrument, while the second expresses the effective area of the instrument in surface units ($cm^2$) as a function of photon energy. We combined the spectra of the XIS0 and XIS3 using `mathpha`, while the response matrices and the ancillary response files were added with the `addrmf` and `addarf` tools. The source spectra were grouped in order to have at least 100 counts per bin.

The PIN data were reduced using the standard procedure, as presented in the *Suzaku* ABC guide[2]. We use the `aepipeline` task to calibrate and screen the unfiltered event file. In particular the calibration steps include Time Assignment, Gain History Generation, PI Assignment and Grade Assignment. For the screening procedure, the `aepipeline` applies

---

[2] http://heasarc.gsfc.nasa.gov/docs/suzaku/analysis/abc/

the criteria reported in Table 2.5.

| Type | Criterion | Comments |
|---|---|---|
| Event by event | `DET_TYPE=0` | GSO events |
| | `DET_TYPE=1` | PIN events |
| | `DET_TYPE=2` | Pseudo events |
| GTI | `AOCU_HK_CNT3_NML_P==1` | Attitude control in pointing mode |
| | `HXD_HV_Wn_CAL_` > `700` | High voltage is not reduced |
| | `HXD_HV_Tn_CAL_` > `700` | High voltage is not reduced |
| | `SAA_HXD==0` | Satellite is outside SAA |
| | `T_SAA_HXD` > `500` | Time since SAA passage > 500 sec |
| | `TN_SAA_HXD` > `180` | Time to next SAA passage > 180 sec |
| | `COR` > `6` | Cut-off Rigidity > 6 GeV |
| | `ELV` > `5` | Pointing direction > 5 deg above Earth |
| | `HXD_DTRADE` < `3` | GSO only |
| | Telemetry is unsaturated | `aeNNNNNNNNNhxd_0_tlm.gti` |

Table 2.5: PIN screening criteria.

The source and the background spectra were then extracted from the cleaned event files, using *XSELECT* tool. The spectra were corrected for dead time and the exposure of the background spectra were increased by a factor of 10, since the event rate in the PIN background event files is 10 times higher than the real background to suppress the Poisson errors. The sum of the "tuned" non X-ray Background (NXB) spectra and simulations of the Cosmic X-ray Background (CXB) was adopted as PIN background in the spectral analysis. The CXB is simulated from a typical model provided by the *Suzaku* team (Boldt 1987). It is known that the detected spectrum can be different from that model, due to spatial fluctuations of the intrinsic CXB. These fluctuations are known to be of 10% from place to place on scales of 1 sq degree (Barcons et al. 2000). In those cases where the PIN background has important uncertainties and the source flux is relatively low, the reliability of the PIN data can be affected. Since the CXB corresponds only to 5% of the total background spectrum (Fukazawa et al. 2009), the fluctuations on the total PIN background are dominated by the uncertainties of the NXB, which are measured to be of the order of 3%. Considering all these issues, we decided to use the PIN spectrum only in cases where the source spectrum is more than 20% of the background, to avoid being dominated by background uncertainties. After this analysis, the PIN spectra were grouped in order to have at least 40 counts per bin after background subtraction.

## 2.4 *NuSTAR*

The Nuclear Spectroscopic Telescope Array (*NuSTAR*) satellite (Harrison et al. 2013) is composed of two co-aligned focusing hard X-ray telescopes (FPMA and FPMB). They have a focal length of 10m, fixed by an extendible mast which was deployed after launch (see Figure 2.9). The instrument has built in aspect and alignment metrology, provided by a laser alignment system and a star tracker head mounted on the optics bench. Table 2.6 presents the principal instrument performance characteristics.

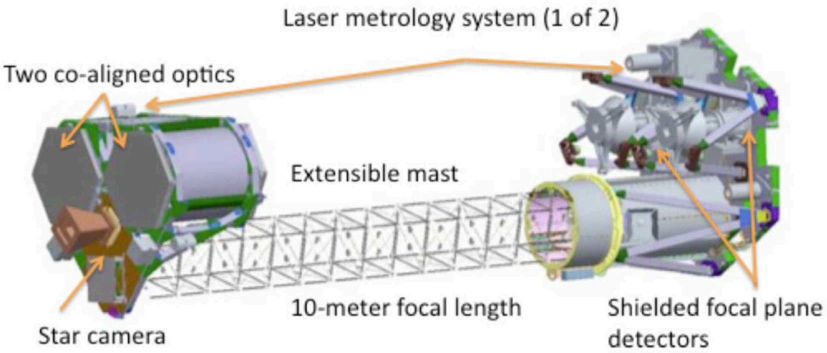

Figure 2.9: A scheme of the *NuSTAR* principal components.

| | |
|---|---|
| Energy band | 5-80 keV |
| Half Power Diameter | 43” |
| PSF FWHM | 7.5” |
| Energy resolution (FWHM) | 0.6 keV at 10 keV / 1.2 keV at 68 keV |
| Strong src. localization | 1.5” (1-$\sigma$) |
| Temporal resolution | 0.1 msec |
| ToO latency | 2-24 hr |
| Field of view (50% area) | 10’ at 10 keV / 8’ at 40 keV / 6’ at 68 keV |

Table 2.6: Key parameters of *NuSTAR* (Harrison et al. 2013).

## 2.4.1 Optics

The optics consist of two highly-nested, low graze angle, multilayer coated shells in a conical approximation of a Wolter-I geometry. The *NuSTAR* optics have smaller average graze angle, which is the angle between the incident X-ray and the optics shell, than the other soft X-ray telescopes such as *XMM-Newton* or *Chandra*, thus they have a smaller field of view. Vignetting is important over the sensitive field, so that the effective area falls towards the edge of the field of view.

The Point Spread Function (PSF) of the FPMA and FPMB *NuSTAR* optics is sharply peaked and has broad wings (Figure 2.10). It can be modelled with a King's function as a convenient parametrization. The FWHM is 7.5”, while the Half Power Diameter (HPD) is estimated to be between 40” and 45” (see Table 2.7).

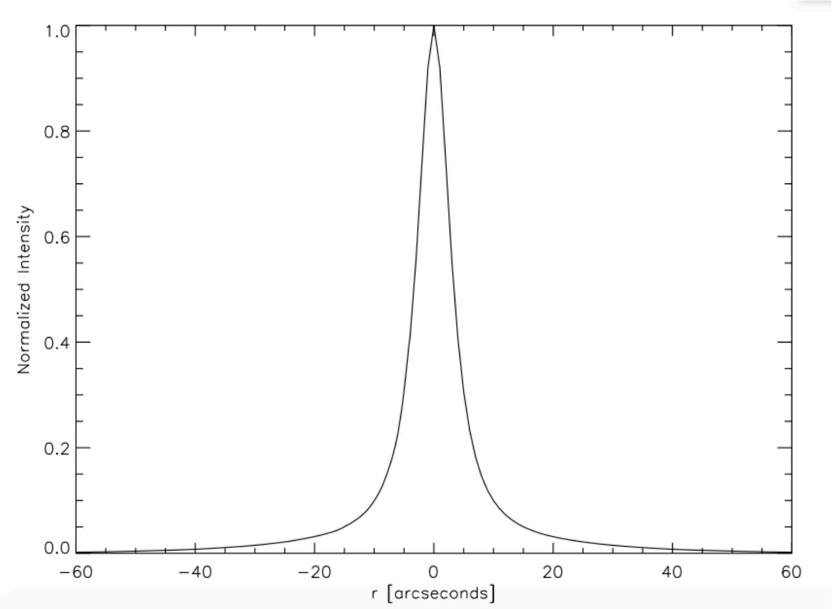

Figure 2.10: Point Spread Function of the FPMA and FPMB *NuSTAR* optics. It has a sharp core and broad wings. 50% of a point source flux is enclosed in a diameter of 45", while the FWHM is 7.5 ".

| Encircled energy fraction | Diameter (arcsec) |
|---|---|
| 50% | 43 |
| 70% | 75 |
| 80% | 101 |

Table 2.7: Encircled energy fraction for *NuSTAR* optics.

### 2.4.2 Detectors

The focal plane of each *NuSTAR* telescope consist of 2 × 2 array of imaging CdZnTe pixel detectors and the optical axis intersects the detector off-center in order to avoid the dead area between the detectors. There are four detectors onboard *NuSTAR* and each of them has a 32 × 32 array of pixels on a 0.6 mm pitch, corresponding to an angle on the sky of 12.3"/pixel. The dead gap between the detectors is on average 0.5 mm, but cannot be greater than 0.75 mm. The pixel detectors have readout electronics triggered each time an X-ray is detected. The processing time is 2.5 milliseconds, limiting the rate at which events can be read out to between 300 and 400 evts/s.

Because the reflectance is dependent on the graze angle and on the energy, the FWHM of the optics as a function of off-axis angle decreases with the X-ray energy. The low energy threshold is defined by the detector pixel trigger threshold of ∼3 keV. The detector quantum efficiency slightly increases between 3 and 6 keV because the events with energies divided in different pixels become more easily detected. Moreover, the collecting area of the telescopes increases between 5 and 10 keV as the optics thermal covers and detectors entrance window become more transparent. Finally, above 10 keV the effective area decreases due to decreasing of the reflectance of the coating above the critical angle for total external reflection. Figure 2.11 shows the effective collecting area of *NuSTAR* compared to selected operating focusing telescopes. The focusing capability is extended up to 79 keV compared to the other X-ray missions and combined with the good resolution in the hard X-ray range (FWHM response of 400 eV at 10 keV and 0.9 keV at 60 keV), the *NuSTAR* spectra allow us to optimally study the hard X-ray sky. These features complement the superior sensitivity and energy resolution of the other telescopes in the soft X-ray band, in particular that of *XMM-Newton* and *Suzaku*.

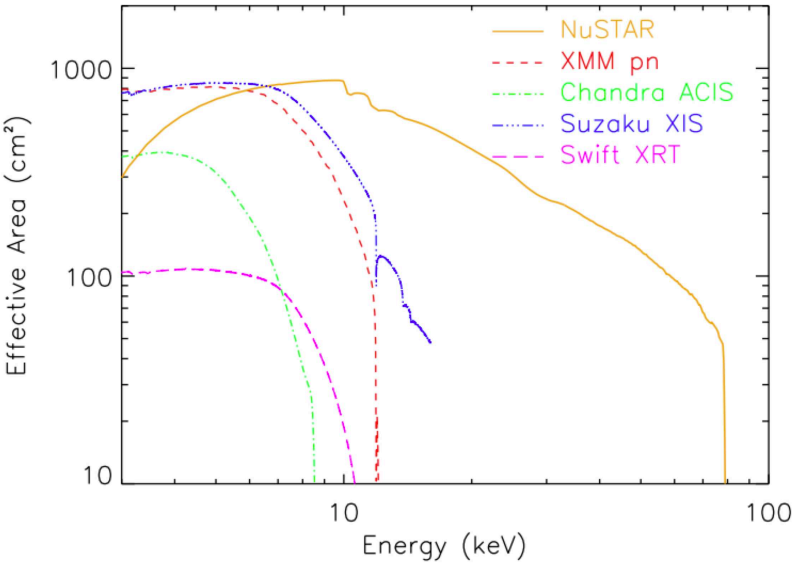

Figure 2.11: Effective collecting area of *NuSTAR* compared to other operating focusing telescopes: *XMM-Newton*, *Chandra* ACIS, *Suzaku* XIS and *Swift* XRT.

## 2.5 *NuSTAR* Data Reduction

We processed the *NuSTAR* data following the standard procedure presented in the *NuSTAR* Data analysis Software Guide[3]. Data from both the Focal Plane Modules (FPMA and FPMB) were processed. The unfiltered event files were analysed using the *nupipeline* (version 0.4.3). The Stage 1 of this task includes the processing of the data from the laser metrology system, the measuring the observatory mast alignment temporal changes and the correction of the spacecraft attitude file. The next stage of the data reduction involves screening the event files by applying cleaning criteria based on specified attitude/orbital/instrument parameters and event properties, using the latest calibration files available in the *NuSTAR* calibration data base (CALDB 2015-03-20 release). It includes

---

[3] https://heasarc.gsfc.nasa.gov/docs/nustar/analysis/nustar_swguide.pdf

also the generation of sky exposure maps. The output of this task are calibrated and cleaned event files which are used for the subsequent analysis.

Source spectra were extracted from these cleaned event files from circular regions of 90 arcsec centered on the source, exceptions to this value will be reported in each individual case. Background regions were made as large as possible avoiding the source and the corners of the CCD. Figure 2.12 present an example of extracting region for the source and background spectra. The object is IC 4329A and the image refers to the FPMA instrument onboard of *NuSTAR*.

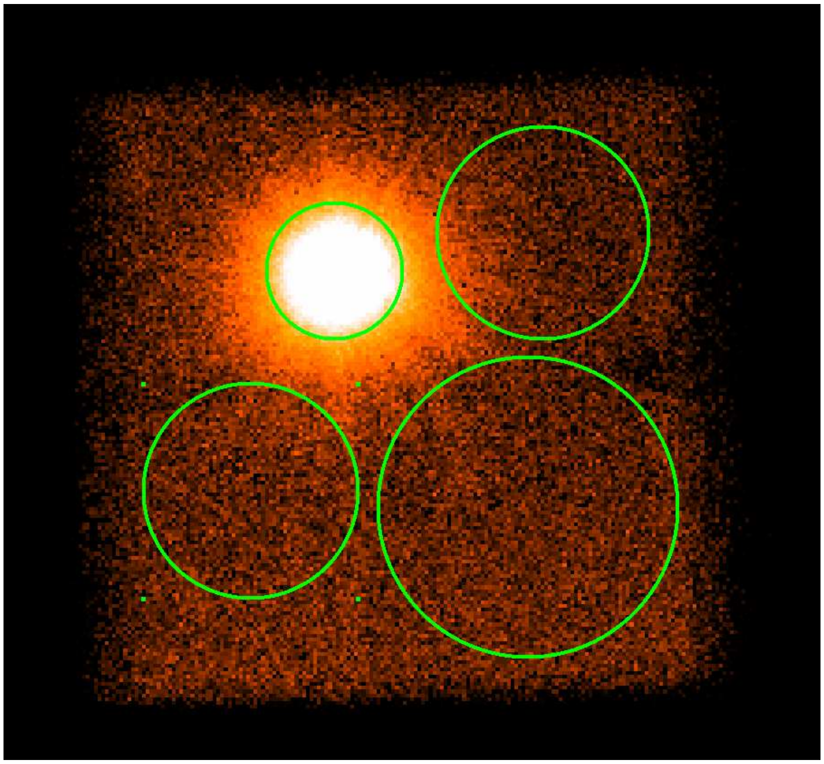

Figure 2.12

We next used the task `nuproducts`. This module extracts high-level data products from the cleaned event files, applying the backscale correction to the energy spectra, which is accounting for the exposure variations within the extracting regions of the background and source, and the livetime, PSF/EXPOSURE and vignetting corrections to the light-curves. Finally, it generates the ARF file for an input PHA file and the RMF file for an input spatial region file. After this analysis, the spectra were grouped in order to have at lest 40 counts per energy bin, in order to be able to apply the Chi Squared statistics. In the fitting process, we allow the cross-normalization factor between the FPMA and the FPMB modules spectra to vary freely.

# Chapter 3

# Relativistic Reflection Signature in IC 4329A

## 3.1 Introduction

One of the aims of this work is to investigate the presence of relativistic reflection signatures, in particular of the relativistic Fe K$\alpha$ line and its relation with the emission at higher energies, i.e. the Compton hump. As presented in Section 1.6, complete samples of Seyfert 1 objects, observed with *XMM-Newton* and *Suzaku*, were analyzed and a large fraction of them did not show the presence of the relativistic Fe line. However, such a broad feature should always be detected in Seyfert 1 objects if the accretion disk extends down to the last stable circular orbit. Several hypothesis have been proposed to explain the lack of detection of this spectral feature. One possible explanation to this result is the low signal-to-noise ratio of the single observation analyzed. Low statistics of the data might prevent us from disentangling such a broad feature from the underlying continuum. We aim to investigate this issue in one of the brightest objects in X-rays, IC 4329A. The analysis of previous *XMM-Newton* observations showed the absence and/or low significance relativistic line detection in this source. To do that, we decided to analyze *Suzaku* observations, because these spectra allow us to study also the relation between both the narrow and broad Fe K$\alpha$ line and the Compton hump flux.

### 3.1.1 IC 4329A

IC 4329A is one of the brightest Seyfert 1 galaxies in the local universe. This spiral galaxy is seen almost edge-on and is the closest companion to the elliptical galaxy IC 4329, the central galaxy in a cluster. On the basis of the optical reddening ($A_V$ = 2.5 - 4.8 magnitudes) Wilson & Penston (1979) have classified IC 4329A as the nearest quasar, with an absolute magnitude between -23.0 and -25.3. The optical spectra display prominent Na I D, Ca II and weaker Mg I absorption lines, consistent with the dust lane observed in the equatorial plane of the galaxy (Wilson & Penston 1979). The optical spectrum also shows that the absorber is neutral or of very low ionization. The redshift of IC 4329A is 0.01605

± 0.00005 and the Galactic hydrogen absorption column density is assumed to be $N_H = 4.55 \times 10^{20}$ cm$^{-2}$ (Elvis et al. 1989).

IC 4329A is the second brightest hard X-ray Seyfert 1 ($F_{2-10keV} \sim 2 \times 10^{10}$ ergs cm$^{-2}$ s$^{-1}$). The X-ray spectrum can be fitted with a simple power law with a photon index of $\sim 2$, plus a strong Compton reflection component, typical for Seyfert 1 galaxies (Madejski et al. 1995). The nature of the iron K-complex has been controversial, in particular regarding the presence or not of broad component of the Iron K$\alpha$ line. The analysis of simultaneous *ASCA* and *RXTE* observations (Done et al. 2000) showed the presence of a moderately broadened (FWHM = 43,000 ± 11,000) Fe K$\alpha$ line with an equivalent width of EW = 180 ± 50 eV peaking at $\sim$ 6.4 keV. Although the line is significantly broadened, the broadening is not as what expected from an accretion disk extended to the last stable orbit around a black hole. Previous work based on *ASCA* observations showed similar results (Nandra et al. 1997). A narrow core for the iron K$\alpha$ line (EW = 43 ± 1 eV) was detected in an *XMM-Newton* observation, reported by Gondoin et al. (2001), consistent with being produced by neutral material. A purely narrow emission together with a moderately broadened iron line, similar to the *ASCA* observation, were found in two *XMM-Newton* observations of this source (Nandra et al. 2007). An accurate view of the Fe line complex in IC 4329A was provided by McKernan & Yaqoob (2004), using a 60 ks high resolution *Chandra-HETGS* observation, showing the presence of a narrow core of the 6.4 keV line together with an additional narrow emission line near 6.9 keV. This double-peaked feature can be reproduced by different models, including double Gaussians, double or single disk lines. The same *Suzaku* observations considered in our work were analyzed by Patrick et al. (2012). The authors compiled a sample of Seyfert 1 objects, with available archival *Suzaku* observations. In IC 4329A, a relativistic line was detected in the stacked spectrum with an equivalent width of $69^{+13}_{-14}$ eV. Recently this source has been observed simultaneously by *Suzaku* and *NuSTAR* (Brenneman et al. 2014a). The high quality broad-band spectrum of *NuSTAR* allowed the authors to separate the reflection component arising from the distant material from the primary continuum emitted by the corona. Therefore, it was possible to precisely measure the high energy cut-off of the primary power law component to be $E_c = 178^{+74}_{-40}$ keV. Brenneman et al. (2014b) performed the spectral analysis of the *NuSTAR* and *Suzaku* spectra, investigating the Fe energy band in details. Together with the narrow component, only a moderately broad Fe K$\alpha$ line was detected using a simple gaussian model with an equivalent width of $34^{+6}_{-9}$ eV. Because this source was observed only once, it was not possible to constrain any parameters of the relativistic model for the Fe K$\alpha$ line. Finally, Markowitz et al. (2006), Nandra et al. (2007) and Tombesi et al. (2010) reported the possible presence of a blue shifted absorption line in an *XMM-Newton* observation of IC 4329A, which may be the signature of a very fast outflow.

In order to study the nature of the iron line and the reflection component in the Seyfert 1 galaxy IC 4329A, we analyzed archival *Suzaku* observations of this source. With its large effective area, this X-ray telescope provides a unique opportunity to determine the nature of the iron K$\alpha$ emission line. Moreover, its broad bandpass allows us to simultaneously fit both the narrow and the broad Fe line components and their associated emission at higher energies, investigating their relationship.

## 3.2 Data Analysis

IC 4329A was observed 5 times with *Suzaku* in 2007 on August 1, 6, 11, 16, 20 with an exposure time of $\sim$ 26 ks for each observation. X-ray Imaging Spectrometer (XIS; Koyama et al. 2007) and Hard X-ray Detector (HXD; Kokubun et al. 2007) event files were reprocessed as described in Chapter 2. The XIS and PIN spectra were analyzed together, considering a cross-normalization constant for both instruments. We fixed to 0.994 the value for the XIS spectrum and to 1.164 that for the PIN data, as appropriated for data taken at XIS nominal position (Maeda et al. 2008).

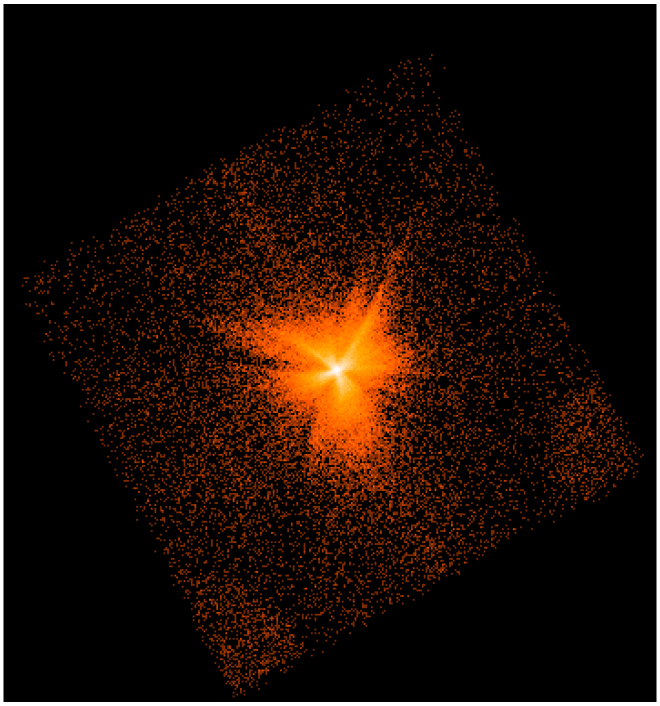

Figure 3.1: An example image of the source IC 4329A from the XIS instrument.

Figure 3.1 shows an example image from the XIS instrument of IC 4329A. The bright source is clearly visible in the center of the CCD. It is also possible to note the presence of the calibration sources at two bottom corners of the detector. These parts of the CCD were excluded from the extracting regions of the source and background spectra.

Figure 3.2 shows the light curves of the source in the XIS energy band for each observation, presented in chronological order. The black line shows the mean counts per second for each observation. The light curves from the XIS0 and XIS3 instruments were summed together after background subtraction. The bins in all the light curves are 150 s. The source is highly variable within each observation (up to a factor of $\sim$ 1.5) in particular in the first three observations. The average counts per second in each light curve are 12.70, 14.07, 12.84, 12.17 and 7.49, respectively. From the light curves it is possible to note that the source is highly variable from time scales of 150 s (bin size), within each single observation, to time scales of 20 days. The latter is given by the time scale in which the five observations were taken. We are going to investigate the spectral variability in more detail in Section 3.2.4.

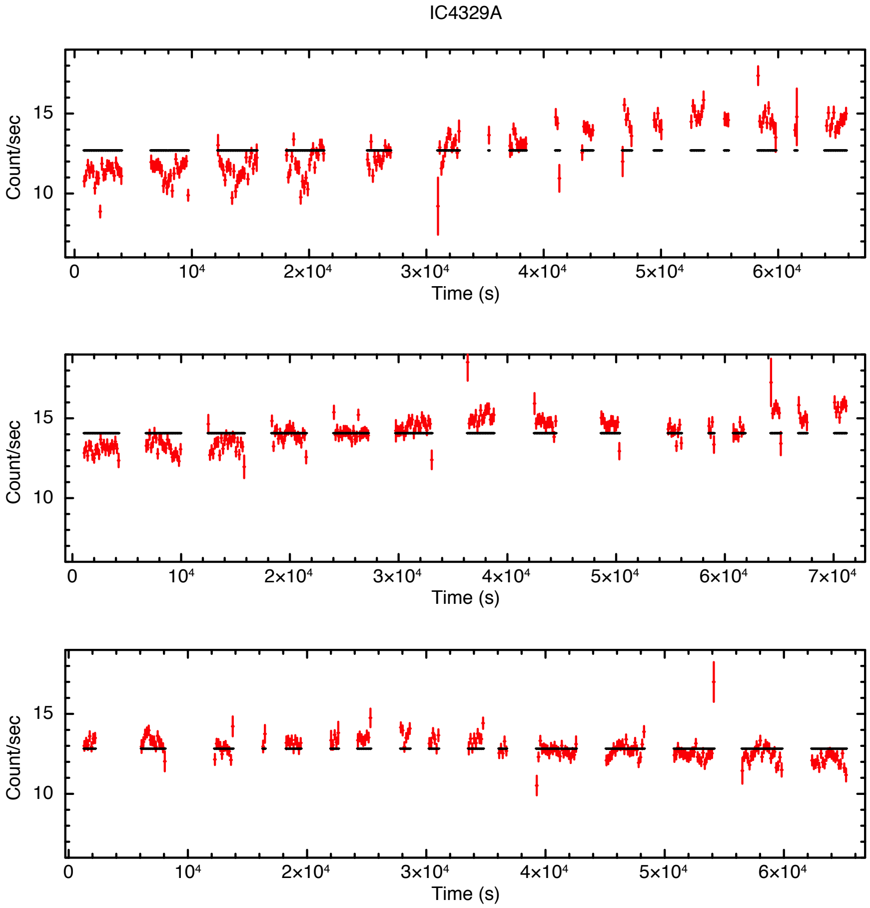

Figure 3.2: Light curves of each observation for IC 4329A in chronological order. The XIS0 and XIS3 light curves were combined after the background subtraction. The bins in all the light curves are set to 150 s.

### 3.2.1 Baseline Model

We begin the spectral analysis of IC 4329A by fitting the data to a simple model. The Baseline model includes a neutral absorber at the redshift of the source (*zwabs*) and a power law together with a Compton reflection component (*pexrav*; Magdziarz & Zdziarski 1995). The inclination of the distant reflector was fixed to 60° and we assumed solar Fe abundance. The column density was left free to vary. We found a mean value for this parameter of $N_H = 0.4 \times 10^{22}\ cm^{-2}$. Subsequently we fixed the column density to this value.

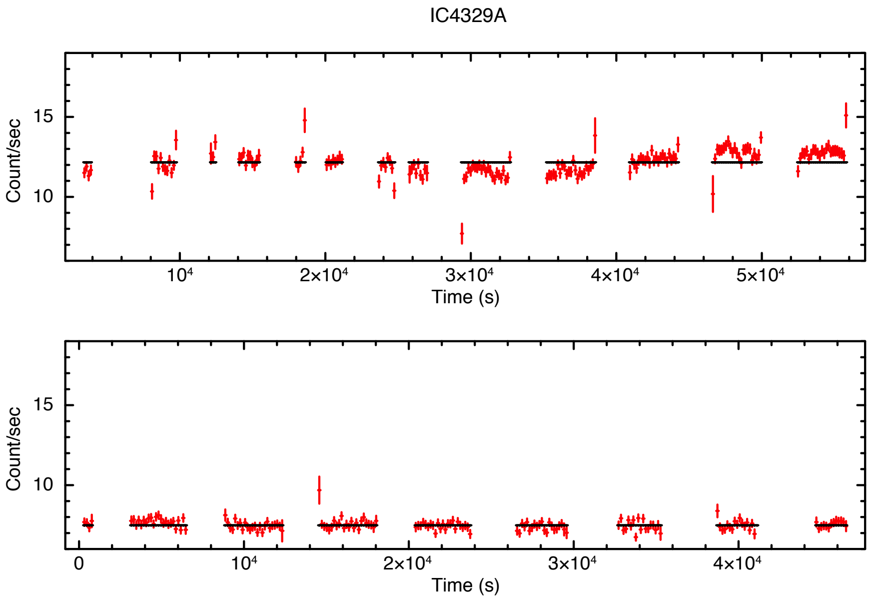

Figure 3.2: (Continued) Light curves of each observation for IC 4329A in chronological order. The XIS0 and XIS3 light curves were combined after the background subtraction. The bins in all the light curves are set to 150 s.

Figure 3.3 shows the data to model ratio for each observation for both the XIS and PIN spectra. The left panels present the data to model ratios when the Baseline model is applied to the data. Clear residuals are present at the energy of the Iron K$\alpha$ line (6.4 keV) in all 5 observations. These could be due to a blend of narrow and broad Fe K$\alpha$ lines. The right panels show the data to model ratios when a narrow gaussian component is included in the previous model (see Section 3.2.2 for more details). We are going to investigate the Fe complex for each observation in the next Section.

### 3.2.2 Line models

After modelling the primary continuum together with the reflection component, we tested whether the residuals present in the Fe energy band could be explained only with emission from distant material (see left panels of Figure 3.3). We thus fitted the XIS and the PIN spectra simultaneously with the Gaussian model: *zwabs*(pexrav+zgauss)*. This includes a neutral absorber at the redshift of the source (*zwabs*), a power law continuum together with a reflection component (*pexrav*) and a gaussian component for the narrow Fe emission line (*zgauss*). The width of the gaussian model was fixed to $\sigma = 1$ eV, while the energy and the flux of this component were allowed to vary. The inclination of the distant reflector was fixed to 60°, whilst the Fe abundance was also fixed to the solar value. As a first step, we allowed the high energy cut off to vary. We measured a mean value for this parameter between the 5 observations of 180 keV and subsequently adopted this as a fixed parameter in the model. This measurement is in agreement with the recent value of $178^{+74}_{-40}$ keV found

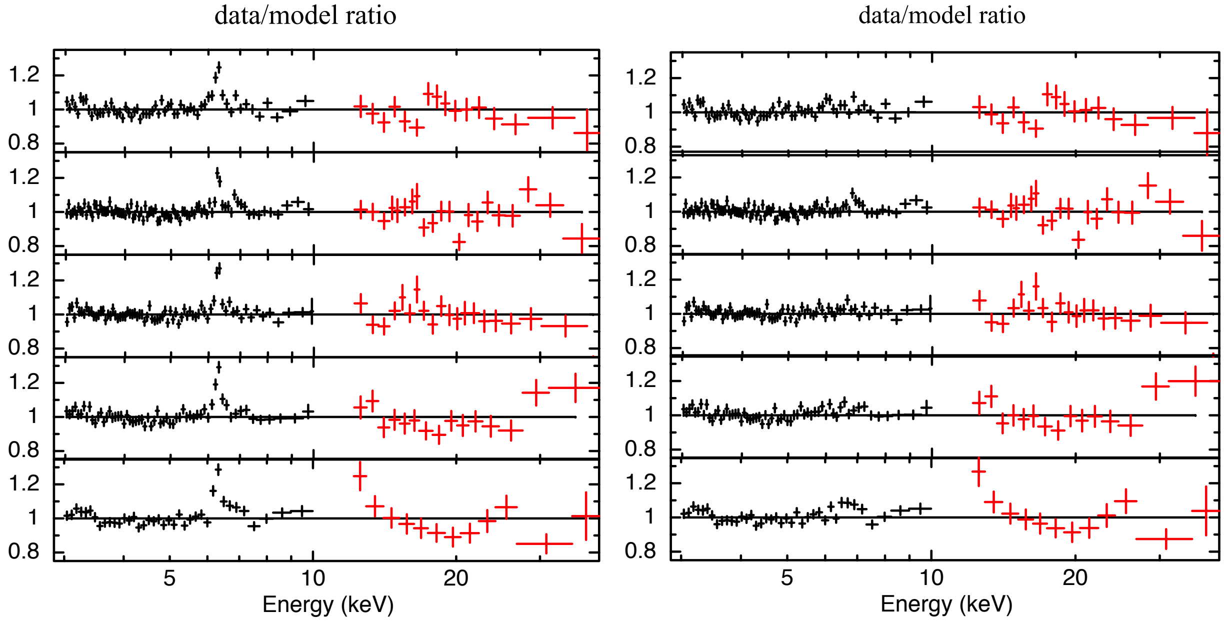

Figure 3.3: Data to model ratio of each observations. From top to bottom in both panels, the observations are in temporal order. *Left panels* show the ratios, when a neutral absorber at the redshift of the source and a reflection component is included in the model. A narrow Fe K$\alpha$ line is clearly present in the data. *Right panels* present the data to model ratios when a narrow gaussian component is included in the previous model (see Section 3.2.2 for more details.

by Brenneman et al. (2014b).

Table 3.1 presents the best fit parameters for the Gaussian model. The energy of the gaussian component is consistent within the errors with Fe K$\alpha$ line produced by neutral material. The values for the power law slope, as well as the normalization, are not consistent between the observations, showing a spectral variation of the continuum, which we are going to investigate in more details in Section 3.2.4.

Right panels of Figure 3.3 present the data to model ratios for each single observation, when the Gaussian model is applied to the data. The narrow gaussian model component is now fitting well the residuals around 6.4 keV. However, from visual inspection it is not straightforward to claim whether a relativistic Fe K$\alpha$ line is present in the spectra or not.

In order to test if the apparent lack of a broad Fe line component is due to the low signal-to-noise ratio in the single observation, we combined the data to model ratio presented in the left panels of Figure 3.3. Figure 3.4 shows the average data to best-fit Gaussian model ratio, in the 3-10 keV band. The model is reproducing well the narrow iron K$\alpha$ emission line. However, it leaves significant residuals around 6.4 keV. In particular, a broad component extending to lower and higher energies is clearly visible in the plot. It is important to note that each spectrum was fitted separately, in order to account for the variability of the source within the observations. This approach allows us to consider any variations of the continuum slope, which in theory might produce artificial residuals if the

| Gaussian | 702113010 | 702113020 | 702113030 | 702113040 | 702113050 |
|---|---|---|---|---|---|
| $\Gamma$ | $1.81 \pm 0.04$ | $1.90 \pm 0.03$ | $1.77 \pm 0.03$ | $1.82 \pm 0.04$ | $1.73 \pm 0.06$ |
| R | $0.78 \pm 0.23$ | $1.18 \pm 0.24$ | $0.79 \pm 0.20$ | $0.96 \pm 0.25$ | $1.56 \pm 0.48$ |
| Norm | $3.11 \pm 0.14$ | $4.12 \pm 0.16$ | $3.26 \pm 0.13$ | $3.18 \pm 0.14$ | $1.72 \pm 0.12$ |
| $E_{K\alpha}$ | $6.39 \pm 0.02$ | $6.40 \pm 0.01$ | $6.38 \pm 0.02$ | $6.40 \pm 0.02$ | $6.40 \pm 0.02$ |
| $F_{K\alpha}$ | $6.24 \pm 0.94$ | $5.81 \pm 0.92$ | $7.40 \pm 0.99$ | $7.54 \pm 1.00$ | $5.58 \pm 0.83$ |
| $F_{2-10keV}$ | $1.05 \pm 0.02$ | $1.25 \pm 0.02$ | $1.18 \pm 0.02$ | $1.08 \pm 0.02$ | $0.69 \pm 0.01$ |
| $F_{12-40keV}$ | $1.56 \pm 0.01$ | $1.82 \pm 0.01$ | $1.89 \pm 0.01$ | $1.68 \pm 0.01$ | $1.45 \pm 0.01$ |
| $F_{Comptonhump}$ | $2.43 \pm 0.86$ | $4.86 \pm 1.22$ | $2.58 \pm 0.78$ | $3.05 \pm 0.97$ | $2.68 \pm 1.09$ |
| $EW_{Fe_{K\alpha}}$ | $52 \pm 8$ | $42 \pm 7$ | $55 \pm 7$ | $62 \pm 8$ | $68 \pm 10$ |
| $\chi^2$ | 959.81/891 | 1117.19/1104 | 993.38/999 | 921.63/869 | 626.51/606 |

Table 3.1: Best-fit parameters for the Gaussian model. The continuum fluxes are in $10^{-10}$ erg s$^{-1}$ cm$^{-2}$ while the Normalizations (Norm) and the Compton Hump fluxes are in $10^{-2}$ photons keV$^{-1}$ cm$^{-2}$ s$^{-1}$. The Iron K$\alpha$ fluxes are in $10^{-5}$ erg s$^{-1}$ cm$^{-2}$. The energy of the line is in keV and the equivalent width is in eV.

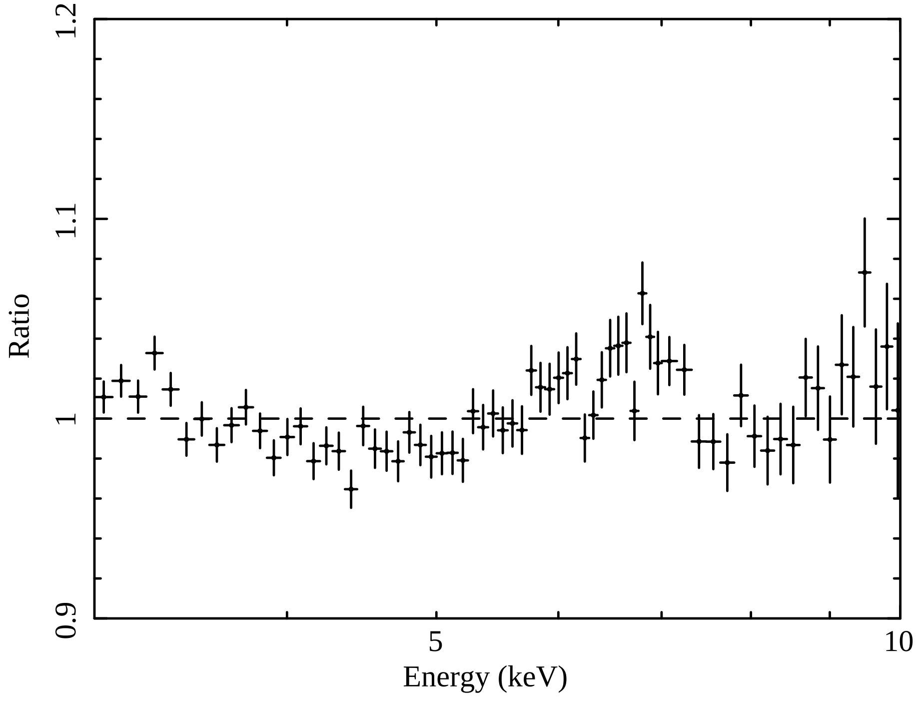

Figure 3.4: Combined data to model ratio for all the 5 observations. Each spectrum was fitted separately with the Gaussian model. It includes a single narrow Gaussian model together with a power law component and a Compton reflection component. A broad iron line, which is not visible in the individual spectra (right panels of Fig. 3.3), is evident in the combined residuals.

spectra are stacked before fitting with an average model. This result is consistent with Nandra et al. (2007). They pointed out by simulations that such a variable continuum does not produce false broad relativistic component in any case.

We then estimated the significance level of the broad component by introducing an accretion disk line component (*laor* model; Laor 1991) in the Gaussian model presented above. The rest energy of this line component was fixed to 6.4 keV, while the inner and outer radii ($R_{in}$ and $R_{out}$) to 6 and 400 $r_g$, respectively, being appropriated for the Schwarzschild metric. The emissivity index was fixed to q = 3 and a fixed inclination of 35° was also adopted (see below). We left the iron line flux as the only additional free parameter. The improvement in $\chi^2$ for each individual spectrum ranged from 3-18, corresponding to 2-4$\sigma$ based on the F-test. When all the improvements in $\chi^2$ are considered together, however, the significance level reaches 5.5$\sigma$ based on the same test.

### 3.2.3 Reflection model

To provide a more physically self-consistent model for the spectra, we used the *pexmon* model (Nandra et al. 2007). This model accounts for the Compton reflection and iron K$\alpha$ emission from neutral, optically thick material in a slab geometry. The *pexmon* model combines: i) narrow Fe K$\alpha$ at 6.4 keV; ii) narrow Fe K$\beta$ at 7.06 keV; iii) Ni K$\alpha$ at 7.47 keV; iv) Compton reflection (as the *pexrav* model) and v) Fe K$\alpha$ Compton shoulder. The Fe K$\beta$ and Ni K$\alpha$ line fluxes are linked with the Fe K$\alpha$ flux. In particular, they are 11.3% and 5% respectively of that for the 6.4 keV line (George & Fabian 1991). It is important to note, that this model is intrinsically linking the strength of the Fe K$\alpha$ line with the Compton reflection component at higher energies, being features of the same reflection spectrum.

We then applied the Reflection model: *zwabs*(cutoffpl+pexmon+kdblur2*pexmon)*. In order to model the continuum, we used a neutral absorber at the redshift of the source (*zwabs*) and a cut off power law (*cutoffpl*). Together with these component, we included two *pexmon* components, in order to account for the narrow core of the iron line and to test the presence of a broadened component. In the former, we fixed the inclination of the slab to 60°, parametrizing the strength of the reflection with the reflection fraction $R_N$. This measures the ratio between the reflection continuum and the power law component. For the blurred component, we convolved the *pexmon* with the *kdblur2* model (Crummy et al. 2006). This model broadens the reflection component appropriately to account for the relativistic effects close to the black hole. Following Nandra et al. (2007), we parametrized the emissivity of the reflection continuum by a broken power law with fixed indices of q = 0 and q = 3 above and below the break radius of $R_{break}$. This parameter was fixed to 20 $r_g$, while the inner and outer radii to 6 and 400 $r_g$, respectively. The iron abundance was fixed to solar in both *pexmom* models, and the spectral index $\Gamma$ was tied to the one of the cut off power law. We first allowed the inclination of the relativistic component (i.e. accretion disk) to vary. Then, we fixed this parameter to mean values found within the 5 observations of 35°.

Table 3.2 shows the best fit parameters for the Reflection model. This approach of

| Reflection | 702113010 | 702113020 | 702113030 | 702113040 | 702113050 |
|---|---|---|---|---|---|
| $\Gamma$ | $1.82 \pm 0.03$ | $1.85 \pm 0.02$ | $1.78 \pm 0.03$ | $1.83 \pm 0.03$ | $1.71 \pm 0.04$ |
| Norm | $3.15 \pm 0.12$ | $3.97 \pm 0.12$ | $3.31 \pm 0.11$ | $3.25 \pm 0.12$ | $1.69 \pm 0.08$ |
| $R_N$ | $0.38 \pm 0.07$ | $0.32 \pm 0.06$ | $0.36 \pm 0.06$ | $0.44 \pm 0.07$ | $0.46 \pm 0.09$ |
| $R_B$ | $0.29 \pm 0.13$ | $0.23 \pm 0.11$ | $0.26 \pm 0.12$ | $0.36 \pm 0.14$ | $0.47 \pm 0.18$ |
| $F_{2-10keV}$ | $1.05 \pm 0.02$ | $1.25 \pm 0.02$ | $1.18 \pm 0.02$ | $1.08 \pm 0.02$ | $0.69 \pm 0.01$ |
| $F_{12-40keV}$ | $1.53 \pm 0.01$ | $1.78 \pm 0.01$ | $1.87 \pm 0.01$ | $1.65 \pm 0.01$ | $1.42 \pm 0.01$ |
| $\chi^2$ | 942.25/891 | 1124.08/1104 | 987.78/999 | 899.82/869 | 610.57/606 |

Table 3.2: Best-fit parameters for Reflection model. The continuum fluxes in the 2-10 keV are in $10^{-10}$ erg s$^{-1}$ cm$^{-2}$ while the Normalizations (Norm) is in $10^{-2}$ photons keV$^{-1}$ cm$^{-2}$ s$^{-1}$. The Iron K$\alpha$ fluxes are in $10^{-5}$ erg s$^{-1}$ cm$^{-2}$. The energy of the line is in keV and the equivalent width is in eV. $R_N$ and $R_B$ correspond to the reflection fraction of the narrow and broad Iron line component, respectively.

modelling the spectra does not yield consistent spectral indices $\Gamma$ between the observations. This is in agreement with the analysis presented in the previous section. Both the narrow and the broad reflection components are clearly present in each spectrum, as indicated by the fact the their strengths (R$_N$ and R$_B$) are well constrained in the fits. This analysis confirms the conclusions from the visual inspection of Fig. 3.4 that a relativistically blurred Iron K$\alpha$ lines is present in each spectrum of IC 4329A.

We now want to test if ionised iron lines (such as Fe XXVI and Fe XXV) are present in these spectra. We found that, in addition to the 6.4 keV core and the broad component, two observations (Obs. ID: 702113020 and 702113050) show strong evidence for a Fe XXVI narrow emission line. We modelled these features, including a narrow gaussian component in the Reflection model. The line width was fixed to $\sigma = 1$ eV. The energies of these components were measured to be $6.94^{+0.04}_{-0.01}$ and $6.94^{+0.04}_{0.13}$ respectively for the two observations. These values are consistent with narrow Fe XXVI lines emitted from distant material. We then included these components in the Reflection model.

| Observation | Gaussian | Reflection | $\Delta\chi^2$ |
|---|---|---|---|
| 702113010 | 950.20/890 | 933.88/890 | 16.32 |
| 702113020 | 1097.46/1103 | 1100.35/1103 | -2.89 |
| 702113030 | 993.35/998 | 987.78/998 | 5.57 |
| 702113040 | 921.33/868 | 899.79/868 | 21.54 |
| 702113050 | 616.26/605 | 600.41/605 | 15.85 |

Table 3.3: Comparison of the $\chi^2$ of Gaussian and Reflection model when the highly ionised emission lines component at 6.94 keV are also included.

Table 3.3 shows the $\chi^2$ of the phenomenological model (Gaussian model) and the more physically self-consistent one (Reflection model). We also present the $\Delta\chi^2$ between these two models. Generally, the latter is giving a much better fit to the data. The only exception is the observations 702113020, where the $\chi^2$ is similar between the Gaussian and the Reflection model.

Finally, we tested for the presence of a high energy absorption line around 7.5 keV. This was first reported by Markowitz et al. (2006). None of the *Suzaku* spectra considered in this analysis shows any evidence for such a feature.

### 3.2.4 Spectral variability

In Section 3.2, we presented the light curves of the five *Suzaku* observations, which show a variable X-ray emission in IC 4329A. The spectral analysis shows that important parameters are varying between different observations. We investigated how these quantities change in the time scale spaced by the observations: $\sim$ 20 days.

The left plot of Figure 3.5 presents the variations of the power law slope as a function of time, while the right plot shows the variations of the continuum flux in the 2 to 10 keV energy band. These quantities are varying by a factor of $\sim$ 1.2 and $\sim$ 1.5, respectively. Moreover, the variability trend of the primary continuum presented in the right plot of Figure 3.5 is consistent with the variations of the averaged counts per second of the light curves (12.70, 14.07, 12.84, 12.17 and 7.49. See also Figure 3.2).

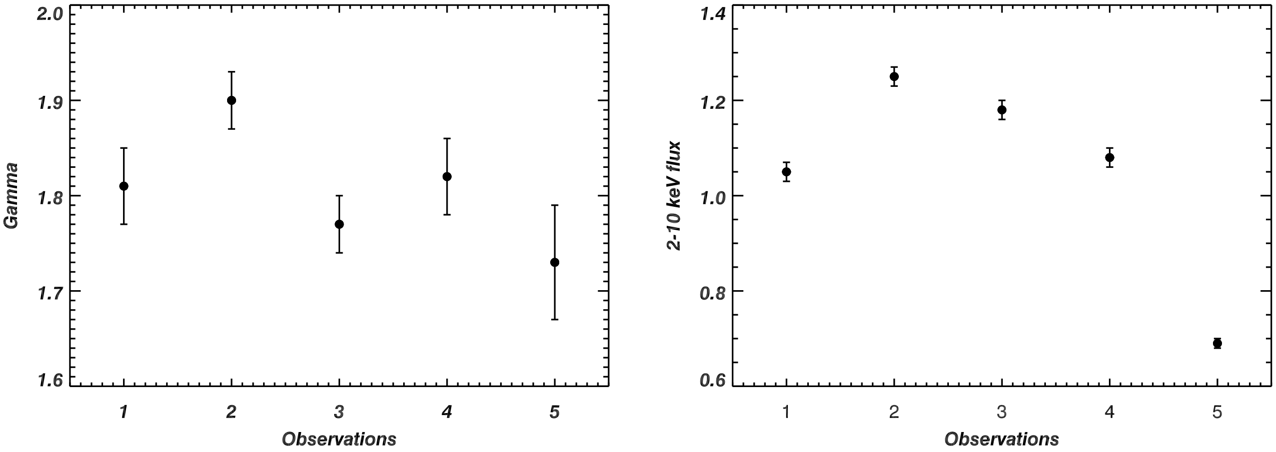

Figure 3.5: Variations of the power law slope parameter (left plot) and the continuum flux in the 2-10 keV energy band as a function of time. The flux is in unit of $10^{-10}$ *erg cm*$^{-2}$ s$^{-1}$

Figure 3.6 shows the Compton reflection flux and the narrow Fe K$\alpha$ flux as a function of time. The former has been calculated as the product between the normalization of the primary continuum and the reflection fraction $R$. The Fe flux is in unit of photons cm$^{-2}$ s$^{-1}$, while the Reflection flux is in photons keV$^{-1}$ cm$^{-2}$ s$^{-1}$. No significant variability for both quantities is detected.

Figure 3.7 presents the variability of the reflection fraction $R$ and the equivalent width of the narrow Fe K$\alpha$ line as a function of time. Both parameters show variations of a factor of 2 in the time scale investigated ($\sim$ 20 days). These quantities measure the amount of

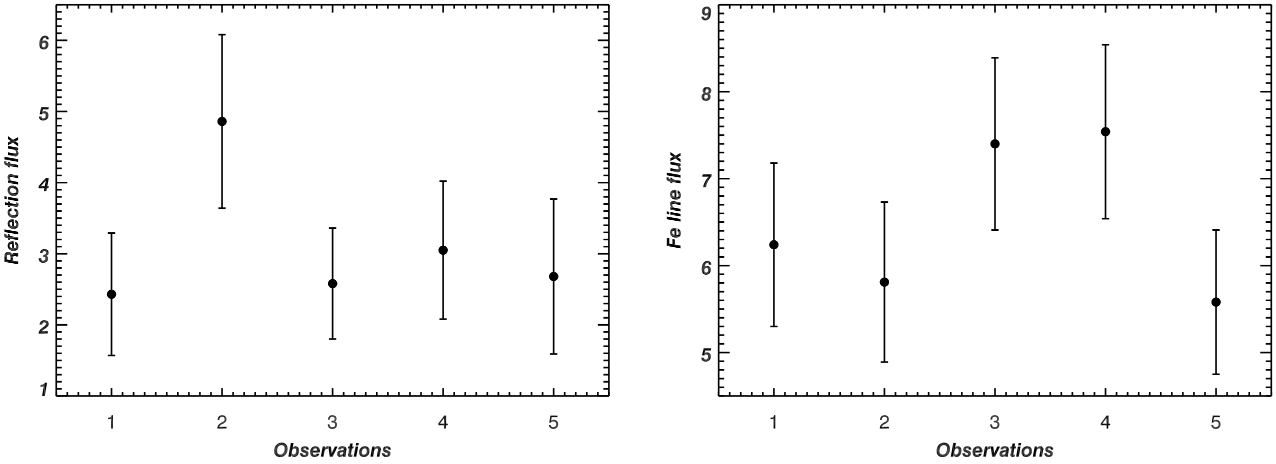

Figure 3.6: Variations of the Compton reflection component (left plot) and the narrow Fe line flux (right plot) as a function of time.

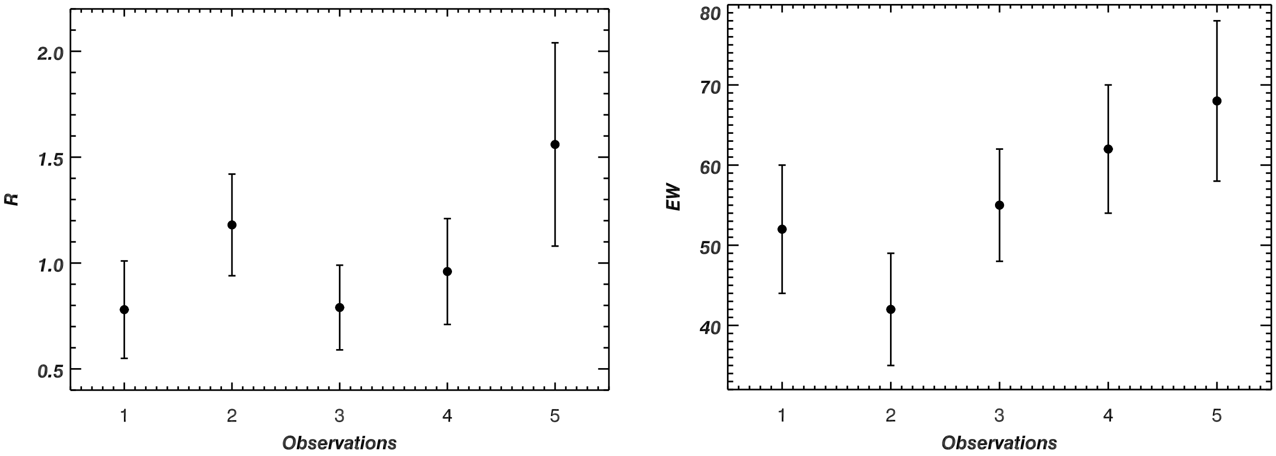

Figure 3.7: The reflection fraction $R$ (left plot) and the narrow line equivalent width (right plot) as a function of time.

reflection with respect to the primary continuum, at the energies of the Compton hump and the Fe line, respectively. If the amount of reflection detected in this spectra is only due to emission from distant material, a one-to-one relationship should be found between the equivalent width of the narrow Fe line and the reflection fraction $R$. We then investigated further the relationship between these parameters.

In the standard scenario (George & Fabian 1991), correlations between the continuum flux in the 2-10 keV band and the quantities associated to the reflection continuum are expected. This is due to the reflection spectrum being produced by the interaction of the primary X-ray continuum emitted by the corona onto the accretion disk and/or a distant reflector. We investigated whether these relationships are present in the data of IC 4329A.

Figure 3.8a shows the power law slope and the continuum flux, in units of $10^{-10}$ $erg\ cm^{-2}$

$s^{-1}$, in the 2-10 keV energy band for each observations. Some degree of correlation is seen here, but the significance is low ($\sim$ 70 % confidence). This result is consistent with previous works, where a correlation between these two quantities is commonly observed in AGN spectra (Leighly et al. 1996; Lamer et al. 2000; 2003; Ponti et al. 2006). Figure 3.8b shows the Compton reflection flux as a function of the primary continuum. The former is calculated as the product between the normalization of the primary power law and the reflection fraction $R$. Contrary to the expectations, we do not find correlation between these parameters.

Figure 3.8c presents the Fe K$\alpha$ line flux as a function of the primary continuum in the 2-10 keV energy band. A significant correlation is not present between these parameters. This could be due to the fact the the narrow Fe line arises from neutral distant material located at distances higher than the time scale tested with these set of observations ($\sim$ 20 days).

Lastly, Figure 3.8d and Figure 3.8e show no clear correlation between the reflection fraction R and either the equivalent width or the Fe K$\alpha$ line flux. If the reflection fraction $R$ from the *pexrav* component is only associated to the emission of the narrow Fe line, a one-to-one correlation should be present between $R$ and the narrow Fe line equivalent width. For the same reason, a linear correlation should also be detected between the narrow Fe line flux and the Compton reflection Component. The lack of those correlations is consistent with the presence of a broad component in these spectra, producing an higher amount of reflection compared to that expected from the narrow Fe line only.

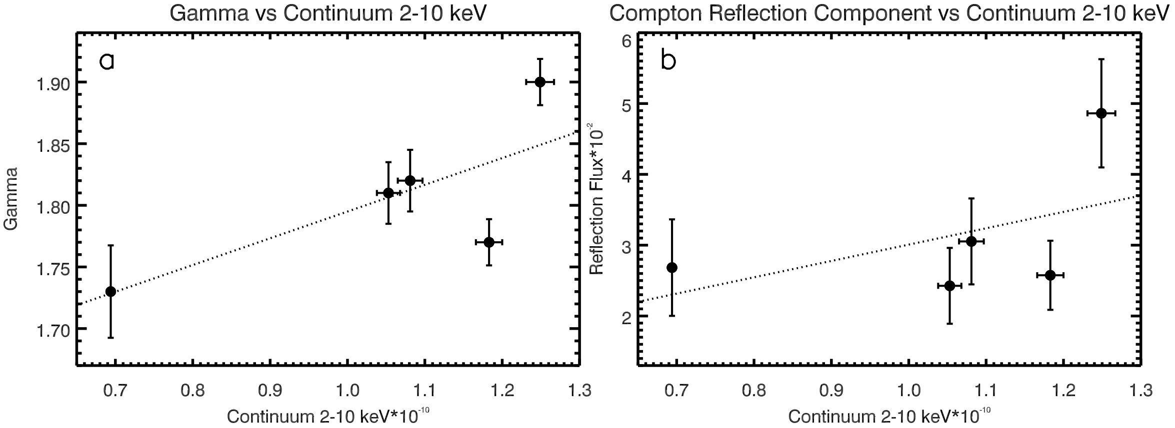

Figure 3.8: The upper three panels (a, b, c) plot $\Gamma$, reflection flux and iron line flux as function of continuum flux in the 2-10 keV band. The bottom panels (d, e) plot the Reflection Fraction as function of Equivalent Width, the Iron flux versus Reflection Flux. The continuum fluxes are in erg $cm^{-2}$ $s^{-1}$, the Iron fluxes are in photons $cm^{-2}$ $s^{-1}$ while the Reflection Fluxes are in photons $keV^{-1}$ $cm^{-2}$ $s^{-1}$. The dotted lines show the linear fit.

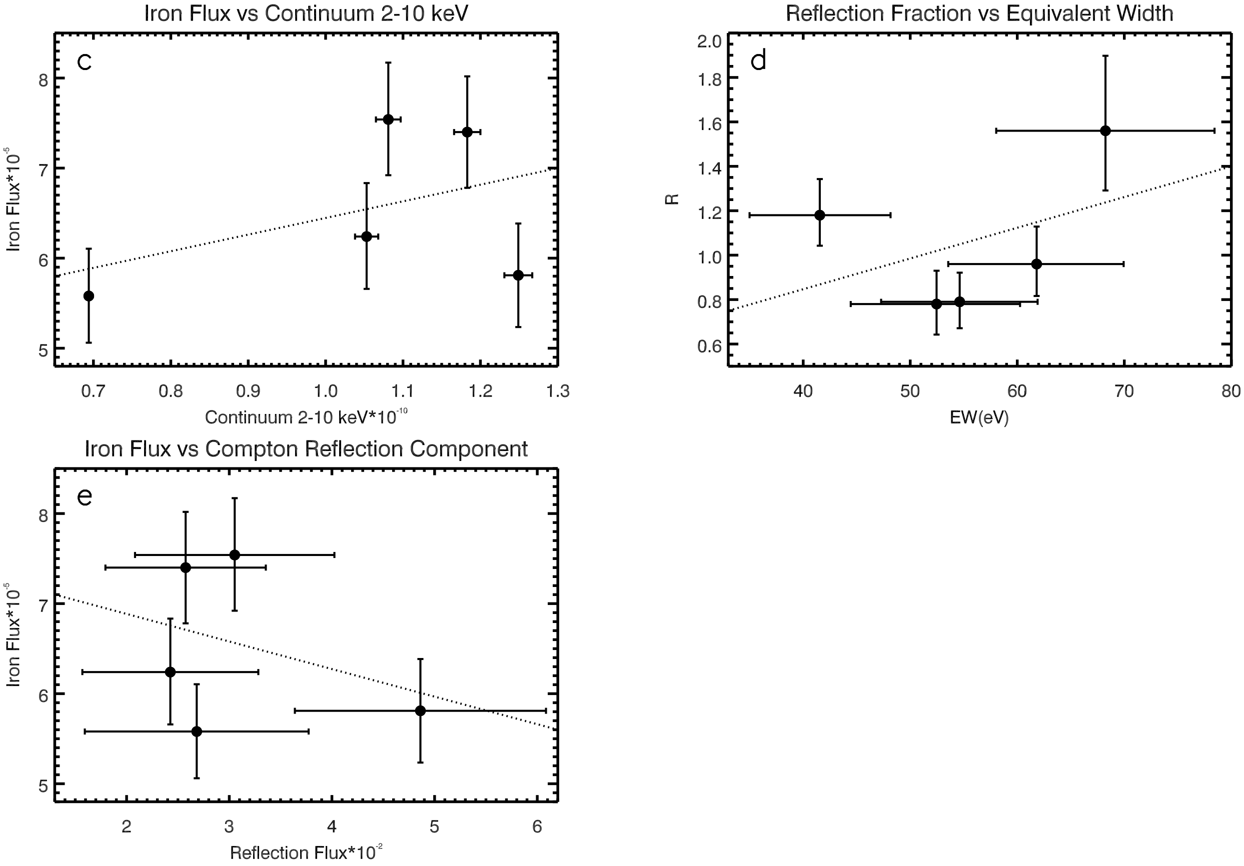

Figure 3.8: (Continued.) The upper three panels (a, b, c) plot $\Gamma$, reflection flux and iron line flux as function of continuum flux in the 2-10 keV band. The bottom panels (d, e) plot the Reflection Fraction as function of Equivalent Width, the Iron flux versus Reflection Flux. The continuum fluxes are in erg cm$^{-2}$ s$^{-1}$, the Iron fluxes are in photons cm$^{-2}$ s$^{-1}$ while the Reflection Fluxes are in photons keV$^{-1}$ cm$^{-2}$ s$^{-1}$. The dotted lines show the linear fit.

## 3.3 Discussion

We analyzed five *Suzaku* observations of the bright Seyfert 1 galaxy IC 4329A. The goal of this work was to determine the nature of the Fe K$\alpha$ emission and its relation with the Compton Hump. Our analysis shows the presence of a narrow core with an energy consistent to that produced by distant material. Once this narrow component is modelled and subtracted, important broad residuals in the Fe K energy band appear. However, these are clearly visible only when all data-to-model ratios are combined (see Fig. 3.4 and Fig. 3.3). These residuals can be easily reproduced if the emission originated in the inner parts of the accretion disk is modelled. In these regions, the Fe K$\alpha$ line and the reflection continuum are blurred by relativistic effects.

The apparent lack of relativistic features in the X-ray spectra of AGN - including IC

4329A - is a major outstanding issue in the standard accretion disk model for the feeding of AGN. If a relatively cold, optically thick accretion disk is assumed to be present around the central black hole and the X-ray primary emission interacts with this disk, the relativistic component must be present. The hypothesis of a disk truncation to large radii seems implausible because of the very high radiative efficiency of these systems and the fact that most of the energy dissipation is expected to occur in the central regions. Bhayani & Nandra (2011) have suggested in general, and in particular for this object, that strong relativistic effects, disk ionization and/or high disk inclination can explain the lack of the relativistic signatures in the AGN spectra. This is due to difficulties in disentangling a very broad feature from the underlying continuum. While these effects may be present in IC 4329A, the spectra are well fitted by a relatively simple, normal relativistic, reflection component from a neutral accretion disk with Schwarzschild geometry observed at relatively low inclination (35 deg). The difficulty in detecting the relativistic Fe K$\alpha$ component in IC 4329A derives from its relative weakness compared to the expectations from a semi-infinite flat disk geometry illuminated by a point source ($R_B \sim 0.3$ compared to $R \sim 1$). However, Murphy & Yaqoob (2009) pointed out that this geometry produces strong reflection signatures in the spectra. General relativistic effects close to the central black hole can also result in a reflection which is either stronger, or weaker, than the expectations, depending for example on the height of the primary source above the accretion disk (Miniutti et al. 2003). Either or both effects could play a role in IC 4329A.

This work is also in agreement with the results of de La Calle Pérez et al. (2010), Guainazzi et al. (2006) and Nandra et al. (2007). Very high signal-to-noise ratio is required to disentangle broad iron line components even in the brightest nearby AGN. Despite IC 4329A is the second brightest Seyfert 1 galaxy (in the 2-10 keV energy band) it was necessary to combine all the data to model ratios and reach a total exposure time of $\sim$ 130 ks in order to clearly detect significant residuals at $\sim$ 6.4 keV.

Another aspect of this work is to examine the relationship between the Fe K$\alpha$ strength and the Compton hump. Being features of the the same reflection spectrum, they should both respond to the variation of the primary continuum. Fits performed with the phenomenological model (Gaussian model) have revealed no evident correlation between these features. On the other hand, the physically self-consistent reflection model (*pexmon*) provides a much better fit to the data. This suggests that such a correlation might in fact be present. As a further test, we allowed the iron abundance to vary in the Reflection model. While largely unphysical (one would not expect the iron abundance to vary on time scales of $\sim$ 20 days), the effect is to decouple the emission line from the reflection continuum, while retaining the requirement for both to be present. This naturally accounts for the evidence in the spectra for both a blurred and distant reflection component. Applying this approach, we find consistency in the iron abundance between all the observation, with evidence of a sub-solar values ($A_{Fe} \sim 0.5$). If this is the case, the sub-solar iron abundance could be another factor contributing to the difficulty in the detection of the relativistic component in this source. Furthermore, the consistency of the iron abundance between each observation shows that the data are in agreement with the hypothesis of the iron line tracking the reflection continuum, as expected in the standard model.

Finally, we also detected a narrow emission line at 6.94 keV with the 99.7% of confidence level in two observations, in agreement with previous findings of McKernan & Yaqoob (2004). This feature does not appear to be a blue wing of a disk line, but it is more likely to be associated with ionized gas and identified as a narrow Fe XXVI emission line.

## 3.4 Conclusion

We presented the analysis of the *Suzaku* spectra of the bright Seyfert 1 galaxy IC 4329A. The Fe K band is dominated by a narrow core at 6.4 keV produced by neutral and distant material. Using a physically self-consistent model, our analysis also reveals the presence of a broad Fe line, produced in the inner parts of the accretion disk and blurred by general relativistic effects. This line component is not evident in the single epoch observations, but it is clearly present, with high significance, in the combined data to model ratio. This result is the first clear demonstration of a relativistic Fe line component in this source.

The data are also consistent with both the narrow and broad Fe line components tracking the emission at higher energies, i.e. Compton hump. An additional narrow Fe XXVI emission line at 6.94 keV is also detected, suggesting the presence of ionized material relatively distant from the central source.

# Chapter 4

# Relativistic Reflection in a Sample of Seyfert 1 galaxies

## 4.1 Introduction

In the previous chapter, we presented the analysis of the bright Seyfert 1 galaxy, IC 4329A. The *Suzaku* data are consistent with the presence of a relativistic iron K$\alpha$ emission line, but it is clearly visible only when all the observations were combined together and the signal-to-noise increases. Moreover, a relationship between the flux of this feature and the emission of the Compton hump at higher energies is found.

Several studies investigated whether the relativistic Fe K$\alpha$ line is an ubiquitous feature in the X-ray spectra of the Seyfert 1 galaxies or not, using large samples of sources observed with *XMM-Newton* (Guainazzi et al. 2006, Nandra et al. 2007, de La Calle Pérez et al. 2010) and *Suzaku* (Patrick et al. 2012, Walton et al. 2013). A large fraction of the spectra analyzed did not show the presence of relativistic Fe line emission from the accretion disk. As presented in Section 1.6, the nature of this absence was poorly understood and several hypothesis have been proposed to explain these results. One of the main reasons might be the low signal-to-noise ratio of the single observations (Guainazzi et al. 2006, Nandra et al. 2007, de La Calle Pérez et al. 2010, Patrick et al. 2012). Another explanation is that the disk is truncated at larger radii. In this case the relativistic effects are no longer important. Lastly, Bhayani & Nandra (2011) have suggested that strong relativistic effects could also explain the lack of relativistic features, due to the difficulty of disentangling very broad emission lines from the underlying continuum.

In this chapter, we investigate this phenomenon by analyzing *Suzaku* observations of sources previously observed with *XMM-Newton*, where a relativistic Fe line was missing. The broad band spectrum of the *Suzaku* data and its high throughput around the Fe K$\alpha$ line allows an independent check of the *XMM-Newton* results and to investigate the Compton hump at high energies, for comparison with the emission line properties.

## 4.2 Sample Selection

Our sample was compiled starting from the work of Nandra et al. (2007). In this work a sample of sources was analysed using *XMM-Newton* observations. The aim was to characterize the iron K$\alpha$ emission line in a unique and systematic way in the bright and local AGN. The Nandra et al. (2007) sample was compiled from the *XMM-Newton* observations available in the archive cross-correlated with the Véron-Cetty & Véron (2001) AGN catalogue. A cut on the redshift was adopted in order to restrict the analysis to nearby objects ($z < 0.05$). Seyfert 2 galaxies were excluded from the study because their central engine is usually heavily obscured in X-ray. Nandra and collaborators also included lightly obscured, intermediate Seyfert classifications (i.e. Sy 1.8 and 1.9) and the objects which are classified as Seyfert 2 galaxies which however, show broad emission lines detected in the near IR. Radio loud sources and central cluster galaxies were excluded as well, even if they are classified as AGN. From the entire sample analysed in Nandra et al. (2007), we selected only the sources in which a relativistic Iron K$\alpha$ emission line was not detected. In the cases in which one source has multiple observations and at least one of those did not show a relativistic component, the object was still considered for our analysis. The objects selected for this analysis are presented in Table 4.1.

The goal of this analysis is to investigate why certain sources do not show relativistic emission. For example, we want to understand if the absence is related to the geometrical structure of the source itself (e.g. the accretion disk is truncated) or if it is related to the signal-to-noise of each single observation. This could be not sufficiently high in order to distinguish such a broad emission line from the underlying continuum. Since our goal is also to investigate the relation between both the narrow and relativistic iron lines and the emission at higher energies (i.e. Compton hump), we decided to use *Suzaku* observations. As we discussed in section 2.2, the extended energy band of *Suzaku* compared to *XMM-Newton* allows us to model the high energy part of the X-ray spectra. In particular, it is possible to estimate with more precision the reflection coming from the disk, measuring the reflection fraction R (see Section 1.4). Moreover, the primary X-ray continuum can be better constrained, and this is an important point for the analysis of relativistic iron lines.

We therefore searched for *Suzaku* archival observations of the sources missing a broad iron component in the work of Nandra et al. (2007). In Table 4.1, together with the source name, we report the continuum flux in the iron K band (i.e. in the 5-7 keV energy band), the observational ID and the total exposure time for each source. When multiple observations are available, the mean continuum flux is quoted. The flux in the iron K band is expressed in units of $10^{-11}$ erg cm$^{-2}$ s$^{-1}$, while the exposure time is in ks. From the sub-sample selected from Nandra et al. (2007), we excluded from the following analysis two sources, Mrk 6 and HE 1143-1810 because no *Suzaku* observations are available in archive. NGC 2110 is a special case. This source is a narrow-line object in the optical and is viewed through a relatively large absorption screen, which may be patchy (e.g., Evans et al. 2007), or ionized (Nandra et al. 2007). The analysis of different *XMM-Newton*, *Chandra* and *Suzaku* observations demonstrated the presence of a relatively stable, full-covering absorber (column density of $\sim 3 \times 10^{22}$ cm$^{-2}$). Together with this, an additional

Table 4.1: Sample of objects missing relativistic Fe K$\alpha$ line in their *XMM-Newton* observations (Nandra et al. 2007) and therefore considered in this work. The flux is in units of $10^{-11}$ erg cm$^{-2}$ s$^{-1}$. †Flux in the 2-10 keV band from Nandra et al. 2007.

| Object | Flux 5-7 keV | #Suzaku Obs | Exposure (ks) |
|---|---|---|---|
| NGC 2110 | 3.4 | 2 | 205.300 |
| NGC 5506 | 2.7 | 3 | 158.455 |
| IC 4329A | 2.6 | 6 | 248.820 |
| MCG +8-11-11 | 1.6 | 1 | 98.750 |
| NGC 7213 | 0.57 | 1 | 90.750 |
| MRK 110 | 0.48 | 1 | 90.900 |
| NGC 7469 | 0.49 | 1 | 112.100 |
| NGC 5548 | 0.46 | 7 | 209.435 |
| MRK 590 | 0.18 | 2 | 102.520 |
| HE 1143-1810 | 2.83† | 0 | - |
| MRK 6 | 1.43† | 0 | - |

absorber, likely variable in both column density and covering fraction, was required by the data (Rivers et al. 2014). The difficulties in modelling the absorber in this source could produce residuals in the iron energy band, which are difficult to distinguish from any relativistic Fe K$\alpha$ emission. As the latter is the main focus of this work, we decided to exclude this object from the following analysis.

For the data reduction of the spectra from the *Suzaku* XIS and PIN instruments, we followed the process described in Chapter 2. The XIS0 and XIS3 spectra were added together, as presented in Chapter 2. We considered only the PIN spectra where the source spectrum is more than 20% of the background. In Table 4.2 we present the PIN energy bands considered for this analysis.

## 4.3 Data Analysis

### 4.3.1 Baseline model

The general approach that we followed is to fit the spectra of all the sources systematically with the same models. The first attempt was to model the emission of the X-ray primary continuum, applying a model which includes a power law with an high energy cutoff, along with neutral reflection (Magdziarz & Zdziarski 1995) and a neutral absorber at the redshift of the source. In *xspec*, we adopted the following model: *zwabs*(pexrav)* (Baseline model). The neutral absorber was actually required only for two sources, IC 4329A and NGC 5506, with values for the column density of $N_H = 0.4 \times 10^{22}$ cm$^{-2}$ (Mantovani et al. 2014) and $N_H \sim 3 \times 10^{22}$ cm$^{-2}$ (Bianchi et al. 2003), respectively. We assumed solar abundances and an inclination of the reflector of 60°. The high energy cutoff of the primary continuum was usually assumed to be 300 keV. However, in the case of IC 4329A we adopted $E_c$

Table 4.2: PIN energy ranges used in the analysis.

| Object | Observation ID | PIN Energy Range |
|---|---|---|
| NGC 5506 | 701030010 | 12-60 keV |
| | 701030020 | 12-50 keV |
| | 701030030 | 12-50 keV |
| IC 4329A | 702113010 | 12-55 keV |
| | 702113020 | 12-50 keV |
| | 702113030 | 12-55 keV |
| | 702113040 | 12-70 keV |
| | 702113050 | 12-55 keV |
| | 707025010 | 12-55 keV |
| MCG +8-11-11 | 702112010 | 12-50 keV |
| NGC 7213 | 701029010 | Not Considered |
| MRK 110 | 702124010 | 12-25 keV |
| NGC 7469 | 703028010 | 12-30 keV |
| NGC 5548 | 702042010 | Not Considered |
| | 702042020 | Not Considered |
| | 702042040 | 12-25 keV |
| | 702042050 | 12-25 keV |
| | 702042060 | 12-35 keV |
| | 702042070 | 12-30 keV |
| | 702042080 | Not Considered |
| MRK 590 | 705043010 | Not Considered |
| | 705043020 | Not Considered |

= 180 keV, based on recent *NuSTAR* and *Suzaku* observations (Brenneman et al. 2014a, Mantovani et al. 2014). For NGC 5506 we fixed this parameter to $E_c$ = 130 keV, as Bianchi et al. (2003) reported from the analysis of *BeppoSAX* observations.

In Figure 4.1 the data to model ratios are presented for each source. The upper panels show the ratios when only the continuum is fitted with the Baseline model. In order to fit only the power law contribution to the emission in the spectra, the energy range between 5 and 7 keV was excluded in the fitting process. In the middle panels, we present the data to model ratios when a narrow gaussian model component is included in the Baseline model to fit the narrow iron K$\alpha$ emission (for further details we refer to section 4.3.2). The bottom panels show the data to model ratios when the Relativistic Relline model is applied to the data (see Section 4.3.3 for details). When more than one observation is available for one object, we combined all the data to model ratios after the model was applied to each spectrum independently. This is the case for NGC 5506, MRK 590, NGC 5548 and

IC 4329A. In the upper panels, clear residuals at 6.4 keV are present in each source which could be due to a blend of narrow and relativistic Fe K$\alpha$ emission lines. Moreover, ionized iron emission lines, such as Fe XXV and Fe XXVI, can be present in some sources. This could be the case in NGC 5506, IC 4329A and MCG +8-11-11. In the next section, we investigate the nature of the iron complex in all the objects of the sample.

### 4.3.2 Narrow Line Model

After modelling the primary X-ray continuum and the Compton reflection component, we tested whether or not the residuals at 6.4 keV (Fig. 4.1) could be associated with emission from distant material. Indeed, if the relativistic iron line is not present in the spectra, only a narrow Fe K$\alpha$ line will be necessary to completely model these residuals. In order to verify the presence of reflection from distant material (e.g. the torus) we added to the previous model, the so-called Baseline model, a narrow gaussian component (*zgauss* in *xspec*) to fit the residuals at $\sim$ 6.4 keV (Narrow Line Model: *zwabs*(pexrav+zgauss)*). We fixed the width of the gaussian component to $\sigma = 1$ eV, while the energy was free to vary.

As presented in Section 1.4, Fe K$\beta$ emission is expected to be produced in the reflection spectrum from neutral material together with the iron K$\alpha$ component. We therefore included in the previous model another Gaussian component in order to fit this feature. The energy of this line was fixed to 7.06 keV, the width to $\sigma = 1$ eV and the flux was linked to that of Fe K$\alpha$. We remind the reader that this is expected to be about 11.3 per cent of that of the 6.4 keV emission line (as presented in section 1.4).

After the inclusion of the narrow iron K$\beta$ line, we tested for the presence of ionized emission lines in all the spectra, specifically the H-like and He-like lines (Fe XXV and Fe XXVI). For this reason, we added to the previous model two narrow gaussian components. The energies of these lines were fixed to 6.7 keV and 6.96 keV, respectively (Bianchi & Matt 2002, Bianchi et al. 2004), which are the rest frame energies, and the widths to $\sigma = 1$ eV. In Table 4.3 we present the results of this test for each observation. Together with the fluxes of the line, we show the improvements in $\Delta\chi^2$ when those components are included in the model. We conservatively included these lines in the subsequent analysis whenever the 90% lower limit on the flux was found to be greater than zero. The presence of both Fe XXV and Fe XXVI lines in all the three spectra of NGC 5506 is consistent with previous results based on the analysis of *XMM-Newton* observations (Matt et al. 2001). In the case of IC 4329A, the Fe XXV emission line was already significantly detected in the previous work of Mantovani et al. (2014), when the same *Suzaku* observations were analyzed. The residuals from these fits are presented in the middle panels in Figure 4.1. It is clear that the narrow gaussian component account for the peak at 6.4 keV. However, important residuals are still present in some objects, such as NGC 5506, IC 4329A, MCG +8-11-11 and NGC 7469, which could be associated with a relativistic Fe K$\alpha$ line component. We investigate the nature of these residuals in Section 4.3.3.

Table 4.4 presents the parameters free to vary when the Narrow Line model is applied to the data. The Fe K$\alpha$ narrow component is always detected in all the observations with energies consistent with 6.4 keV indicating emission from neutral material. For this reason,

Table 4.3: Observations where the Fe xxv and the Fe xxvi lines were detected. We report the improvements in $\Delta\chi^2/\Delta$d.o.f. in the cases where the detection of the lines is significant. The fluxes are in units of $10^{-5}$ erg s$^{-1}$ cm$^{-2}$.

| Object | Observation | Flux xxv | Flux xxvi | $\Delta\chi^2/\Delta$d.o.f. |
|---|---|---|---|---|
| NGC 5506 | 701030010 | $2.68^{+0.73}_{-0.74}$ | $2.08^{+0.74}_{-0.74}$ | 55.5/2 |
| | 701030020 | $2.42^{+0.72}_{-0.72}$ | $1.63^{+0.72}_{-0.72}$ | 44.68/2 |
| | 701030030 | $1.36^{+0.64}_{-0.64}$ | $1.20^{+0.64}_{-0.64}$ | 20.62/2 |
| IC 4329A | 702113010 | - | $1.44^{+0.89}_{-0.89}$ | 7.89/1 |
| | 702113020 | - | $1.71^{+0.88}_{-0.88}$ | 10.12/1 |
| | 702113030 | - | - | - |
| | 702113040 | - | - | - |
| | 702113050 | - | $1.10^{+0.78}_{-0.78}$ | 5.37/1 |
| | 707025010 | - | $0.68^{+0.46}_{-0.46}$ | 6.06/1 |
| MCG +8-11-11 | 702112010 | - | $1.22^{+0.39}_{-0.39}$ | 26.3/1 |
| NGC 7213 | 701029010 | $0.69^{+0.26}_{-0.26}$ | $0.43^{+0.25}_{-0.25}$ | 22.05/2 |
| MRK 110 | 702124010 | - | $0.40^{+0.24}_{-0.24}$ | 7.72/1 |
| NGC 7469 | 703028010 | - | - | - |
| NGC 5548 | 702042010 | - | - | - |
| | 702042020 | - | - | - |
| | 702042040 | - | - | - |
| | 702042050 | - | - | - |
| | 702042060 | - | - | - |
| | 702042070 | - | - | - |
| | 702042080 | - | $0.31^{+0.30}_{-0.29}$ | 3.01/1 |
| MRK 590 | 705043010 | $0.29^{+0.18}_{-0.19}$ | - | 6/1 |
| | 705043020 | - | - | - |

we decided to fix the energy of the narrow gaussian component to 6.4 keV in the subsequent analysis. The equivalent widths of this feature are different within the sample, ranging from $\sim$ 40 eV to $\sim$ 200 eV. The slopes of the power law component, which is reproducing the primary X-ray continuum, are also different for each sources, but the measurements are consistent with values typically observed in the Seyfert galaxies (Piconcelli et al. 2005, Bianchi et al. 2009).

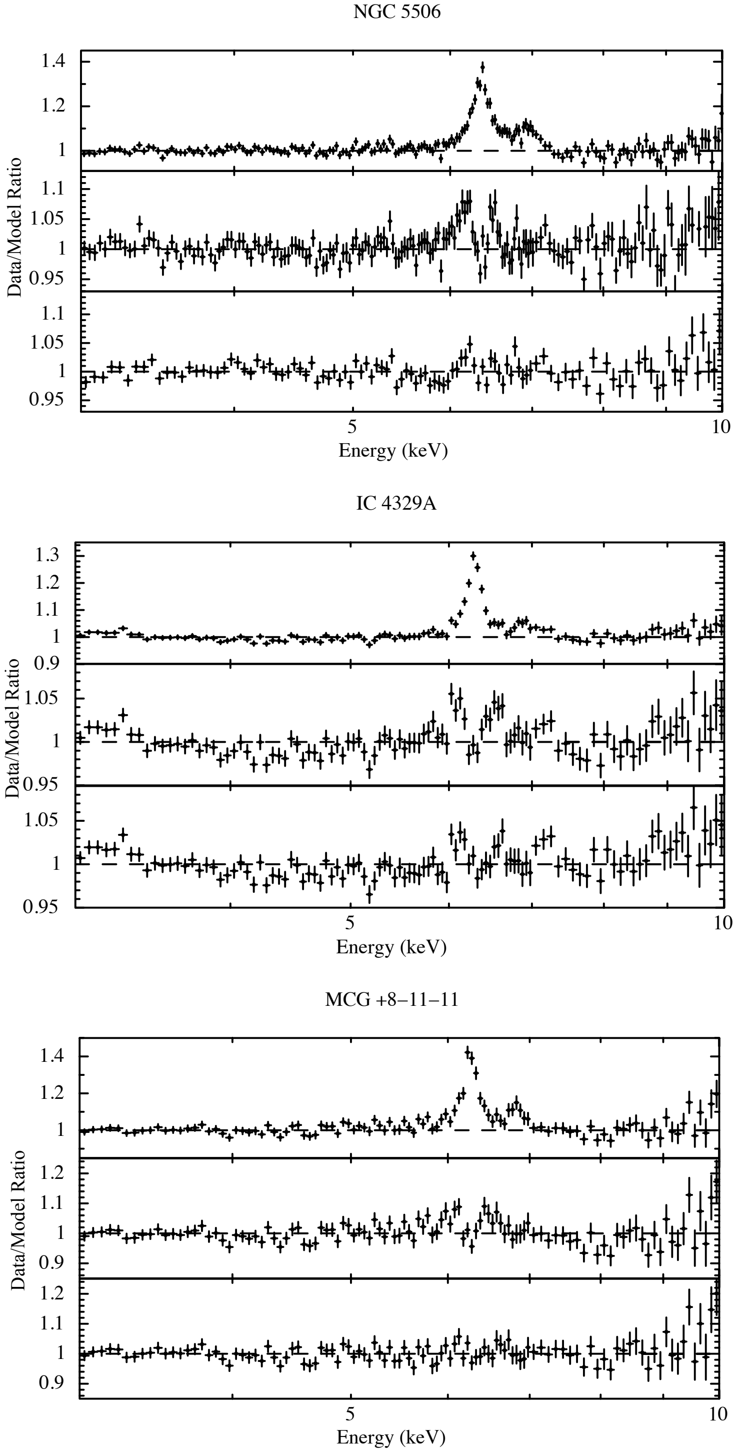

Figure 4.1: We present the XIS data to model ratios for each source in the sample. The top panels show a model that includes a neutral absorber at the redshift of the source and a reflection component (as described in Section 4.3.1). The 5-7 keV data have been excluded from these fits. The middle panels show the residuals from a model adding a gaussian component to fit the narrow Fe K$\alpha$ emission line (see Section 4.3.2). The bottom panels show the data to model ratio when a relativistic line line component is included in the previous model (Relativistic Relline Model, see Section 4.3.3).

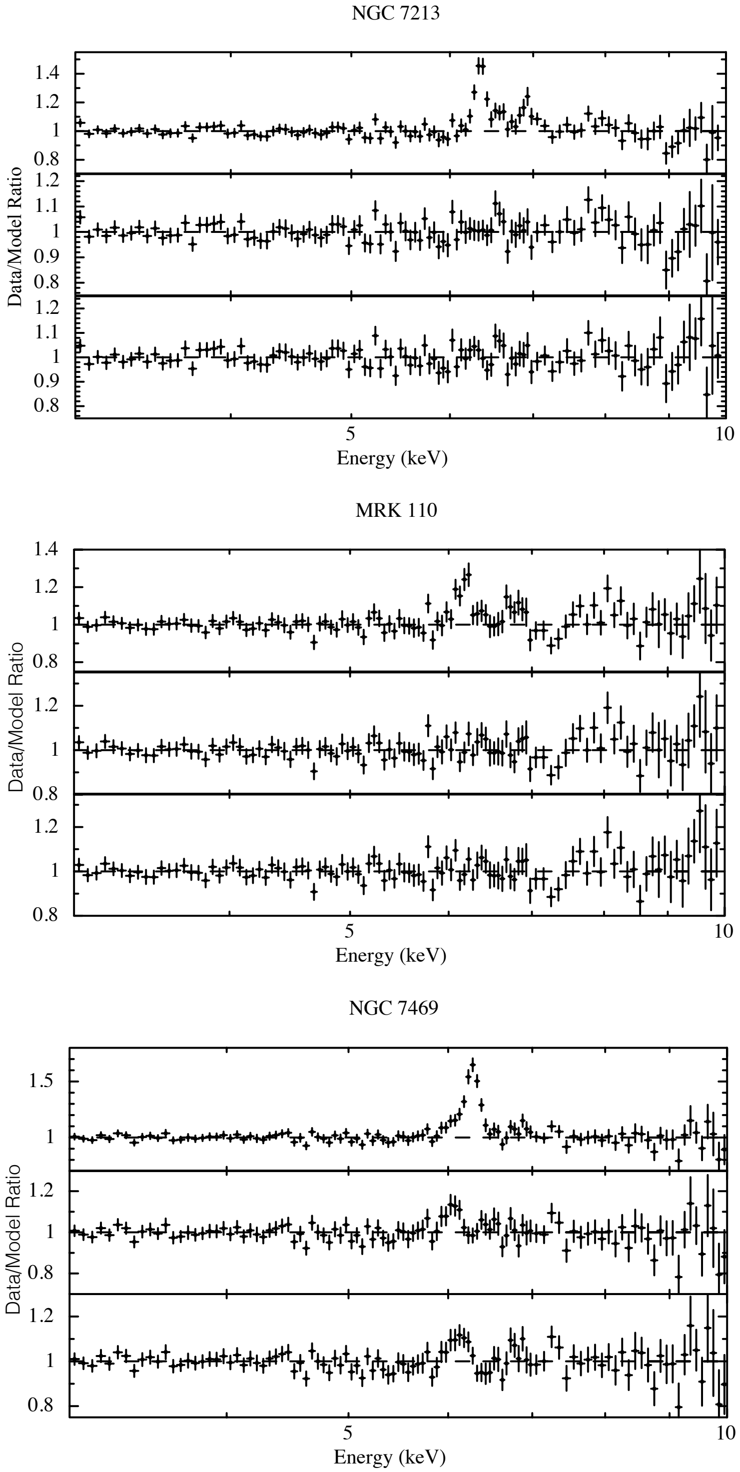

Figure 4.1: (Continued)

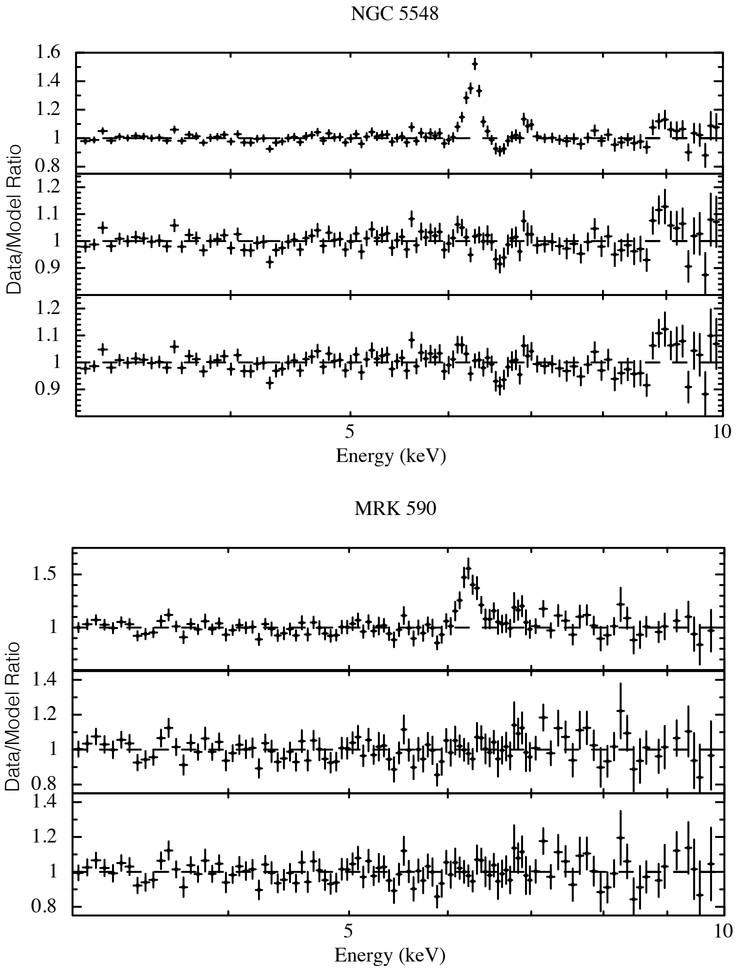

Figure 4.1: (Continued)

Table 4.4: Best-fit parameters for the Narrow Line Model. The column density is in units of $10^{22}$ cm$^{-2}$ and the normalization of the primary continuum is in units of $10^{-2}$ photons keV$^{-1}$ cm $^{-2}$ s$^{-1}$. The energy of the Iron line is shown in keV, while the EW is in eV. The FeK$\alpha$ flux is quoted in units of $10^{-5}$ erg s$^{-1}$ cm$^{-2}$. The continuum flux in the 3-10 keV band is in units of $10^{-11}$ erg s$^{-1}$ cm$^{-2}$. In the last column we present the best fit $\chi^2$/d.o.f. when the energy of the iron line is fixed to 6.4 keV.

| Object | Observation | $N_H$ | $\Gamma$ | R | Norm | $E_{K\alpha}$ | $Flux_{K\alpha}$ | EW | $Flux_{3-10keV}$ | $\chi^2$/d.o.f | $\chi^2$/d.o.f$_{K\alpha}$ |
|---|---|---|---|---|---|---|---|---|---|---|---|
| NGC 5506 | 701030010 | $2.76^{+0.22}_{-0.22}$ | $1.92^{+0.05}_{-0.04}$ | $1.23^{+0.27}_{-0.24}$ | $4.12^{+0.29}_{-0.27}$ | $6.41^{+0.01}_{-0.01}$ | $9.50^{+0.78}_{-0.77}$ | $72^{+8}_{-8}$ | $8.59^{+0.01}_{-0.01}$ | 1362.29/1334 | 1363.73/1335 |
|  | 701030020 | $3.09^{+0.20}_{-0.20}$ | $1.95^{+0.04}_{-0.04}$ | $1.33^{+0.26}_{-0.23}$ | $4.63^{+0.30}_{-0.28}$ | $6.39^{+0.02}_{-0.01}$ | $9.09^{+0.77}_{-0.77}$ | $64^{+5}_{-5}$ | $9.12^{+0.03}_{-0.03}$ | 1463.26/1403 | 1463.89/1404 |
|  | 701030030 | $3.21^{+0.19}_{-0.19}$ | $2.02^{+0.05}_{-0.04}$ | $1.83^{+0.35}_{-0.30}$ | $4.79^{+0.32}_{-0.30}$ | $6.39^{+0.01}_{-0.01}$ | $7.73^{+0.68}_{-0.69}$ | $58^{+5}_{-5}$ | $8.55^{+0.02}_{-0.02}$ | 1411.65/1377 | 1415.12/1378 |
| IC 4329A | 702113010 | 0.4 fixed | $1.82^{+0.04}_{-0.03}$ | $0.79^{+0.24}_{-0.21}$ | $3.13^{+0.15}_{-0.13}$ | $6.39^{+0.02}_{-0.02}$ | $6.26^{+0.96}_{-0.92}$ | $53^{+8}_{-8}$ | $8.38^{+0.01}_{-0.01}$ | 938.11/876 | 939.04/877 |
|  | 702113020 | 0.4 fixed | $1.92^{+0.04}_{-0.03}$ | $1.50^{+0.30}_{-0.26}$ | $4.23^{+0.18}_{-0.17}$ | $6.39^{+0.01}_{-0.01}$ | $5.66^{+0.92}_{-0.92}$ | $40^{+7}_{-7}$ | $9.85^{+0.01}_{-0.01}$ | 1091.85/1093 | 1092.91/1094 |
|  | 702113030 | 0.4 fixed | $1.77^{+0.03}_{-0.03}$ | $0.81^{+0.21}_{-0.19}$ | $3.27^{+0.14}_{-0.13}$ | $6.38^{+0.01}_{-0.02}$ | $7.32^{+0.99}_{-0.99}$ | $54^{+7}_{-7}$ | $9.48^{+0.01}_{-0.01}$ | 985.37/989 | 993.81/990 |
|  | 702113040 | 0.4 fixed | $1.82^{+0.04}_{-0.04}$ | $0.97^{+0.27}_{-0.23}$ | $3.19^{+0.15}_{-0.14}$ | $6.40^{+0.02}_{-0.02}$ | $7.58^{+1.00}_{-0.99}$ | $62^{+8}_{-8}$ | $8.62^{+0.01}_{-0.01}$ | 917.53/861 | 917.72/862 |
|  | 702113050 | 0.4 fixed | $1.73^{+0.06}_{-0.05}$ | $1.51^{+0.52}_{-0.39}$ | $1.73^{+0.13}_{-0.11}$ | $6.40^{+0.02}_{-0.02}$ | $5.65^{+0.84}_{-0.82}$ | $69^{+10}_{-10}$ | $5.65^{+0.02}_{-0.02}$ | 589.74/586 | 589.83/587 |
|  | 707025010 | 0.4 fixed | $1.74^{+0.01}_{-0.01}$ | $0.48^{+0.08}_{-0.07}$ | $2.88^{+0.05}_{-0.05}$ | $6.40^{+0.01}_{-0.01}$ | $7.88^{+0.48}_{-0.48}$ | $65^{+4}_{-4}$ | $8.65^{+0.01}_{-0.01}$ | 1688.70/1639 | 1689.37/1640 |
| MCG +8-11-11 | 702112010 | - | $1.65^{+0.02}_{-0.01}$ | <0.12 | $1.49^{+0.04}_{-0.03}$ | $6.39^{+0.01}_{-0.01}$ | $5.61^{+0.42}_{-0.42}$ | $78^{+6}_{-6}$ | $5.19^{+0.01}_{-0.01}$ | 1296.96/1324 | 1298.25/1325 |
| NGC 7213 | 701029010 | - | $1.75^{+0.07}_{-0.07}$ | < 1.21 | $0.62^{+0.05}_{-0.04}$ | $6.39^{+0.01}_{-0.01}$ | $2.08^{+0.28}_{-0.25}$ | $81^{+11}_{-11}$ | $1.89^{+0.01}_{-0.01}$ | 677.09/689 | 680.17/690 |
| MRK 110 | 702124010 | - | $1.74^{+0.04}_{-0.04}$ | < 0.41 | $0.55^{+0.03}_{-0.03}$ | $6.39^{+0.03}_{-0.03}$ | $1.06^{+0.25}_{-0.24}$ | $44^{+10}_{-10}$ | $1.65^{+0.01}_{-0.01}$ | 546.96/546 | 547.12/547 |
| NGC 7469 | 703028010 | - | $1.75^{+0.05}_{-0.05}$ | $0.94^{+0.40}_{-0.32}$ | $0.52^{+0.03}_{-0.03}$ | $6.38^{+0.01}_{-0.01}$ | $2.73^{+0.24}_{-0.24}$ | $119^{+10}_{-11}$ | $1.64^{+0.01}_{-0.01}$ | 633.72/667 | 650.95/668 |
| NGC 5548 | 702042010 | - | $1.45^{+0.22}_{-0.11}$ | <3.58 | $0.12^{+0.03}_{-0.02}$ | $6.40^{+0.02}_{-0.02}$ | $1.85^{+0.33}_{-0.33}$ | $192^{+34}_{-34}$ | $0.68^{+0.01}_{-0.01}$ | 83.72/101 | 83.87/102 |
|  | 702042020 | - | $1.68^{+0.14}_{-0.13}$ | <2.78 | $0.30^{+0.05}_{-0.04}$ | $6.39^{+0.02}_{0.02}$ | $2.03^{+0.35}_{-0.34}$ | $132^{+23}_{-23}$ | $1.10^{+0.01}_{-0.01}$ | 235.1/188 | 236.91/189 |
|  | 702042040 | - | $1.69^{+0.07}_{-0.06}$ | <0.71 | $0.61^{+0.05}_{-0.05}$ | $6.37^{+0.03}_{-0.03}$ | $1.82^{+0.43}_{-0.43}$ | $64^{+15}_{-15}$ | $2.04^{+0.02}_{-0.02}$ | 326.84/312 | 328.70/313 |
|  | 702042050 | - | $1.55^{+0.09}_{-0.08}$ | $0.79^{+0.68}_{-0.49}$ | $0.33^{+0.04}_{-0.03}$ | $6.38^{+0.02}_{-0.02}$ | $1.90^{+0.39}_{-0.39}$ | $92^{+19}_{-19}$ | $1.45^{+0.01}_{-0.01}$ | 220.66/230 | 222.41/231 |
|  | 702042060 | - | $1.61^{+0.05}_{-0.05}$ | <0.49 | $0.70^{+0.05}_{-0.04}$ | $6.41^{+0.03}_{-0.03}$ | $1.80^{+0.49}_{-0.49}$ | $49^{+13}_{-13}$ | $2.77^{+0.03}_{-0.03}$ | 388.77/374 | 389.54/375 |
|  | 702042070 | - | $1.58^{+0.07}_{-0.06}$ | $0.42^{+0.42}_{-0.32}$ | $0.45^{+0.04}_{-0.03}$ | $6.39^{+0.02}_{-0.02}$ | $2.28^{+0.42}_{-0.42}$ | $90^{+17}_{-17}$ | $1.80^{+0.01}_{-0.01}$ | 252.40/295 | 253.00/296 |
|  | 702042080 | - | $1.63^{+0.16}_{-0.15}$ | <3.38 | $0.24^{+0.04}_{-0.04}$ | $6.41^{+0.01}_{-0.02}$ | $2.16^{+0.36}_{-0.32}$ | $158^{+26}_{-26}$ | $0.98^{+0.01}_{-0.01}$ | 170.68/180 | 172.86/181 |
| MRK 590 | 705043010 | - | $1.65^{+0.14}_{-0.05}$ | <1.39 | $0.17^{+0.03}_{-0.01}$ | $6.40^{+0.02}_{-0.02}$ | $1.06^{+0.20}_{-0.21}$ | $118^{+24}_{-25}$ | $0.62^{+0.01}_{-0.01}$ | 199.99/186 | 200.44/187 |
|  | 705043020 | - | $1.56^{+0.20}_{-0.11}$ | <2.74 | $0.13^{+0.03}_{-0.02}$ | $6.41^{+0.03}_{-0.03}$ | $0.86^{+0.25}_{-0.25}$ | $106^{+31}_{-31}$ | $0.57^{+0.01}_{-0.01}$ | 103.76/116 | 104.35/117 |

### 4.3.3 Relativistic Fe K$\alpha$ analysis

One of the main aims of this thesis is to investigate the presence of relativistic iron K$\alpha$ emission in the spectra of Seyfert 1 galaxies. For this reason after modelling all the narrow Fe features present in the *Suzaku* spectra, we tested if the quality of the fits improves adding a relativistic iron K$\alpha$ line component. Ideally, one would compare the $\chi^2$ obtained from the fit with and without a broad line component and estimate its significance. However, assessing the significance of relativistic emission lines in the X-ray spectra of AGN is not straightforward. For example, it has been pointed out that the F-test is not a precise tool to estimate the chance probability of detecting these or similar features (Protassov et al. 2002).

#### Estimating the significance of relativistic Fe line detections for a given $\Delta\chi^2$

In order to estimate the appropriate significance of the line, we performed Monte Carlo simulations. We started by simulating six thousand spectra. The model used in this process includes a cut-off power law, a reflection component with narrow Fe K$\alpha$, Fe K$\beta$ and Ni K$\alpha$ emission lines and an iron Compton shoulder: *cutoffpl+pexmon*. The *pexmon* model component (Nandra et al. 2007) reproduces self-consistently all the features of the reflection spectrum emitted from a neutral distant material: i) the Fe K$\alpha$ line, ii) the Fe K$\beta$ line, iii) the Ni K$\alpha$ line, iv) the Fe Compton shoulder. We used the *fakeit* command with the addition of the appropriate noise. We took into account the response files of the XIS instrument (i.e. XIS_FI.rmf and XRT_FI_xisnom.arf files). Once the spectra were simulated, we first refitted them with the simple *cutoffpl+pexmon* model and then we included also a *relline* component (Dauser et al. 2010). The latter is reproducing a relativistic Fe line profile modified by gravity effects close to the black hole assuming the lamp post geometry, in which the X-ray emitting source is placed above the black hole and irradiates the accretion disk. For each simulated spectrum, we recorded the best fit $\chi^2$ for the two different models. By recording how many times a $\Delta\chi^2$ better than the observed values happens by chance, we can establish a relation between the observed $\Delta\chi^2$ and the significance of the detection of the *relline* component in the real data.

We repeated this process using different relativistic line profiles in order to test if the threshold values of $\Delta\chi^2$ depends on the parameters adopted in the *relline* model component. Since it is difficult to constrain the most important parameters of the relativistic line, especially in the cases where the line is weak and/or very broad, we assumed emission from neutral material fixing the rest energy of the line to 6.4 keV. We also fixed the following parameters, except for the flux of the line: i) $E_{Relline} = 6.4$ keV; ii) index1 = index2 = 3; iii) $R_{break} = 15$ $r_g$; iv) a = 0; v) $R_{out} = 400$ $r_g$; vi) limb = 0 (see Section 1.5.1 for more details on the parameters). Since the sources of the sample are nearby objects, for the simulations we assumed $z = 0$. This allows us to obtain simulations that are useful for sources at low redshift. We modified the line profile using different combinations of inclinations (30°, 60°, 80°) and inner radii (6 $r_g$ and 1.24 $r_g$). When the inner radius was fixed to 1.24 $r_g$, the spin parameter was changed to a = 0.998, corresponding to a maximally spinning Kerr black hole. Table 4.5 presents the results of the simulations. The $\Delta\chi^2$ values reported correspond to the 95% confidence level for each combination.

Table 4.5: Results of the simulations for $\Delta\chi^2$ corresponding to the 95% confidence level for the detection of a relativistic Fe K$\alpha$ line. The spectra were simulated using a model including a cut-off power law and a reflection component with narrow Fe K$\alpha$, Fe K$\beta$ and Ni K$\alpha$ lines. We then refitted the spectra including a *relline* component in the model. The values are presented for different combinations of inclinations and inner radii.

| $\theta$ | $R_{in}$ | $\Delta\chi^2$(95%) |
|---|---|---|
| 30° | 6 $r_g$ | 4.71 |
| 30° | 1.24 $r_g$ | 5.57 |
| 60° | 6 $r_g$ | 2.67 |
| 60° | 1.24 $r_g$ | 2.99 |
| 80° | 6 $r_g$ | 1.99 |
| 80° | 1.24 $r_g$ | 1.44 |

### Spectral Analysis

Once we obtained the critical values for $\Delta\chi^2$ corresponding to the 95% confidence level, we then fitted all the actual source spectra using the Relativistic Relline model (RR): *zwabs*(pexrav+zgauss+relline)*. For the *relline* component we assumed the same parameters as for the simulations, and the same combinations of inner radius and inclination. The fixed combinations of inclination and inner radius are necessary because it is very difficult to constrain all parameters of the relativistic Fe K$\alpha$ line simultaneously, bearing in mind that the spectra in our sample have been chosen specifically because the relativistic component is weak and/or of low significance. The Relativistic Relline model includes a neutral absorber at the redshift of the source (*zwabs*), a cutoff power law together with a reflection continuum (*pexrav*), a narrow emission line (*zgauss*) and a relativistic line component (*relline*). The width of the gaussian model was fixed to $\sigma = 1$ eV, while the energy to 6.4 keV. We also included narrow Fe K$\beta$, Fe XXV and Fe XXVI emission lines, the latter when significantly detected in the previous analysis (see Table 4.3). For each source, we fitted all the combinations of inclinations and inner radii. Then we selected the best fit solution that leads to a detection of the relativistic iron K$\alpha$ line and improves the $\chi^2$ at more than 95% (see Table 4.5 for the $\Delta\chi^2$ values adopted). If more than one solution satisfies this criterion, we choose the one with the highest $\Delta\chi^2$. In the cases where the line is not detected, we have chosen the combination which leads to the best fit with the highest $\Delta\chi^2$ in order to calculate the upper limits for the relativistic iron line fluxes.

The best fit parameters for the Relativistic Relline model are presented in Table 4.6. All the errors correspond to $1\sigma$ confidence level, whereas upper limits correspond to the 95% confidence level as determined from the simulations. The relativistic iron K$\alpha$ emission line

Table 4.6: Best-fit parameters for the Relativistic Relline model. The column density is in units of $10^{22}$ cm$^{-2}$ and the normalization of the primary continuum is in units of $10^{-2}$ photons keV$^{-1}$ cm $^{-2}$ s$^{-1}$. The energies of the Fe K$\alpha$ and the Fe K$\beta$ lines are in keV while the EW in eV. The Fe K$\alpha$ ad Fe K$\beta$ fluxes are in units of $10^{-5}$ erg s$^{-1}$ cm$^{-2}$. The continuum flux in the 3-10 keV band is in units of $10^{-11}$ erg s$^{-1}$ cm$^{-2}$.

| Object | Observation | $N_H$ | $\Gamma$ | R | Norm | $\mathrm{Flux}_{K\alpha}$ | EW | $\mathrm{Flux}_{3-10keV}$ | $\theta_{disk}$ | $R_{in}$ | $EW_{Rell}$ | $\chi^2$/d.o.f | $\Delta\chi^2/\Delta$d.o.f. | Significance |
|---|---|---|---|---|---|---|---|---|---|---|---|---|---|---|
| NGC 5506 | 701030010 | $2.35^{+0.17}_{-0.17}$ | $1.87^{+0.03}_{-0.03}$ | $1.00^{+0.15}_{-0.14}$ | $3.71^{+0.18}_{-0.17}$ | $8.26^{+0.57}_{-0.57}$ | $61^{+4}_{-4}$ | $8.60^{+0.02}_{-0.02}$ | 30° | $6r_g$ | $62^{+16}_{-16}$ | 1348.65/1334 | 15.08/1 | 99.998% |
| | 701030020 | $2.50^{+0.15}_{-0.15}$ | $1.87^{+0.03}_{-0.03}$ | $0.99^{+0.13}_{-0.12}$ | $3.97^{+0.18}_{-0.17}$ | $7.16^{+0.55}_{-0.55}$ | $49^{+4}_{-4}$ | $9.13^{+0.02}_{-0.02}$ | 30° | $6r_g$ | $96^{+15}_{-15}$ | 1423.86/1403 | 40.03/1 | > 99.999 % |
| | 701030030 | $2.64^{+0.15}_{-0.15}$ | $1.93^{+0.03}_{-0.03}$ | $1.35^{+0.17}_{-0.16}$ | $4.09^{+0.19}_{-0.18}$ | $6.34^{+0.48}_{-0.47}$ | $46^{+3}_{-3}$ | $8.54^{+0.02}_{-0.02}$ | 30° | $6r_g$ | $89^{+15}_{-15}$ | 1381.03/1377 | 34.09/1 | > 99.99 % |
| IC 4329A | 702113010 | 0.4 fixed | $1.83^{+0.02}_{-0.02}$ | $0.84^{+0.15}_{-0.13}$ | $3.16^{+0.09}_{-0.08}$ | $5.07^{+0.65}_{-0.65}$ | $41^{+5}_{-5}$ | $8.37^{+0.01}_{-0.01}$ | 30° | $6r_g$ | $69^{+18}_{-18}$ | 923.58/876 | 15.46/1 | 99.986 % |
| | 702113020 | 0.4 fixed | $1.92^{+0.02}_{-0.01}$ | $1.50^{+0.17}_{-0.16}$ | $4.23^{+0.09}_{-0.09}$ | $5.63^{+0.55}_{-0.56}$ | $40^{+4}_{-4}$ | $9.85^{+0.02}_{-0.02}$ | 30° | $6r_g$ | <24 | 1092.91/1093 | - | - |
| | 702113030 | 0.4 fixed | $1.78^{+0.02}_{-0.02}$ | $0.83^{+0.13}_{-0.12}$ | $3.29^{+0.08}_{-0.08}$ | $6.49^{+0.67}_{-0.67}$ | $47^{+5}_{-5}$ | $9.48^{+0.01}_{-0.01}$ | 30° | $6r_g$ | < 66 | 990.03/989 | - | - |
| | 702113040 | 0.4 fixed | $1.83^{+0.02}_{-0.02}$ | $1.01^{+0.16}_{-0.14}$ | $3.21^{+0.09}_{-0.09}$ | $6.62^{+0.68}_{-0.68}$ | $53^{+5}_{-5}$ | $8.61^{+0.01}_{-0.01}$ | 30° | $6r_g$ | $54^{+18}_{-18}$ | 908.35/861 | 9.37/1 | 99.704 % |
| | 702113050 | 0.4 fixed | $1.74^{+0.03}_{-0.03}$ | $1.52^{+0.28}_{-0.24}$ | $1.73^{+0.07}_{-0.07}$ | $5.08^{+0.57}_{-0.57}$ | $61^{+7}_{-7}$ | $5.65^{+0.01}_{-0.01}$ | 30° | $6r_g$ | < 90 | 585.23/586 | - | - |
| | 707025010 | 0.4 fixed | $1.75^{+0.09}_{-0.09}$ | $0.53^{+0.05}_{-0.05}$ | $2.91^{+0.03}_{-0.03}$ | $6.80^{+0.35}_{-0.35}$ | $54^{+3}_{-3}$ | $8.64^{+0.02}_{-0.02}$ | 30° | $6r_g$ | $49^{+8}_{-8}$ | 1656.27/1639 | 33.1/1 | > 99.999 % |
| MCG +8-11-11 | 702112010 | - | $1.68^{+0.01}_{-0.01}$ | $0.12^{+0.06}_{-0.05}$ | $1.52^{+0.03}_{-0.02}$ | $4.59^{+0.29}_{-0.29}$ | $60^{+4}_{-4}$ | $5.17^{+0.01}_{-0.01}$ | 30° | $6r_g$ | $96^{+12}_{-12}$ | 1236.05/1324 | 62.2/1 | > 99.999 % |
| NGC 7213 | 701029010 | - | $1.85^{+0.06}_{-0.06}$ | $0.82^{+0.60}_{-0.55}$ | $0.70^{+0.05}_{-0.04}$ | $1.98^{+0.17}_{-0.17}$ | $77^{+6}_{-6}$ | $1.89^{+0.01}_{-0.01}$ | 80° | $6r_g$ | $233^{+80}_{-80}$ | 671.73/689 | 8.44/1 | > 99.999 % |
| MRK 110 | 702124010 | - | $1.79^{+0.05}_{-0.04}$ | $0.32^{+0.26}_{-0.22}$ | $0.58^{+0.03}_{-0.03}$ | $1.05^{+0.15}_{-0.15}$ | $44^{+6}_{-66}$ | $1.65^{+0.01}_{-0.01}$ | 80° | $1.24r_g$ | $148^{+122}_{-122}$ | 545.66/546 | 1.46/1 | 95.110% |
| NGC 7469 | 703028010 | - | $1.76^{+0.03}_{-0.03}$ | $0.96^{+0.22}_{-0.20}$ | $0.53^{+0.02}_{-0.02}$ | $2.39^{+0.16}_{-0.16}$ | $100^{+7}_{-7}$ | $1.64^{+0.01}_{-0.01}$ | 30° | $6r_g$ | $73^{+20}_{-20}$ | 637.81/667 | 13.14/1 | 99.977 % |
| NGC 5548 | 702042010 | - | $1.55^{+0.17}_{-0.16}$ | $1.56^{+1.70}_{-1.34}$ | $0.14^{+0.03}_{-0.02}$ | $1.84^{+0.20}_{-0.20}$ | $190^{+21}_{-21}$ | $0.68^{+0.01}_{-0.01}$ | 80° | $1.24r_g$ | <680 | 83.01/101 | - | - |
| | 702042020 | - | $1.82^{+0.12}_{-0.12}$ | $1.79^{+1.20}_{-1.00}$ | $0.35^{+0.05}_{-0.04}$ | $2.00^{+0.21}_{-0.21}$ | $130^{+14}_{-14}$ | $1.09^{+0.01}_{-0.01}$ | 80° | $1.24r_g$ | $489^{+247}_{-249}$ | 233.10/188 | 3.81/1 | 99.350 % |
| | 702042040 | - | $1.69^{+0.05}_{-0.03}$ | $0.26^{+0.28}_{-0.24}$ | $0.61^{0.04}_{-0.03}$ | $1.79^{+0.26}_{-0.26}$ | $63^{+9}_{-9}$ | $2.04^{+0.01}_{-0.01}$ | 80° | $1.24r_g$ | <131 | 328.70/312 | - | - |
| | 702042050 | - | $1.58^{+0.10}_{-0.07}$ | $0.96^{+0.66}_{-0.43}$ | $0.34^{+0.04}_{-0.03}$ | $1.86^{+0.24}_{-0.24}$ | $90^{+12}_{-12}$ | $1.45^{+0.01}_{-0.01}$ | 80° | $1.24r_g$ | <317 | 222.19/230 | - | - |
| | 702042060 | - | $1.61^{+0.02}_{-0.04}$ | $0.20^{+0.17}_{-0.13}$ | $0.70^{+0.02}_{-0.03}$ | $1.77^{+0.30}_{-0.30}$ | $48^{+8}_{-8}$ | $2.65^{+0.01}_{-0.01}$ | 80° | $1.24r_g$ | <43 | 389.54/374 | - | - |
| | 702042070 | - | $1.58^{+0.04}_{-0.04}$ | $0.42^{+0.24}_{-0.24}$ | $0.45^{+0.02}_{-0.02}$ | $2.27^{+0.25}_{-0.25}$ | $90^{+10}_{-10}$ | $1.80^{0.01}_{-0.01}$ | 80° | $1.24r_g$ | <105 | 253.00/295 | - | |
| | 702042080 | - | $1.63^{+0.10}_{-0.10}$ | $1.43^{+0.60}_{-0.60}$ | $0.24^{+0.02}_{-0.03}$ | $2.15^{+0.19}_{-0.19}$ | $156^{+14}_{-14}$ | $0.98^{+0.02}_{-0.02}$ | 80° | $1.24r_g$ | <113 | 172.86/180 | - | - |
| MRK 590 | 705043010 | - | $1.68^{+0.12}_{-0.05}$ | < 1.04 | $0.18^{+0.03}_{-0.01}$ | $1.06^{+0.12}_{-0.13}$ | $118^{+13}_{-15}$ | $0.61^{0.03}_{-0.03}$ | 80° | $1.24r_g$ | < 494 | 198.71/186 | - | - |
| | 705043020 | - | $1.70^{+0.17}_{-0.15}$ | <2.70 | $0.17^{+0.03}_{-0.02}$ | $0.83^{+0.15}_{-0.15}$ | $102^{+19}_{-19}$ | $0.57^{+0.02}_{-0.02}$ | 80° | $1.24r_g$ | $465^{+324}_{-329}$ | 102.35/116 | 2/1 | 96.750% |

is detected at least in one observation of each source, in a total of 12 out of 22 observations. In cases where the significance exceeds 95% confidence, we determine the significance more precisely using the distributions of $\Delta\chi^2$ from the simulations described above. We report these values in the last column of Table 4.6. We also present the improvements in $\Delta\chi^2$/d.o.f. when the *relline* model is included in the Narrow Line model. The typical value for the equivalent width of this component over the sample is $\sim$ 100 eV.

The bottom panels of Figure 4.1 show the data to model ratio of each source for the XIS spectra when the Relativistic Relline model is applied to the spectra. The broad residuals around 6.4 keV present in several cases in the middle panels (Narrow Line model) are generally well fitted by the *relline* model component. However, in the case of NGC 7469 residuals around the Fe K$\alpha$ line energy are still present, even if the relativistic Fe line is included and detected at more than 95% confidence). This could be due to the fact that we fixed many of the important parameters in the fits. We tested this hypothesis by letting the inner radius, the inclination and the emissivity index free to vary in the *relline* model component for this object. In this case, we found a better fit to the data with a $\chi^2/d.o.f.$ = 601.13/665, compared to that with frozen parameters ($\chi^2/d.o.f.$ = 637.81/667). The best fit parameters for inclination, inner radius and emissivity index are: $\theta = 17^{+2}_{-3}$, $r_{in} <$ 74 $r_g$ and $q = 1.69^{+0.48}_{-0.69}$. The equivalent width of the relativistic Fe line is $EW = 81^{+27}_{-24}$ eV. The results on this object are in agreement within the errors with previous analysis of the same spectrum performed by Patrick et al. (2012). We present in Figure 4.2 the data to model ratios for NGC 7469 when the Baseline model (upper panel), the Narrow Line model (middle panel) and the Relativistic Relline model (bottom panel) are applied to the data. It is evident that, when the inclination, inner radius and emissivity index are free to vary in the fit, the Relativistic Relline model is fitting all the residuals associated with the broad Fe K$\alpha$ component.

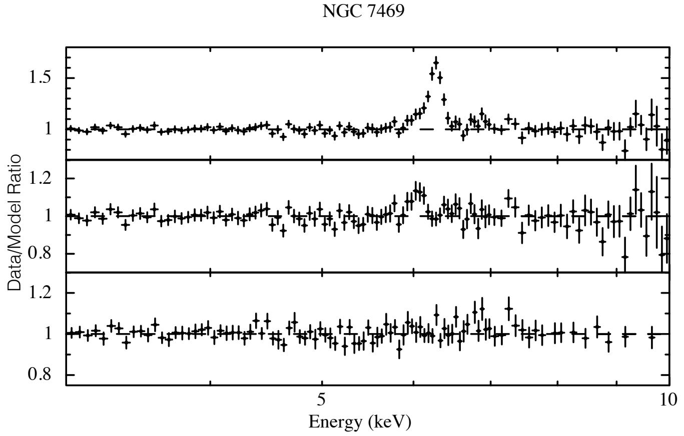

Figure 4.2: We present the data to model ratio of the XIS spectrum for NGC 7469. The Baseline model (upper panel), the Narrow Line model (middle panel) and the Relativistic Relline model (bottom panel) are applied to the data. In the Relativistic Relline model the inclination, the inner radius and the emissivity index are now free to vary in the fit

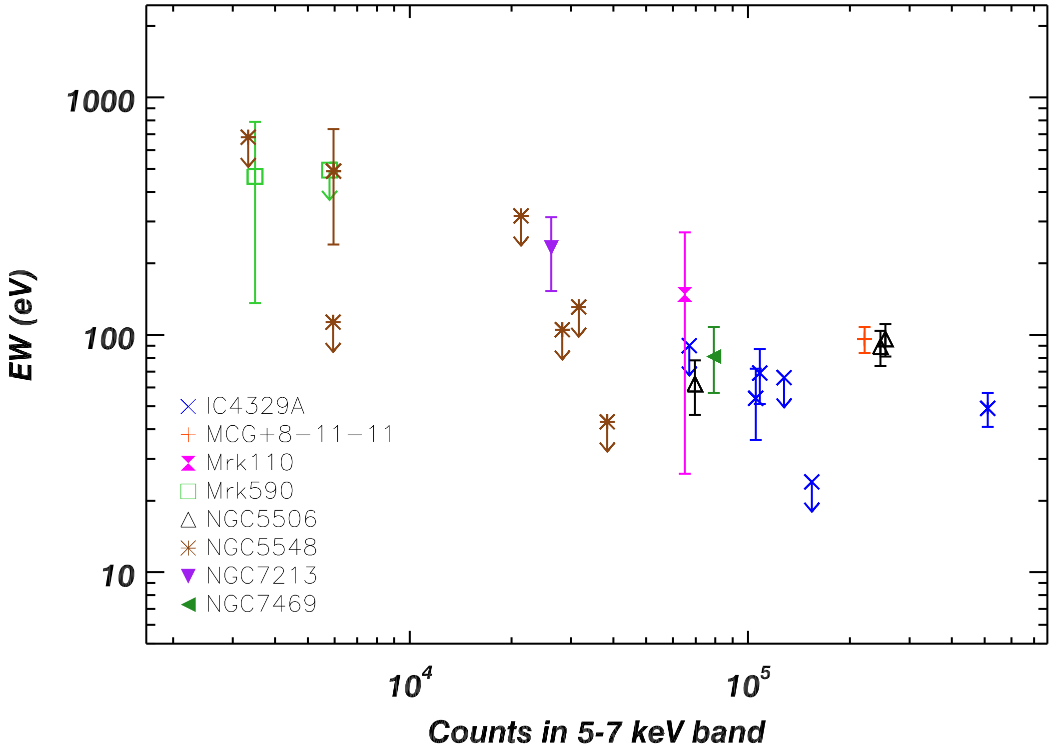

Figure 4.3: Equivalent Width (eV) of the relativistic Fe K$\alpha$ line component as a function of the counts in the Iron energy band. These counts are calculated for each observation as the product of the counts/s in the 5-7 keV energy band and the exposure time.

Figure 4.3 summarises the results of this analysis. The equivalent width of the relativistic iron K$\alpha$ line for each observation is plotted as a function of the counts in the Iron K band. These were calculated as the product between the count rate in the 5-7 keV energy band and the exposure time of the single observation. Different symbols and colours correspond to different sources as presented in the legend. It is clear from the plot that when the observations have a low number of counts, the measurement of the equivalent width of the relativistic line gives mostly upper limits, unless the line is intrinsically very strong. In contrast, when the counts in the iron band are higher, in particular more than $\sim 4\times10^4$, we generally see evidence for the presence of a broad Fe K$\alpha$ line. Nevertheless, we do detect relativistic iron line at lower counts ($\sim 3\times10^3$) in Mrk 590, where the inferred equivalent width of the line ($\sim$ 450 eV) and is much larger than is typical value. In 6 out of 7 observations of NGC 5548, we measured upper limits to the presence of relativistic Fe K$\alpha$ emission line. In one observation, however, we find an apparently intense broad line with $EW \sim 500 \pm 250$ eV, albeit at low significance. It seems likely that this is due to Malmquist bias, whereby we see a positive statistical fluctuation in the line strength resulting in an apparent detection of a strong line, when the true EW is much lower. We further note that at some epochs this source exhibits absorption features in the Fe K-band. This might prevent a proper analysis of the iron K line (e.g. Liu et al. 2010, Kaastra et al.

2014). We note that while the trend of positive detections at high signal-to-noise ratio is clear, there are also spectra with high statistics in the Fe K-band where only upper limits are obtained, most notably for IC 4329A, where one such upper limit is inconsistent with the detections in the same object. This is discussed further in Section 4.4.1. The results on this source are consistent with the previous work of Mantovani et al. (2014) where the same *Suzaku* observations were analyzed. The authors pointed out that the relativistic line in this object is relatively weak and detected with high significance only when the data are combined together.

The main result of our analysis i.e. the need for high signal-to-noise ratio in the detection of broad lines, is in agreement with previous works centred on samples of sources observed with *XMM-Newton* (e.g., Guainazzi et al. 2006, de La Calle Pérez et al. 2010, Bhayani & Nandra 2011).

## 4.4 A Self-Consistent Reflection Model

The Relativistic Relline model used in the analysis described above provides an improvements to the fit in many cases. However, this model is not self-consistent. As presented in Section 1.4, the accretion disk is expected to be optically thick and the emission of a relativistic iron line should be accompanied by a reflection continuum which is modified by the same relativistic effects as the line. Furthermore, if the narrow emission line arises from optically thick material, such as the torus, it should be accompanied by reflection, too. This is allowed for in our fit by the *pexrav* component in the Baseline model. However, in order to be physically self-consistent, the strength of this component should be linked to that of the associated Fe line.

To provide a more physical and self-consistent model for the spectra in our sample, we adopted the *pexmon* model (Nandra et al. 2007). This model reproduces the main features of the reflection spectrum, which is produced by the interaction of the primary X-ray continuum with a Compton thick layer of neutral material (e.g. accretion disk, torus). This model is combining: i) narrow Fe K$\alpha$ line at 6.4 keV; ii) narrow Fe K$\beta$ line at 7.06 keV; iii) narrow Ni K$\alpha$ line at 7.47 keV; iv) Compton reflection, modelled with a *pexrav* component and v) Fe K$\alpha$ Compton shoulder. It is important to note that the Fe K$\beta$ and Ni K$\alpha$ line fluxes are linked to that of the Fe K$\alpha$ line. In particular, they are fixed to 11.3 and 5 per cent of that of the K$\alpha$ line, respectively (George & Fabian 1991). We then adopted two such *pexmon* components, one modified by relativistic effects, assumed to originate from the inner parts of the disk, and another which is not (e.g. from the torus): we term this the Relativistic Pexmon model (RP) *zwabs*(cutoffpl+pexmon+relconv*pexmon)*. This model fits not only the iron K$\alpha$ emission lines, but also self consistently reproduces the high energy reflection continua associated with both the narrow and the relativistic lines. To model the relativistic effects, we convolved the second *pexmon* with the *relconv* model (Dauser et al. 2010). This relativistically smears the whole reflection spectrum using the same kernel as the *relline* emission line model (Dauser et al. 2010). As in the Relativistic Relline model, the *zwabs* model was introduced only for IC 4329A and NGC 5506 with

Table 4.7: The table shows the $\chi^2$/d.o.f. for the model with a relativistic Fe K$\alpha$ line (Relativistic Relline model) and for the self-consistent model (Relativistic Pexmon model). We also report the $\Delta\chi^2/\Delta$d.o.f. between the two models, expressed as $\chi^2_{RP} - \chi^2_{RR}$.

| Source | Observation ID | Relativistic Relline Model | Relativistic Pexmon Model | $\Delta\chi^2/\Delta$d.o.f. |
|---|---|---|---|---|
| NGC 5506 | 701030010 | 1348.65/1334 | 1369.46/1335 | 20.81/1 |
| | 701030020 | 1423.86/1403 | 1431.75/1404 | 7.89/1 |
| | 701030030 | 1381.03/1377 | 1386.33/1378 | 5.3/1 |
| IC 4329A | 702113010 | 923.58/876 | 917.12/877 | -6.46/1 |
| | 702113020 | 1092.91/1093 | 1148.52/1094 | 55.61/1 |
| | 702113030 | 990.03/989 | 988.59/990 | -1.44/1 |
| | 702113040 | 908.35/861 | 908.75/862 | 0.4/1 |
| | 702113050 | 585.23/586 | 592.92/587 | 7.69/1 |
| | 707025010 | 1656.27/1639 | 1658.91/1640 | 2.64/1 |
| MCG +8-11-11 | 702112010 | 1236.05/1324 | 1358.79/1325 | 122.74/1 |
| NGC 7213 | 701029010 | 671.73/689 | 672.52/690 | 0.79/1 |
| MRK 110 | 702124010 | 545.66/546 | 549.12/547 | 3.46/1 |
| NGC 7469 | 703028010 | 637.81/667 | 625.46/668 | -12.35/1 |
| NGC 5548 | 702042010 | 83.01/101 | 84.14/102 | 1.13/1 |
| | 702042020 | 233.10/188 | 229.29/189 | -3.81/1 |
| | 702042040 | 328.70/312 | 326.69/313 | -2.01/1 |
| | 702042050 | 222.19/230 | 222.01/231 | -0.17/1 |
| | 702042060 | 389.54/374 | 390.92/375 | 1.38/1 |
| | 702042070 | 253.00/295 | 255.41/ 296 | 2.41/1 |
| | 702042080 | 172.86/180 | 172.70/181 | -0.16/1 |
| MRK 590 | 705043010 | 198.71/186 | 198.37/187 | -0.34/1 |
| | 705043020 | 102.35/116 | 100.94/117 | -1.41/1 |

fixed column densities of $N_H = 0.4 \times 10^{22}$ cm$^{-2}$ and $N_H = 3 \times 10^{22}$ cm$^{-2}$, respectively. As before, we also fixed the high energy cut-off for these two sources to 180 keV and 130 keV, while for the other sources in the sample we adopted 300 keV. The iron abundance was always fixed to the solar value, while in the *relconv* model we fixed the following parameters: i) index1 = index2 = 3; ii) $R_{break} = 15$ $r_g$; iii) $R_{out} = 400$ $r_g$; iv) limb = 0. For each source, we adopted the combination of inclination and inner radius as in the Relativistic Relline model (see Table 4.6). The spin parameter was assumed to be a = 0 for $r_{in} = 6$ $r_g$ and a = 0.998 for $r_{in} = 1.24$ $r_g$.

Table 4.7 presents the $\chi^2$/d.o.f. for the Relativistic Relline model and for the Relativistic Pexmon model. We also report the $\Delta\chi^2/\Delta$d.o.f. between these two models in order to investigate which one is fitting better the data. This is expressed as $\chi^2_{RP}$-$\chi^2_{RR}$. This test is important to understand whether the strength of the iron emission line and the emission of the Compton hump at higher energies are simultaneously well-fitted, since the *pexmon* model links these two quantities, while the *relline* model does not. This analysis shows that in general the physically self-consistent model provides a similar or better fit compared to the phenomenological one. This shows the consistency between the strength of the Fe K$\alpha$ line and the reflection continuum at high energies (i.e. Compton hump). However, in two cases, MCG +8-11-11 and IC 4329A Obs. ID 702113020, the $\Delta\chi^2$ between the Relativistic Pexmon model and the Relativistic Pexmon model is large ($\Delta\chi^2 > 50$). This might suggest a lack of connection between the Fe K$\alpha$ line and the hard X-ray continuum in these objects and/or during these observations. In the next section, we investigate this issue in more detail for these two observations.

### 4.4.1 The case of MCG +8-11-11 and IC 4329A

In this section we present the two extreme cases where the Relativistic Relline model gives a better fit to the data compared to the Relativistic Pexmon model: MCG +8-11-11 and one observation of IC 4329A (Obs. ID 702113020).

The case of MCG +8-11-11 has been already noticed as peculiar by Bianchi et al. (2010). A relativistic iron K$\alpha$ emission line was found in the same *Suzaku* observation analysed in this work. However, no reflection component was detected at higher energies. The results we found in our analysis are fully consistent with this result (see Table 4.6). In fact, when the Relativistic Pexmon model is applied to the data, it leads to an inadequate fit ($\Delta\chi^2 = 122.74$) compared to the Relativistic Relline model. The reason is that, in the former, the Compton hump is linked to the strength of the Fe emission line, while in the latter they are completely independent. This can be discerned immediately from the parameters in Table 4.6. The reflection fraction $R$ for MCG +8-11-11 is very small and well constrained to be $R = 0.12^{+0.06}_{-0.05}$. Conversely, both the narrow and relativistic iron lines are well detected and have a combined equivalent width of 156 eV, corresponding to a total reflection fraction of R $\sim$ 1.

Figure 4.4 shows the unfolded spectrum for this observation of this source. The components of the Relativistic Pexmon are plotted in different colours. The red, blue and green lines correspond to the narrow *pexmon*, to the blurred *pexmon* and to the Fe XXVI emission line, respectively. The black line represents the total model. The plot shows the best fit model of the XIS spectrum extrapolated to the high energies covered by the PIN data. For comparison, we plotted also the PIN spectrum. The bottom panel shows the data to model ratio for both the XIS and PIN spectra. It is evident that the Relativistic Pexmon model greatly overestimates the amount of emission at high energies.

Physically, there are several possible interpretations for the appearance of the spectrum of MCG +8-11-11. The first is that the line emission arises from material of small optical depth, producing a line but with little Compton scattering, and hence a weak Compton hump. However, this interpretation is very unlikely: the emission line in this spectrum is strong and low optical depth material would likely underproduce the emission line unless other circumstances were in play. A second possibility is that the Fe abundance of the material is higher than solar. This would produce a relatively strong emission line compared

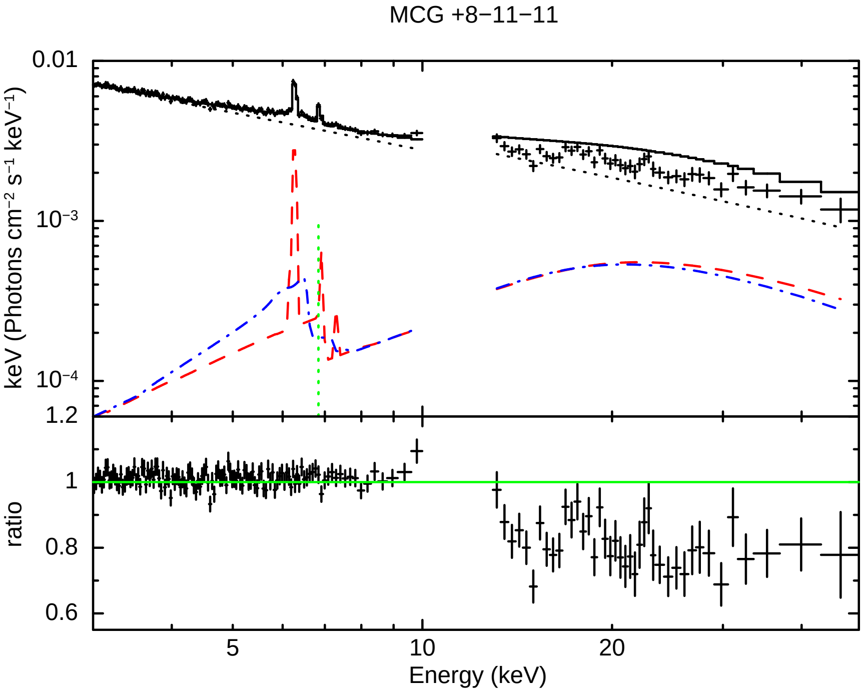

Figure 4.4: Unfolded spectrum for MCG +8-11-11. The Relativistic Pexmon model is applied only to the XIS data and extrapolated to the energies of the PIN spectrum. This model is clearly overestimating the amount of reflection because of the presence of a relativistic iron K$\alpha$ line.

to the Compton hump. We test this hypothesis by letting the iron abundance free to vary in the two *pexmon* models. In this way the fit does improve ($\chi^2$/d.o.f. = 1238.17/1323). However, the values of the iron abundance for the two components of the *pexmon* model are very extreme ($A_{Fe}/A_{Solar} \sim 100$). This explanation therefore seems to be unlikely. While the Fe abundance can explain an anomalous ratio of the line to the continuum, it does not explain why the absolute value of the reflection fraction as measured by the Compton hump is so low in this source. The most likely explanation for the appearance of the spectrum of MCG +8-11-11 is related to the assumption we made for the high energy cut-off. We assumed a value for this parameter of 300 keV. This ensures that there are plentiful high energy photons which can be downscattered into the Compton hump. If the temperature of the corona is lower, there will accordingly be less high energy photons to generate the high energy reflection continuum and Compton hump. We tested this hypothesis by fitting both the XIS and PIN spectra imposing a lower value, 50 keV, in both the Relativistic Relline and Relativistic Pexmon model. The $\chi^2$/d.o.f. now are comparable (Relativistic Relline: $\chi^2$/d.o.f. = 1262.03/1324; Relativistic Pexmon: $\chi^2$/d.o.f. = 1262.31/1325).

Finally, we tested the hypothesis of ionized reflection in this object. We fitted the data with the *relxill* model (García et al. 2014) together with a narrow *pexmon* component. The *relxill* model reproduces the entire reflection spectrum produced by ionized material and modified by strong gravity effects, i.e. produced in the inner regions of the accretion disk.

The best fit $\chi^2/d.o.f.$ for this model is 1254.91/1322, which is comparable to that obtained with the Relativistic Relline model. The model fit constraints the inclination of the disk, the reflection fraction and the high energy cut-off of the primary continuum: $\theta = 38^{+4}_{-5}$, $R = 0.20^{+0.10}_{-0.08}$ and $E_c = 68^{+15}_{-11}$ keV. The hypothesis of an ionized disk is therefore also a plausible explanation for the unusual scenario in MCG +8-11-11, although the rather low reflection fraction is puzzling.

The case of IC 4329A Obs. ID 702113020 appears to be the opposite situation of MCG +8-11-11. In this spectrum, a relativistic iron K$\alpha$ emission line is not significantly detected. However, a significant contribution of the reflection continuum at high energies is present and it is well constrained (see Table 4.6). This case is particularly puzzling because the other *Suzaku* observations of the same source show a relativistic iron K$\alpha$ emission line, albeit relatively weak (see also Mantovani et al. 2014).

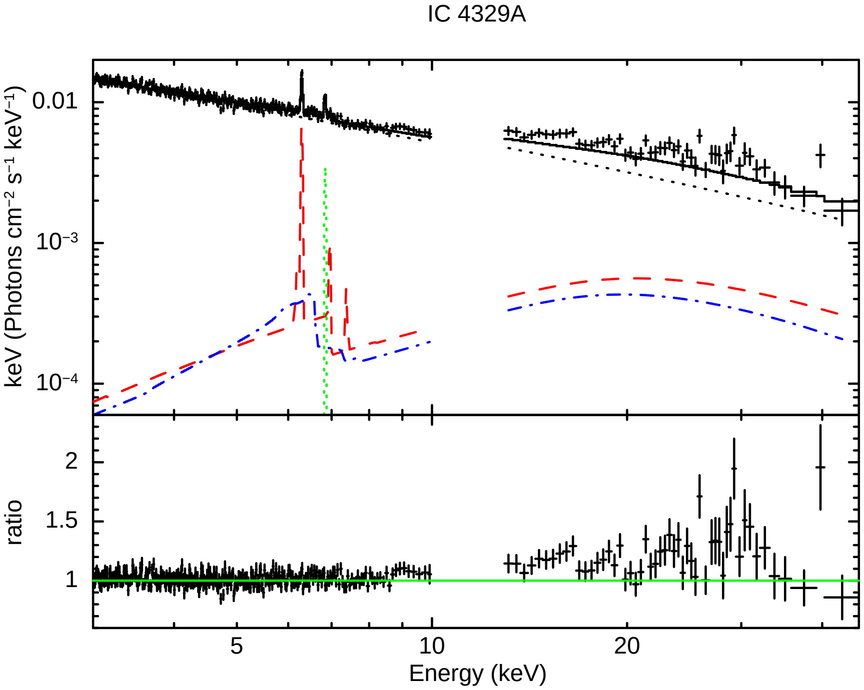

Figure 4.5: Unfolded spectrum for IC 4329A (Obs. ID 702113020). The Relativistic Pexmon model is applied only to the XIS spectrum and extrapolated to the PIN data. In this observation the broad Fe K$\alpha$ line is not significantly detected. However, Compton reflection is important. In this case, the *pexmon* model underestimates the reflection at high energies.

Figure 4.5 shows the unfolded spectrum for this spectrum when the Relativistic Pexmon model is applied only to the XIS spectrum and extrapolated to high energies. Also in this case, we plotted for comparison the PIN data. The red, blue and green lines corresponds to the narrow *pexmon*, to the blurred *pexmon* and to the Fe XXVI emission line, as in the previous case of MCG +8-11-11. For this observation, the *pexmon* model underestimates the amount of reflection at high energies. This is consistent with the fact that the relativistic iron line is not significantly detected. We then fitted only the XIS spectrum with the Relativistic Relline and Relativistic Pexmon models. The $\Delta\chi^2$ now is 6.91, much less then the value obtained when also the PIN data are considered ($\Delta\chi^2 = 55.61$). The best fits for the two models are now comparable. Formally, a sub-solar iron abundance can explain the weak iron K$\alpha$ emission line detected in this observations. We test this hypothesis letting this parameter free to vary in the fits of both the Relativistic Relline and Relativistic Pexmon model. The best-fit iron abundances for these two models indeed appear to be sub-solar (Relativistic Relline: $0.46^{+0.21}_{-0.15}$; Relativistic Pexmon: $0.25^{+0.09}_{-0.08}$). The difference in the goodness of the fit between the two also reduces substantially, with a $\Delta\chi^2 = 10.67$, much less than the $\Delta\chi^2$ of 55.61 obtained with solar abundances. However, in the other observations of the same source, IC 4329A, the abundances appear to be close to solar value. A variation of the iron abundance is highly unlikely if we consider that the time scale between each observation is short ($\sim$ 1 week). These observations of IC 4329A therefore provide a challenge to the prevailing reflection paradigm.

## 4.5 Discussion

In this chapter, we presented the analysis of a sample of Seyfert 1 galaxies observed with *Suzaku*. These sources had previously shown an absence of evidence for a relativistic Fe K$\alpha$ emission line in their *XMM-Newton* observations. The goals of this work are: i) to understand if the detection of this feature is strictly related to the signal-to-noise ratio, i.e. the relativistic iron line is ubiquitous feature in X-ray spectra, but the statistics of the spectra are not sufficient in order to disentangle it from the underlying continuum; ii) investigate if there is a relationship between the iron K$\alpha$ flux and the Compton hump emission at higher energies. This would be an important test on the reliability of the reflection model against more complex scenarios. To achieve these aims, we systematically fitted the spectra of all the sources in the sample with a series of models of varying complexity, testing for the presence of relativistic lines and their consistency with the Compton reflection hump at higher energies.

As in previous work, our analysis shows the presence of a peak at 6.4 keV in all the spectra, which can be easily identified with a narrow iron K$\alpha$ line emitted from relatively distant material. The majority of the sources shows additional complexities around the iron K band, however. Several sources show evidence for more ionised species, identified with Fe XXV and Fe XXVI. Beyond this, at least one observation of each source in our sample, and 12 out 22 in total, shows a significant improvement when a relativistic line is added to the model. Combining *XMM-Newton* and *Suzaku* observations of the sources analyzed in Nandra et al. (2007), the relativistic Fe K$\alpha$ line is detected in 13 out of 26 sources (50%), and in 35 out of 59 observations ($\sim$ 60%). Where the broad lines are detected in our sample, the typical equivalent widths are in the range 50-100 eV, and the upper limits in the cases of non-detections rarely exclude such values. This result is fully consistent with the work of Nandra et al. (2007), using *XMM-Newton* data, who found an average broad EW of $\sim$ 80 eV. Both are also consistent with the work of Patrick et al. (2012), where a sample of Seyfert 1 AGN was analyzed using *Suzaku* observations. In this case, the mean EW within the sample was found to be $96^{+10}_{-10}$ eV. It is interesting to note that the sources in our sample were chosen because the relativistic Fe line in the previous *XMM-Newton* spectra is weak and/or of low significance, but our results show that in reality they are entirely consistent with typical line strengths seen in more complete samples.

The results for the individual sources in our sample are broadly consistent with previous work. *XMM-Newton* observations of NGC 5506 revealed the presence of a broad residual in the Fe band once the narrow emission line is fitted (Matt et al. 2001). The iron emission complex was equally well fitted either with a truly broad line or a blend of He-like and H-like narrow lines. However, our analysis of the *Suzaku* spectra of this source shows that, even accounting for the presence of ionised emission lines, a relativistic Fe K$\alpha$ emission component is required in addition, with an equivalent width of $\sim$ 80 eV. The same observations were analyzed by Patrick et al. (2012) where a relativistic line was detected but with a lower value of equivalent width ($\sim$ 30 eV). In the work of Patrick et al. (2012), the parameters of the *relline* component, such as the emissivity index, the inclination and the inner radius, were let free to vary. However, since it is not straightforward to constrain these parameters, we assumed fixed values of $q = 3$, $\theta = 30°$ and $r_{in} = 6r_g$. Recently, a *NuSTAR* observation of NGC 5506 was analysed by Matt et al. (2015). In this spectrum, a relativistic iron K$\alpha$ line was not required in the fitting process, perhaps suggesting a variation of the intensity of the line between the *Suzaku* and the *NuSTAR* observations, which are separated by $\sim$ 7 years.

The results of the analysis of the bright Seyfert 1 galaxy, IC 4329A are consistent with the work of Mantovani et al. (2014). The same *Suzaku* observations were taken into account, however, in the current sample we included also another observation which is simultaneous to a *NuSTAR* observation. This *Suzaku* spectrum was analysed by Brenneman et al. (2014a) but only a moderately broad Fe K$\alpha$ line was detected using a simple gaussian model. The resulting equivalent width was $34^{+8}_{-7}$ eV. In this work, we considered all 6 *Suzaku* observations available in archive, which allowed us to better constrain the parameters of the relativistic Fe line, such as the inclination of the disk (30°) and the inner radius (6 $\mathrm{r}_g$), which are also in agreement with the previous work of Mantovani et al. (2014). We detected the relativistic line at 95 per cent confidence in 3 observations out of 6, with a mean value for the equivalent width of $\sim$ 90 eV. Mantovani et al. (2014) pointed out that this spectral feature was detected only in the combined data because of the weakness of this feature and relatively poor statistics of the single observations. Our results on this source are fully consistent with this scenario. The same observations were analyzed from Patrick et al. (2012). Using the same model component for modelling the relativistic iron line (i.e. *relline*), they found an equivalent width of $69^{+13}_{-14}$ eV, consistent with the value found in our analysis.

As discussed above, a relativistic iron K$\alpha$ line was already detected in MCG +8-11-11 in the same *Suzaku* spectrum by Bianchi et al. (2010), with an equivalent width of $\sim$ 90 eV. The result of our analysis is fully consistent with the work of Bianchi et al. (2010) (EW = $92^{+23}_{-23}$ eV).

Previous work on NGC 7213 (Lobban et al. 2010) did not reveal the presence of a relativistic emission line, whereas our analysis shows this component to be present in the same *Suzaku* spectrum. In their work, a *diskline* model was used assuming an inclination of the accretion disk of 30° and inner radius of $6r_g$, but an upper limit was found for the flux of the relativistic Fe line. However, in our work different combinations of inner radii and inclinations were tested. We do detect a relativistic Fe line with an equivalent width of $233^{+80}_{-80}$ eV adopting an inclination of 80° and an inner radius of 6 $r_g$.

As with the other objects in our sample, Mrk 110 is a source which did not show evidence for a relativistic Fe line component in previous *XMM-Newton* observations (Nandra et al. 2007). We do find evidence, albeit at marginal statistic significance (∼95 per cent confidence). The same *Suzaku* spectrum was also analyzed by Walton et al. (2013), who also found evidence for a broad Fe component.

Previous *Beppo-SAX* observations of NGC 7469 revealed the presence of both the relativistic Fe K$\alpha$ line (EW $= 121^{+100}_{-100}$ eV) and the associated Compton hump (De Rosa et al. 2002a). The results of our work are consistent with this work (EW$= 73^{+20}_{-20}$ eV). The same *Suzaku* spectrum was also analyzed by Patrick et al. (2012). These authors fitted the data and a relativistic line was detected with an equivalent width consistent within the errors with our result (EW$= 91^{+9}_{-8}$ eV).

Finally, there are two sources in our sample where the evidence for any relativistic Fe K$\alpha$ emission line is very weak, those being NGC 5548 and Mrk 590. We note that no broad line was detected in previous observations of these objects (NGC 5548: Brenneman et al. 2012, Patrick et al. 2012, Mrk 590: Longinotti et al. 2007). In both these sources, however, the constraints on any broad component in the spectra are poor, with upper limits typically of several 100 eV, usually in excess of the typical EW for the detected relativistic lines of $\sim$ 50-100 eV. It is important to note that each spectrum of those sources has low signal-to-noise ratio and the absence and/or low significance detections might be due to the low statistical quality of the data.

Taking advantage of the extended energy band of *Suzaku*, we were able also to investigate the relationship between the emission of the iron K$\alpha$ line and the reflection continuum at higher energies. Being features of the same reflection spectrum, they should correlate in time and respond simultaneously to variations of the primary X-ray continuum. We compared the fits with our Relativistic Relline model, which allows the iron line and the reflection strengths to vary independently, with a more self-consistent reflection model (Relativistic Pexmon model) in which the line and the Compton hump are linked in the ratio expected for a Compton-thick slab. For the majority of the observations (19/22), this self-consistent model gives a better or comparable fit to the data compared to the phenomenological Relativistic Relline model, despite having one less free parameter. This shows that in general the line and the reflection component in AGN are consistent with each other, in support of the idea that both arise from the same material and are features of the same reflection spectrum. In a few cases, the self-consistent model leads to a worse fit to the data compared to the phenomenological one. It is considerably worse in particular for two observations, that of MCG +8-11-11 and in one of the spectra of IC 4329A, which show a difference in fit statistic of $\Delta\chi^2 > 50$. Surprisingly, these two observations exhibit this behaviour for opposite reasons.

In MCG +8-11-11, as already noted by Bianchi et al. (2010), strong evidence for a relativistic iron line is present, but with the absence of any reflection emission at high energy. A possible explanation for the lack of reflection in this source could be a low temperature of the corona, i.e. a low high energy cut off (e.g. $\sim$ 50 keV). This hypothesis could be tested with higher quality data, as can be expected from e.g. *NuSTAR* observations.

The opposite situation appears in the case of one observation of IC 4329A (Obs. ID: 702113020). In this spectrum the relativistic iron line was not detected, with a tight upper limit, while a strong reflection continuum is observed at higher energies. This is puzzling especially if we consider this spectrum in the context with the other observations of IC 4329A with *Suzaku*. These do show a relativistic Fe K$\alpha$ emission line and a reflection continuum, with strengths which are typically consistent with each other. The lack of consistency in only one observation argues against some interpretations, such as an unusual Fe abundance in the material where the reflection is produced. A possible explanation for this problem could be a rapid variation of the geometry of the inner parts of the accretion disk. For example, a variability of the illuminations pattern and/or ionization state of the disk, or strong relativistic effects can play an important role (e.g. Iwasawa et al. 1996, Miniutti et al. 2003). These effects can produce unusual line and continuum properties, such as strong line profile variations, or extreme broadening of the line, which may be difficult to distinguish from the continuum. Overall, however, it is difficult to come up with a robust interpretation for why in this source the line and the reflection continuum appear not to follow each other. If these two components can exhibit differential variability of this kind, it is not only difficult to explain, but also to make predictions which could be tested. This is puzzling in the standard reflection model context, and unless an interpretational framework can be established, diminishes the diagnostic power of this framework.

## 4.6 Conclusion

The analysis presented above, shows that we do detect a relativistic emission line in IC 4329A, MCG +8-11-11, Mrk 110, NGC 5506, NGC 7213 and NCG 7469. These results are fully consistent with the hypothesis of ubiquitous relativistic Fe K$\alpha$ emission in the X-ray spectra of Seyfert 1 galaxies. The lack of detection in some sources and/or observations is mainly due to the low statistics (i.e. low signal-to-noise ratio) of some of the spectra analyzed. This result confirms previous conclusions from the analysis of *XMM-Newton* spectra, where it was claimed that high signal-to-noise ratio is necessary for the detection of broad Fe line of typical equivalent width (e.g. Guainazzi et al. 2006, Nandra et al. 2007, de La Calle Pérez et al. 2010). The analysis of our sample demonstrates that only when the counts in the iron band (5-7 keV) are higher than $\sim 4 \times 10^4$ is this feature consistently detected.

Another important result of our work is that the data are consistent with both the narrow and relativistic iron line tracing the emission of the Compton hump at higher energies. This confirms the idea that these features are part of the same reflection component produced by the same material, and supporting the reflection model in AGN. Except for two observations discussed in the previous section, in the majority of the cases the self-consistent model adopted in our analysis leads to a better or similar fit compared to the phenomenological model, where the iron line and the Compton hump fluxes are not linked. The results of our analysis show the great importance of the high energy X-ray data in constraining the continuum.

# Chapter 5

# Evidence for gravitational light-bending in two Seyfert galaxies

## 5.1 Introduction

The revolutionary sensitivity of *NuSTAR* in the hard X-ray band permits us to reduce the instrument background and obtain high signal-to-noise ratio spectra ($\sim$100 higher than the HDX-PIN detector onboard *Suzaku*). These data are of fundamental importance to study the relation between the emission of both the narrow and relativistic Fe K$\alpha$ lines and their associated emission at higher energies with an accuracy never achieved before. For these reasons, in this Chapter we apply the same analysis we did for the *Suzaku* data to a sample of sources observed with *NuSTAR*.

## 5.2 Sample Selection

The sample was selected starting from the sources analysed by Nandra et al. (2007). They compiled a complete sample of nearby Seyfert 1 objects ($z < 0.05$) from archival *XMM-Newton* observations, cross-correlated with the Véron-Cetty & Véron (2001) AGN catalogue. Seyfert 2 galaxies were excluded because of the obscuration of the central engine in the X-ray (see Section 4.2 for further details). From this sample, we selected the sources with *NuSTAR* observations available in archive. We present in Table 5.1 the objects selected for this work. We list the name of the source, the flux in the iron band (i.e. in the 5-7 keV band), the observation ID and the exposure time of each observation.

All the sources were observed with the two co-aligned telescopes with corresponding Focal Plane Modules A (FPMA) and B (FPMB). The data were reprocessed following the standard procedure as presented in Chapter 2. The spectra from both the FPMA and FPMB were used in the following analysis. We introduced a calibration constant, which is free to vary in all the fits between the two spectra. The energy range we adopted in the fitting process is 3-79 keV.

| Object | Flux 5-7 keV | Obs. ID | Exposure time |
|---|---|---|---|
| NGC 4151 | 5.07 | 60001111002 | 21.9 |
|  | 4.63 | 60001111003 | 57.0 |
|  | 5.42 | 60001111005 | 61.5 |
| IC 4329A | 2.42 | 60001045002 | 162.4 |
| MCG -5-23-16 | 2.24 | 10002019001 | 33.9 |
|  | 2.55 | 60001046002 | 160.5 |
| NGC 5506 | 1.34 | 60061323002 | 56.6 |
| MCG -6-30-15 | 1.05 | 60001047002 | 23.3 |
|  | 1.07 | 60001047003 | 127.2 |
|  | 0.72 | 60001047005 | 29.6 |
| NGC 5548 | 0.98 | 60002044002 | 24.1 |
|  | 0.93 | 60002044003 | 27.3 |
|  | 0.80 | 60002044005 | 49.5 |
|  | 0.92 | 60002044006 | 51.5 |
|  | 0.72 | 60002044008 | 50.1 |
| ARK 120 | 0.58 | 60001044002 | 55.3 |
| NGC 4051 | 0.46 | 60001050003 | 45.7 |
|  | 0.35 | 60001050005 | 10.2 |
|  | 0.26 | 60001050006 | 49.6 |
|  | 0.70 | 60001050008 | 56.7 |
| NGC 4395 | 0.22 | 60061322002 | 19.2 |
| NGC 3516 | 0.11 | 60002042002 | 51.0 |
|  | 0.15 | 60002042004 | 72.1 |

Table 5.1: Sample: these objects are selected from Nandra et al. (2007) and having *NuSTAR* observations public in archive. The continuum flux in the iron K band is expressed in units of $10^{-11}$ erg cm$^{-2}$ s$^{-1}$, while the exposure time of each observation is in ks.

## 5.3 Sample Data Analysis

We started our analysis of the sources presented in Table 5.1 assuming a simple model, systematically applied to all the sources in our sample. The model adopted (Gaussian Model) includes a cut-off power law which models the primary X-ray continuum as well as the reflection continuum and a Gaussian model for fitting the narrow iron K$\alpha$ emission line produced by neutral and distant material (*pexrav+zgauss* in *xspec*). The *pexrav* model (Magdziarz & Zdziarski 1995) takes into account both the power law with the high energy cut-off and the neutral reflection. We included a neutral absorber at the redshift of the source (*zwabs* in *xspec*) for modelling the spectra of NGC 5506, NGC 4151 and IC 4329A. The column density of hydrogen was left as a free parameter for the first two objects, while for IC 4329A it was fixed at the same value presented in the previous analysis of the *Suzaku* spectra, i.e. $N_H = 0.4 \times 10^{22}$ cm$^{-2}$ (Mantovani et al. 2014). The value found for NGC 5506 ($N_H = 3.39^{+0.21}_{-0.35} \times 10^{22}$ cm$^{-2}$) is consistent within the errors with the analysis presented in Chapter 4 based on *Suzaku* observations, while for NGC 4151 the column density was measured to be $N_H = 6.39 \pm 0.88 \times 10^{22} cm^{-2}$. The column density of the other objects is not reported because it does not exceed the Galactic one.

Table 5.2 reports the best-fit parameters of these fits. The energies of the Gaussian component in all the spectra analysed are fully consistent with a neutral narrow Fe K$\alpha$ emission line, emitted from distant material. The slopes of the power law which models the primary X-ray continuum are different from source to source, but they are typical of the values observed in the spectra of other Seyfert galaxies ($\Gamma \sim$ 1.7-1.8, Piconcelli et al. 2005, Bianchi et al. 2009). In the cases of NGC 4051 and MCG -6-30-15 we measured slightly higher photon indices. The cross-normalization constant between the spectra from the two modules A and B is always consistent with unity, as expected for flux calibrated spectra. One important parameter for our studies is the reflection fraction R (see Section 1.4 for more details). R = 1 corresponds to a slab reflector subtending a solid angle of $\Omega/2\pi = 1$ at the primary source. For the majority of the objects in our sample (70%) the reflection fraction is less than 1 (R $\sim$ 0.5), meaning that the reflector covers less than half of the sky seen by the primary source (see Section 1.4). Interestingly, in two cases, namely NGC 4051 and MCG -6-30-15, this parameter exhibits values grater than unity in the Gaussian model, R $\sim$ 3.50 and R $\sim$ 2, respectively. These values of the reflection fraction indicate a larger amount of reflection coming from the disc compared to the standard picture. This scenario assumes that the primary X-ray source is located above the accretion disk which is covering half of the sky seen by the corona (George & Fabian 1991). The results on MCG -6-30-15 and NGC 4051 can be interpreted by considering that the X-ray primary source is located above the disk at a height of a few gravitational radii and sufficiently close to the central black hole that strong gravitational effects, such as light bending, become important (for further details see Section 5.4.2). If this is the case, more than half of the photons emitted by the corona can be bent onto the accretion disk. This phenomenon boosts the flux reflected by the disk and decreases the primary continuum detected by the observer at infinity, therefore increasing the value of $R$.

We now focus our attention on these two sources only. We further investigated the spectra of these objects with the aim to understand which process is responsible for the reflection fraction being higher than unity and testing whether this could be due to gravitational light bending.

| Source | Observation | $N_H$ | $\Gamma$ | $E_{cutoff}$ | R | $N_{pexrav}$ | $E_{K\alpha}$ | $F_{K\alpha}$ | $EW_{K\alpha}$ | Constant | $Flux_{2-10keV}$ | $\chi^2$/d.o.f. |
|---|---|---|---|---|---|---|---|---|---|---|---|---|
| ARK 120 | 2013-02-18 | - | $1.87^{+0.04}_{-0.03}$ | $> 3829.17$ | $0.56^{+0.13}_{-0.13}$ | $0.76^{+0.04}_{-0.04}$ | $6.40^{+0.07}_{-0.01}$ | $4.07^{+0.48}_{-0.47}$ | $149.20^{+17.52}_{-17.18}$ | $1.02^{+0.01}_{-0.01}$ | $0.25^{+0.01}_{-0.01}$ | 800.49/807 |
| MCG -5-23-16 | 2012-07-11 | - | $1.73^{+0.02}_{-0.02}$ | $85.01^{+12.74}_{-8.76}$ | $0.86^{+0.13}_{-0.12}$ | $2.40^{+0.10}_{-0.08}$ | $6.37^{+0.02}_{-0.08}$ | $10.56^{+1.11}_{-1.12}$ | $102.72^{+10.83}_{-10.89}$ | $1.05^{+0.01}_{-0.01}$ | $0.95^{+0.01}_{-0.01}$ | 1136.62/1106 |
| | 2013-06-03 | - | $1.72^{+0.01}_{-0.01}$ | $76.34^{+3.78}_{-3.51}$ | $0.65^{+0.05}_{-0.05}$ | $2.76^{+0.04}_{-0.04}$ | $6.374^{+0.001}_{-0.001}$ | $12.02^{+0.59}_{-0.50}$ | $103.67^{+5.07}_{-4.28}$ | $1.035^{+0.003}_{-0.003}$ | $1.08^{+0.01}_{-0.01}$ | 2277.65/1839 |
| NGC 4051 | 2013-06-17B | - | $2.19^{+0.07}_{-0.06}$ | $> 257.46$ | $3.06^{+0.71}_{-0.60}$ | $0.91^{+0.08}_{-0.07}$ | $6.33^{+0.04}_{-0.04}$ | $1.95^{+0.45}_{-0.44}$ | $92.84^{+21.19}_{-21.1}$ | $1.05^{+0.02}_{-0.02}$ | $0.21^{+0.01}_{-0.01}$ | 719.03/654 |
| | 2013-10-09A | - | $2.24^{+0.26}_{-0.24}$ | $> 119.81$ | $5.62^{+3.24}_{-2.75}$ | $0.63^{+0.14}_{-0.14}$ | $6.41^{+0.08}_{-0.09}$ | $1.95^{+1.34}_{-0.98}$ | $125.76^{+86.06}_{-63.01}$ | $1.06^{+0.04}_{-0.04}$ | $0.15^{+0.02}_{-0.02}$ | 193.54/181 |
| | 2013-10-09B | - | $1.85^{+0.09}_{-0.08}$ | $123.07^{+67.48}_{-33.93}$ | $2.82^{+0.90}_{-0.67}$ | $0.29^{+0.01}_{-0.03}$ | $6.29^{+0.04}_{-0.11}$ | $1.86^{+0.35}_{-0.35}$ | $155.85^{+29.3}_{-29.14}$ | $1.04^{+0.02}_{-0.02}$ | $0.11^{0.01}_{-0.01}$ | 661.45/554 |
| | 2014-02-16 | - | $2.27^{+0.03}_{-0.05}$ | $> 12025.1$ | $2.39^{+0.48}_{-0.36}$ | $1.66^{+0.09}_{-0.09}$ | $6.30^{+0.08}_{-0.04}$ | $2.38^{+0.50}_{-0.50}$ | $74.53^{+15.78}_{-15.76}$ | $1.01^{+0.01}_{-0.01}$ | $0.33^{+0.01}_{-0.01}$ | 833.30/782 |
| NGC 4151 | 2012-11-12A | $5.26^{+0.34}_{-0.39}$ | $1.59^{+0.04}_{-0.04}$ | $83.51^{+9.09}_{-8.54}$ | $0.88^{+0.12}_{-0.12}$ | $4.75^{+0.36}_{-0.33}$ | $6.301^{+0.029}_{-0.001}$ | $24.38^{+2.38}_{-2.52}$ | $92.74^{+9.05}_{-9.59}$ | $1.004^{+0.006}_{-0.006}$ | $1.69^{+0.01}_{-0.01}$ | 1618.51/1369 |
| | 2012-11-12B | $7.56^{+0.28}_{-0.26}$ | $1.51^{+0.03}_{-0.03}$ | $88.24^{+5.85}_{-5.45}$ | $0.71^{+0.06}_{-0.06}$ | $3.98^{+0.19}_{-0.20}$ | $6.34^{0.001}_{-0.001}$ | $31.20^{+1.53}_{-1.39}$ | $125.91^{+6.18}_{-5.61}$ | $1.040^{+0.004}_{-0.004}$ | $1.45^{+0.01}_{-0.01}$ | 2488.34/1871 |
| | 2012-11-14 | $6.35^{+0.19}_{-0.23}$ | $1.56^{+0.02}_{-0.02}$ | $95.02^{+6.26}_{-5.63}$ | $0.68^{+0.05}_{-0.03}$ | $4.99^{+0.21}_{-0.21}$ | $6.34^{+0.01}_{-0.04}$ | $30.17^{+1.58}_{-0.79}$ | $105.58^{+5.53}_{-2.75}$ | $1.045^{+0.004}_{-0.004}$ | $1.76^{+0.01}_{-0.01}$ | 2644.57/1948 |
| MCG -6-30-15 | 2013-01-29 | - | $2.21^{+0.06}_{-0.06}$ | $117.52^{+55.33}_{-29.90}$ | $2.25^{+0.58}_{-0.46}$ | $2.35^{+0.18}_{-0.16}$ | $6.33^{+0.08}_{-0.04}$ | $4.26^{+0.95}_{-0.91}$ | $89.20^{+19.84}_{-19.02}$ | $1.02^{+0.01}_{-0.01}$ | $0.48^{+0.01}_{-0.01}$ | 635.12/652 |
| | 2013-01-30 | - | $2.13^{+0.02}_{-0.02}$ | $172.99^{+42.03}_{-29.46}$ | $1.47^{+0.15}_{-0.14}$ | $2.20^{+0.06}_{-0.06}$ | $6.408^{+0.002}_{-0.033}$ | $3.64^{+0.39}_{-0.39}$ | $75.20^{+7.97}_{-8.04}$ | $1.03^{+0.01}_{-0.01}$ | $0.49^{+0.01}_{-0.01}$ | 1453.51/1290 |
| | 2013-02-02 | - | $2.04^{+0.06}_{-0.06}$ | $172.35^{+129.87}_{-54.02}$ | $2.00^{+0.52}_{-0.42}$ | $1.25^{+0.11}_{-0.09}$ | $6.27^{+0.08}_{-0.08}$ | $3.27^{+0.70}_{-0.68}$ | $97.52^{+20.77}_{-20.30}$ | $1.03^{+0.02}_{-0.02}$ | $0.32^{+0.01}_{-0.01}$ | 693.97/663 |
| IC 4329A | 2012-08-12 | 0.4 (fixed) | $1.78^{+0.01}_{-0.01}$ | $244.17^{+43.64}_{-31.72}$ | $0.45^{+0.04}_{-0.04}$ | $2.92^{+0.04}_{-0.04}$ | $6.38^{0.01}_{-0.05}$ | $7.74^{+0.56}_{-0.55}$ | $66.49^{+4.81}_{-4.73}$ | $1.043^{+0.004}_{-0.003}$ | $1.03^{+0.01}_{-0.01}$ | 2005.54/1840 |
| NGC 5506 | 2014-04-01 | $3.39^{+0.21}_{-0.35}$ | $1.97^{+0.02}_{-0.02}$ | $> 9715.62$ | $1.46^{+0.17}_{-0.09}$ | $2.13^{+0.10}_{-0.15}$ | $6.400^{+0.039}_{-0.002}$ | $7.25^{+0.73}_{-0.72}$ | $112.78^{+11.32}_{-11.19}$ | $1.003^{+0.008}_{-0.008}$ | $0.48^{+0.01}_{-0.01}$ | 1271.83/1160 |
| NGC 3516 | 2014-06-24 | - | $1.44^{+0.06}_{-0.08}$ | $> 92.86$ | $< 0.52$ | $0.006^{+0.001}_{-0.001}$ | $6.46^{+0.04}_{-0.04}$ | $1.78^{+0.24}_{-0.23}$ | $395.82^{+54.06}_{-51.57}$ | $1.10^{+0.03}_{-0.03}$ | $0.04^{+0.01}_{-0.01}$ | 361.76/294 |
| | 2014-07-11 | - | $1.55^{+0.06}_{-0.06}$ | $> 152.31$ | $0.39^{+0.25}_{-0.22}$ | $0.11^{+0.01}_{-0.01}$ | $6.42^{+0.04}_{-0.04}$ | $1.76^{+0.23}_{-0.21}$ | $277.23^{+35.97}_{-33.8}$ | $1.03^{+0.02}_{-0.02}$ | $0.06^{+0.01}_{-0.01}$ | 560.89/518 |
| NGC 4395 | 2013-05-10 | - | $1.17^{+0.09}_{-0.09}$ | $51.45^{+33.46}_{-14.70}$ | $< 0.43$ | $0.09^{+0.01}_{-0.01}$ | $6.42^{+0.14}_{-0.14}$ | $1.25^{+0.47}_{-0.47}$ | $129.38^{+48.43}_{-48.39}$ | $1.04^{+0.03}_{-0.03}$ | $0.08^{+0.01}_{-0.01}$ | 239.71/248 |
| NGC 5548 | 2013-07-11 | - | $1.46^{+0.03}_{-0.03}$ | $106.34^{+38.64}_{-22.64}$ | $0.14^{+0.13}_{-0.11}$ | $0.69^{+0.04}_{-0.04}$ | $6.35^{+0.08}_{-0.08}$ | $4.03^{+0.90}_{-0.88}$ | $86.49^{+19.27}_{-18.85}$ | $1.03^{+0.01}_{-0.01}$ | $0.41^{+0.01}_{-0.01}$ | 870.90/764 |
| | 2013-07-12 | - | $1.55^{+0.04}_{-0.04}$ | $111.79^{+42.96}_{-24.63}$ | $0.35^{+0.16}_{-0.14}$ | $0.75^{+0.04}_{-0.04}$ | $6.31^{+0.08}_{-0.04}$ | $3.97^{+0.83}_{-0.84}$ | $89.30^{+18.63}_{-18.82}$ | $1.06^{+0.01}_{-0.01}$ | $0.38^{+0.01}_{-0.01}$ | 741.79/757 |
| | 2013-07-23 | - | $1.31^{+0.03}_{-0.03}$ | $60.16^{+6.31}_{-6.68}$ | $0.18^{+0.08}_{-0.08}$ | $0.44^{+0.01}_{-0.01}$ | $6.36^{+0.04}_{-0.02}$ | $5.63^{+0.61}_{-0.57}$ | $150.98^{+16.35}_{-15.3}$ | $1.03^{+0.01}_{-0.01}$ | $0.32^{+0.01}_{-0.01}$ | 993.95/959 |
| | 2013-09-10 | - | $1.59^{+0.03}_{-0.03}$ | $83.10^{+16.54}_{-11.42}$ | $0.53^{+0.14}_{-0.13}$ | $0.79^{+0.03}_{-0.03}$ | $6.39^{+0.04}_{-0.02}$ | $4.60^{+0.61}_{-0.62}$ | $107.05^{+14.16}_{-14.31}$ | $1.05^{+0.01}_{-0.01}$ | $0.38^{+0.01}_{-0.01}$ | 990.47/956 |
| | 2013-12-20 | - | $1.25^{+0.03}_{-0.03}$ | $51.82^{+6.01}_{-5.02}$ | $0.24^{+0.11}_{-0.10}$ | $0.35^{+0.02}_{-0.02}$ | $6.37^{+0.04}_{-0.04}$ | $5.07^{+0.55}_{-0.65}$ | $151.57^{+16.42}_{-19.29}$ | $1.02^{+0.01}_{-0.01}$ | $0.28^{+0.01}_{-0.01}$ | 917.69/955 |

Table 5.2: Best fit parameters for the Gaussian Model. The column density is in units of $10^{22}$ $cm^{-2}$ and the normalization of the primary continuum is in units of $10^{-2}$ photons keV$^{-1}$ cm $^{-2}$ s$^{-1}$. The high energy cut-off is expressed in keV as the energy of the Fe K$\alpha$ line. The equivalent width is in eV while the continuum flux in the 3 to 10 keV band in $10^{-11}$ erg s$^{-1}$ cm$^{-2}$.

## 5.4 MCG -6-30-15 and NGC 4051

### 5.4.1 Introduction

#### MCG -6-30-15

A relativistic Fe K$\alpha$ emission line was first detected in the *ASCA* spectrum of the bright Seyfert 1 galaxy MCG -6-30-15 (Tanaka et al. 1995). The *ASCA* spectrum showed the presence of a broad and asymmetric line profile, suggesting that the line is produced within 6 gravitational radii from the black hole (Iwasawa et al. 1996). Indeed, the red wing of the line was observed to extend down to 4 keV. This indicated emission from very small radii and therefore implying that the black hole at the center of this object is rapidly rotating (Iwasawa et al. 1999). The broad Fe line in this source has been subsequently detected in the spectra of many X-ray missions, *ASCA* (Shih et al. 2002, Matsumoto et al. 2003), *RXTE* (Lee et al. 1999, Vaughan & Edelson 2001), *BeppoSAX* (Guainazzi et al. 1999), *Suzaku* (Miniutti et al. 2007, Noda et al. 2011), *Chandra* (Lee et al. 2001, Young et al. 2005) and *XMM-Newton* (Wilms et al. 2001, Fabian et al. 2002, Fabian & Vaughan 2003, Vaughan & Fabian 2004, Brenneman & Reynolds 2006). Consistent results have generally been found from the analysis of these different spectra.

The longest *XMM-Newton* observation ($\sim$ 320 ks) was analyzed by Fabian et al. (2002) and Vaughan & Fabian (2004). Thanks to the large effective area provided by this satellite, it was possible to constrain the most important parameters associated with the emission of the relativistic Fe K$\alpha$ line: the inclination of the disk was found to be $\theta = 33^\circ \pm 0.1$ and the emissivity profile was found to be inconsistent with a simple power law. Instead a broken power law profile was required to fit the data with inner and outer emissivity indices of $q_{in} = 6.9 \pm 0.6$ and $q_{out} = 3.0 \pm 0.1$, respectively, and a break radius of $r_{br} = 3.4 \pm 0.2$. The inner radius of the accretion disk was measured to be $r_{in} = 1.8 \pm 0.1\ r_g$, confirming previous results (e.g. Tanaka et al. 1995, Iwasawa et al. 1996, 1999, Shih et al. 2002) and implying emission beyond the last stable orbit of a Schwarzschild BH. This was later confirmed by Brenneman & Reynolds (2006), who found a rapidly rotating black hole with a spin parameter $a = 0.96 \pm 0.01$. The best-fit parameters found by Fabian et al. (2002) and Vaughan & Fabian (2004) indicate a strong reflection fraction in this source $R = 2.2$, consistent with a previous *BeppoSAX* observation (Guainazzi et al. 1999).

Different scenarios have been proposed in order to explain the broad red wing of the line without the need for relativistic effects close to the black hole. The most popular is the absorption scenario (Miller et al. 2008, 2009). In this picture, the primary continuum passes through a series of components with large columns of ionized gas partially covering the central source, which can produce a prominent curvature around the energy of the Fe K$\alpha$ line. When the absorption model is applied to the *XMM-Newton* data, in order to model the 3-6 keV spectral curvature, narrow absorption lines between 6.4 keV and 6.7 keV are predicted. However, these features are not detected in the high resolution *Chandra* data (Young et al. 2005), indicating that this particular absorption model can not reproduce entirely the red wing of the Fe line without invoking relativistic effects.

It has be noted that the soft X-ray spectrum of this object is characterized by the presence of warm absorbers, which affect the data below 3 keV. This complex structure has been studied by Otani et al. 1996 using *ASCA* data, which showed the presence of two variable warm absorbers. The dusty warm absorber in MCG -6-30-15 has been analyzed in detail, taking advantage of the high resolution spectra of the *Chandra* HETGS (Lee et al. 2001, Young et al. 2005) and the *XMM-Newton* Reflection Grating Spectrometer (RGS) (Branduardi-Raymont et al. 2001). The analysis of the soft X-ray spectrum in the long *XMM-Newton* observation (Turner et al. 2003, 2004) confirmed the presence of the dusty warm absorber.

The analysis of the *XMM-Newton* and *Chandra* spectra shows that the X-ray continuum emission of MCG -6-30-15 is highly variable on short time scales (e.g. Vaughan et al. 2003, Vaughan & Fabian 2004, Reynolds et al. 2004, McHardy et al. 2005). The variability in this object has been explained as the product of two components, a highly variable Power Law Component (PLC), with a constant slope, and a less variable Reflection Dominated Component (RDC). The latter includes the relativistic Fe K$\alpha$ line and is produced in the inner regions of the accretion disk (Shih et al. 2002, Fabian & Vaughan 2003, Taylor et al. 2003, Miniutti et al. 2007, Parker et al. 2014, Marinucci et al. 2014). If the PLC drives the emission of the Fe K$\alpha$ fluorescence line, the changes in the Fe line flux should be correlated with the variations of the PLC. However, several works found that the PLC and the RDC are anti-correlated in this source (Iwasawa et al. 1996, 1999, Reynolds 2000, Vaughan & Edelson 2001, Shih et al. 2002, Matsumoto et al. 2003). This unusual relation can be explained taking into account light bending effects in the vicinity of the black hole (Fabian & Vaughan 2003, Miniutti et al. 2003, Miniutti & Fabian 2004). Miniutti & Fabian (2004) proposed a model which interprets the effects of gravitational light bending on the emission of both the primary X-ray continuum and the reflection spectrum from the accretion disk. We briefly present this model in Section 5.4.2.

### NGC 4051

NGC 4051 is a bright Narrow Line Seyfert 1 galaxy (Komossa & Meerschweinchen 2000). Its X-ray flux and spectral shape exhibit large amplitude and rapid variability on both short (< day) and long (years) timescales (e.g. Lawrence et al. 1987, Papadakis & Lawrence 1995, Guainazzi et al. 1998, Green et al. 1999, Uttley et al. 1999, McHardy et al. 2004, Uttley et al. 2004, Ponti et al. 2006, Terashima et al. 2009, Vaughan et al. 2011). When the source is bright, the spectrum is characterized by a power law component, Fe K$\alpha$ emission, and a reflection component, together with a soft excess and ionized absorber (Pounds et al. 2004). When the source is observed with a lower flux, the spectrum above 2 keV appears to be flatter and a broad residual around 6.4 keV is observed (Uttley et al. 2004, Pounds et al. 2004, Ponti et al. 2006, Gallo 2006). Different interpretations have been proposed in order to explain this feature: a relativistic Fe K$\alpha$ line (Uttley et al. 2004), a combination of relativistically broadened ionized reflection and an Fe K$\alpha$ line produced from distant, neutral material (Ponti et al. 2006), or the result of partial covering of the primary continuum by a weakly ionized absorber (Pounds et al. 2004). When the source was observed in a very low flux epoch, the Fe K line flux appeared to be anti-correlated with the variations of the primary emission (Guainazzi et al. 1998). The two-component model invoked for MCG -6-30-15 can also describe this behaviour in NGC 4051. This scenario consists of one soft highly variable component and a hard constant component (Ponti et al. 2006). The spectral variability within and between the two *XMM-Newton* observations (2001 and 2002) was explained considering the power law of the primary continuum as the variable component. The constant component was associated with a combination of ionized and relativistically broadened reflection and neutral reflection from distant material. Also in this case, the observational evidences can be described by the gravitational light bending model, which we present in the next Section.

### 5.4.2 Light Bending Model

As presented in the previous Sections, the light bending model was invoked in order to interpret the unusual scenario revealed in the analysis of the *XMM-Newton* observation of MCG -6-30-15 (Miniutti & Fabian 2004). This model describes in detail the effects of the gravitational light bending suffered by the photons emitted by the corona close to the BH. The model explains how the gravitational light bending imposes variability on both the continuum and the relativistic Fe K$\alpha$ emission line (Martocchia et al. 2002, Fabian & Vaughan 2003).

This model assumes a maximally spinning Kerr black hole with spin parameter of a = 0.998. The geometrically thin accretion disk, which is lying on the black hole equatorial plane, is extending down to the last stable orbit of $r_{ms} = 1.24$ $\mathrm{r}_g$, as expected in the Kerr metric. The gravitational light bending effect is important in the near vicinity of the black hole. For this reason the inner radius, and consequently the spin of the black hole, is a fundamental parameter for this model. The primary source is assumed to be compact, with a constant intrinsic luminosity, and placed at a height $h_s$ of a few gravitational radii above the black hole and at $2r_g$ from the BH rotating axis. The variability of the primary X-ray continuum is assumed to be only related to variations of the height of the corona above the black hole itself. A fraction of the X-ray photons emitted from the corona reaches the observer at infinity and contributes to the direct continuum which is detected as the power law in the spectra (PLC). The remaining radiation interacts with the accretion disk and is reprocessed as presented in Section 1.4 and contributes to the reflection-dominated component (RDC).

When the corona is placed close to the BH, the effects of the light bending break the correlation between the emission of the primary continuum and the reflection component. Indeed, if the source height is small (of the order of a few gravitational radii) a large fraction of the emitted photons, in particular more than half, is bent onto the accretion disk because of the strong gravitational field of the BH. The result is an enhancement of the illuminating continuum on the accretion disk and a decrease of the PLC detected by the observer. In this case the spectrum will be reflection-dominated. When the height of the primary source increases, the effects of the gravitational light bending are reduced and the PLC increases. Finally, in the case of a large height, the effects of the light bending

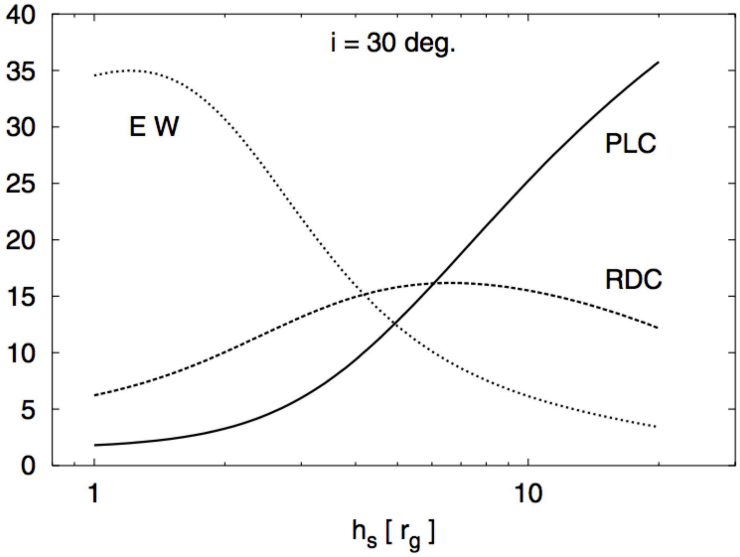

Figure 5.1: The EW of the Fe line, PLC and RDC as a function of the height of the primary source on the accretion disk assuming an inclination of 30°. The RDC is represented by the flux of the relativistic Fe line and the height of the source varies between 1 and 20 $r_g$. The variability is assumed to be due only to the gravitational light bending (Miniutti & Fabian 2004).

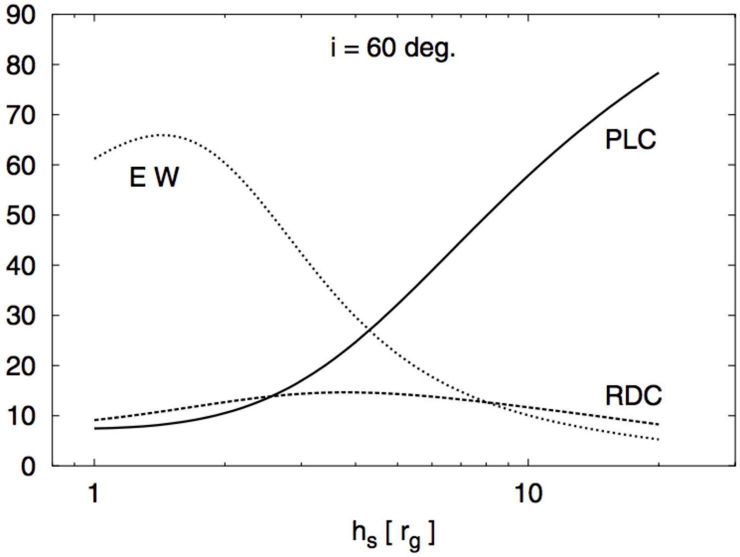

Figure 5.2: The EW of the Fe line, PLC and RDC as a function of the height of the primary source on the accretion disk assuming an inclination of 60°. The RDC is represented by the flux of the relativistic Fe line and the height of the source varies between 1 and 20 $r_g$. The variability is assumed to be due only to the gravitational light bending (Miniutti & Fabian 2004).

become less significant.

Figure 5.1 and 5.2 show the equivalent width of the relativistic line, the PLC flux and the Fe line flux (RDC) as a function of the corona height in the 1-20 $r_g$ range (Miniutti & Fabian 2004), for inclination angles of the accretion disk of 30° and 60°, respectively. The units in the plots are arbitrary. The PLC is well correlated with the increase of the height of the corona showing large variations in flux, while the RDC varies with smaller amplitude. In particular, in the case of an inclination angle of 30°, the PLC varies by a factor of 20 when the source height moves from 1 to 20 $\mathrm{r}_g$, while the RDC varies at most by a factor of 2.6. For an inclination angle of 60°, the variation for the PLC is a factor of 10.5 and only 1.8 for the RDC. The EW of the relativistic Fe line is almost anti-correlated with the height $h_s$ and with the direct continuum. However, for very low flux, the EW appears to be almost constant.

From these plots, it is possible to determine a relationship between the Fe K$\alpha$ flux (i.e. RDC) and the direct continuum observed at infinity (the PLC). This is presented in Figure 5.3 and 5.4 for inclination angles of 30° and 60°, respectively (Miniutti & Fabian 2004). Three regimes can be identified in which the behaviour of these two components is clearly different. They are labelled as I, II and III in the plots. When the gravitational light bending effects are taken into account, the flux of the relativistic Fe K$\alpha$ emission line (i.e. RDC) is not expected to linearly follow and respond to the observed PLC variations anymore. Direct correlation is only seen in Regime I, when the source is located above the disk with a height between 3-4 $\mathrm{r}_g$. The Fe line EW appears to be almost constant in this regime. Regime II corresponds to heights of the primary source between 4 and 13 $\mathrm{r}_g$. The broad Fe line varies less than 10 per cent, while the PLC has variations by a factor of $\sim 4$, as shown in Figure 5.3 and 5.4. The EW of the relativistic Fe line is anti-correlated with the PLC (see Figure 5.1 and 5.2) and therefore the variations of the Fe line flux are difficult to detect. Finally, in Regime III the effects of the light bending are less important resulting in higher PLC flux at infinity detected by the observer. The Fe line flux is anti-correlated with the direct continuum and the EW decreases.

One of the main observational evidences of the effects of the light bending on the reflection spectrum is the anti-correlation of the EW of the broad Fe line with respect to the direct continuum. This relation has been observed in a selection of AGN observed with *Rossi X-ray Timing explorer (RXTE)* by Papadakis et al. (2002). The only exception could appear when the object has low flux. In this case, the EW is almost constant. Moreover, the RDC is not necessary correlated with the EW itself. In fact, only regime III is characterized by a positive correlation between these two components.

In Figure 5.5, the reflection fraction R is plotted as a function of the source height above the accretion disk with an inclination of 30° (Miniutti & Fabian 2004). This parameter is defined as the ratio between the solid angle subtended by the primary source at the disk ($\Omega_{disk}$) and at infinity ($\Omega_\infty$). The solid line corresponds to a source placed in the disc axis, while the dashed line to a co-rotating primary source at 2 $\mathrm{r}_g$ from the BH axis. When the height is large, this parameter reaches the asymptotic value of R = 1. This is consistent with the standard picture where half of the photons emitted by the primary source reaches the observer at infinity while the other half illuminates the disk. However, when the height

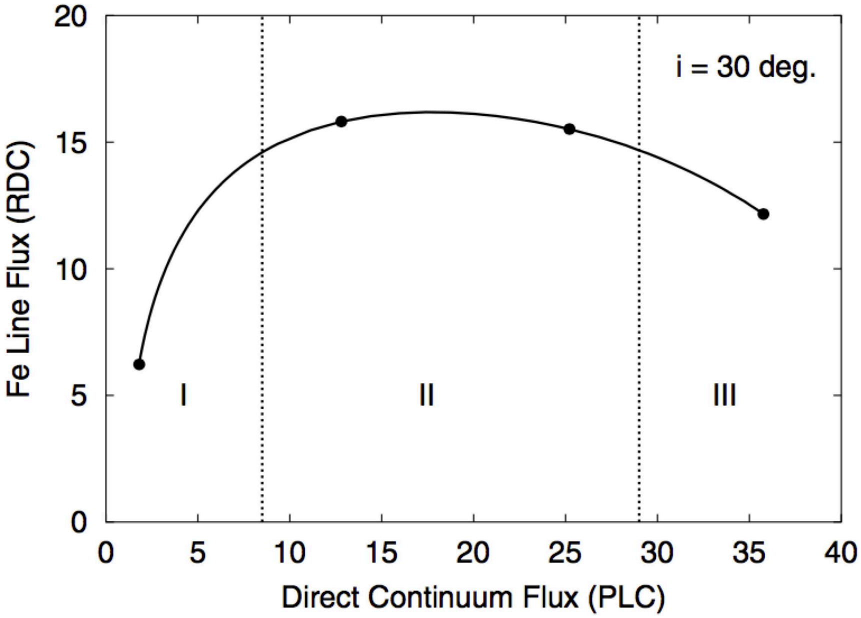

Figure 5.3: The Fe line flux as a function of the direct continuum for an inclination angle of 30°. The solid points in the plot present reference values of the source height $h_s$ of 1.5, 10 and 20 $r_g$. Three different regimes are identified as regime I, II and III (Miniutti & Fabian 2004).

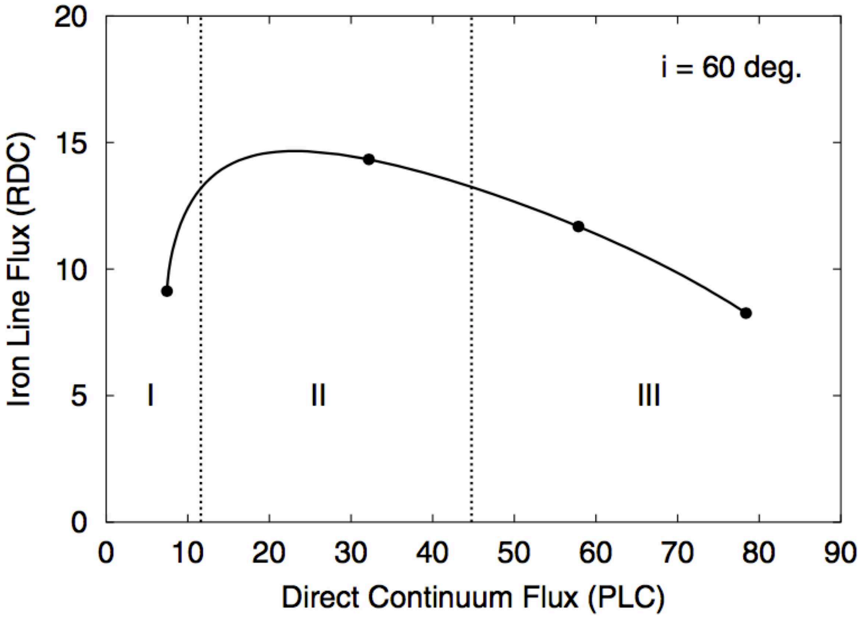

Figure 5.4: The relation between the Fe line flux and the direct continuum observed with and inclination of 60°. The solid points refer to different source height of 1.5, 10 and 20 $r_g$. Three regimes are identified. Miniutti & Fabian 2004).

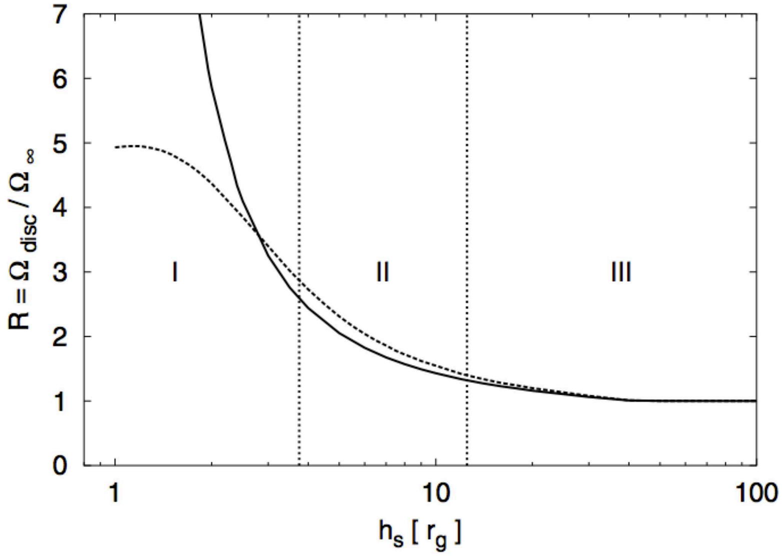

Figure 5.5: The plot presents the reflection fraction R as a function of the primary source height. R = 1 is the asymptote reaches when half of the primary radiation illuminates the disk and the other half reaches the observer at infinity. The solid line corresponds to a source placed on the rotation axis, while the dashed line to a corotating source at 2 $r_g$ form the axis. Three different regimes for an inclination angle of 30° are shown and the variations of R are associated only to the light bending effects (Miniutti & Fabian 2004).

decreases, the effects of gravitational light bending become important and the photons are preferentially bent towards the accretion disk. The result is a dramatical increase of the value of R, as shown in Figure 5.5. In particular, in Regime II the reflection fraction reaches the value of $\sim 2$.

In the next Section, we directly tested the presence of light bending effects in the *NuSTAR* spectra of MCG -6-30-15 and NGC 4051.

### 5.4.3 Data Analysis

Figure 5.6 and 5.7 show the *NuSTAR* data-to-model ratios for MCG -6-30-15 and NGC 4051, respectively, in the 3 to 79 keV energy band for models of increasing complexity from top to bottom. The observations are presented in temporal order for both sources. The upper panels show the data-to-model ratio when only a cut-off power law is included. Important residuals are present for all the observations around 6.4 keV and above 10 keV. The former could be due to a blend of narrow and broad Fe K$\alpha$ emission lines, while the latter could be associated with the reflection continuum at high energies (i.e. the Compton hump). The middle panels show the data-to-model ratios when a narrow gaussian component is included in the previous model. This component well reproduces the core of the Fe K$\alpha$ line, presumably emitted from distant material. However, residuals around 6.4 keV and above 10 keV are still present in all the observations of both sources.

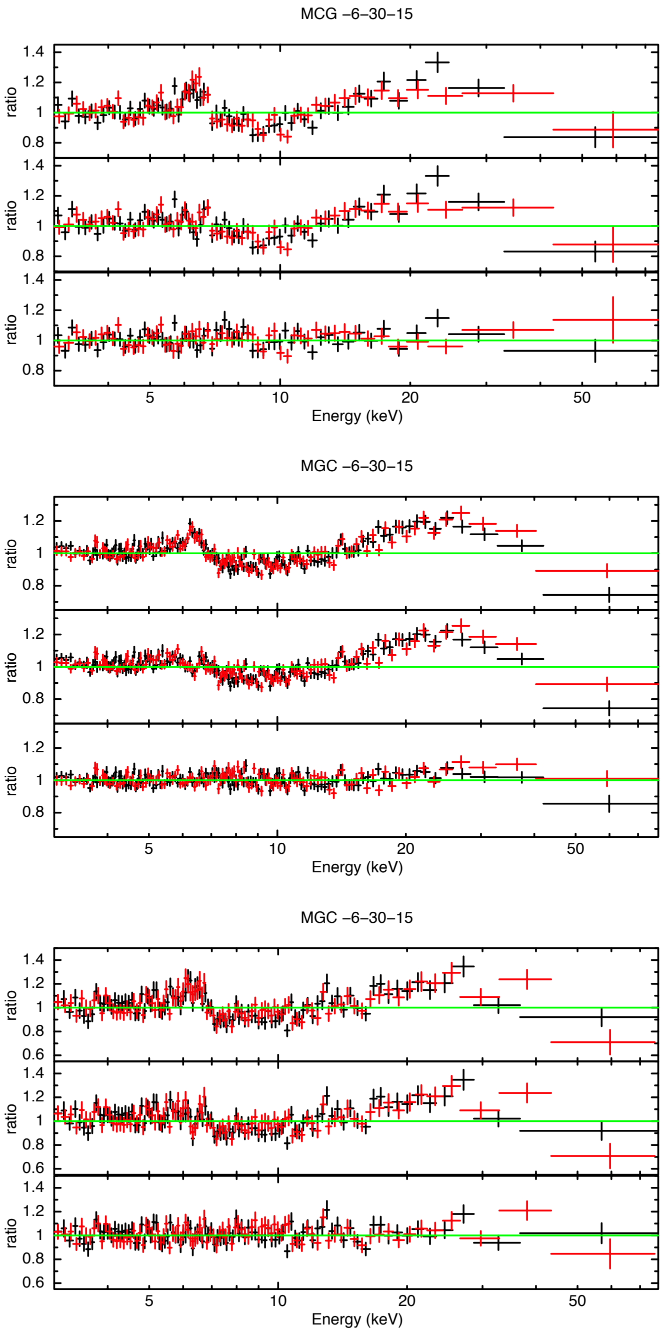

Figure 5.6: We present the *NuSTAR* data to model ratio in the 3 to 79 keV energy band for MCG -6-30-15. The top panels show a model which includes a cut-off power law. The middle panels show the residuals when a narrow gaussian component is included in the previous model in order to fit the narrow Fe K$\alpha$ line. The bottom panels present the data to model ratios when the Relativistic Relline model is applied to the spectra. The observations are presented in temporal order.

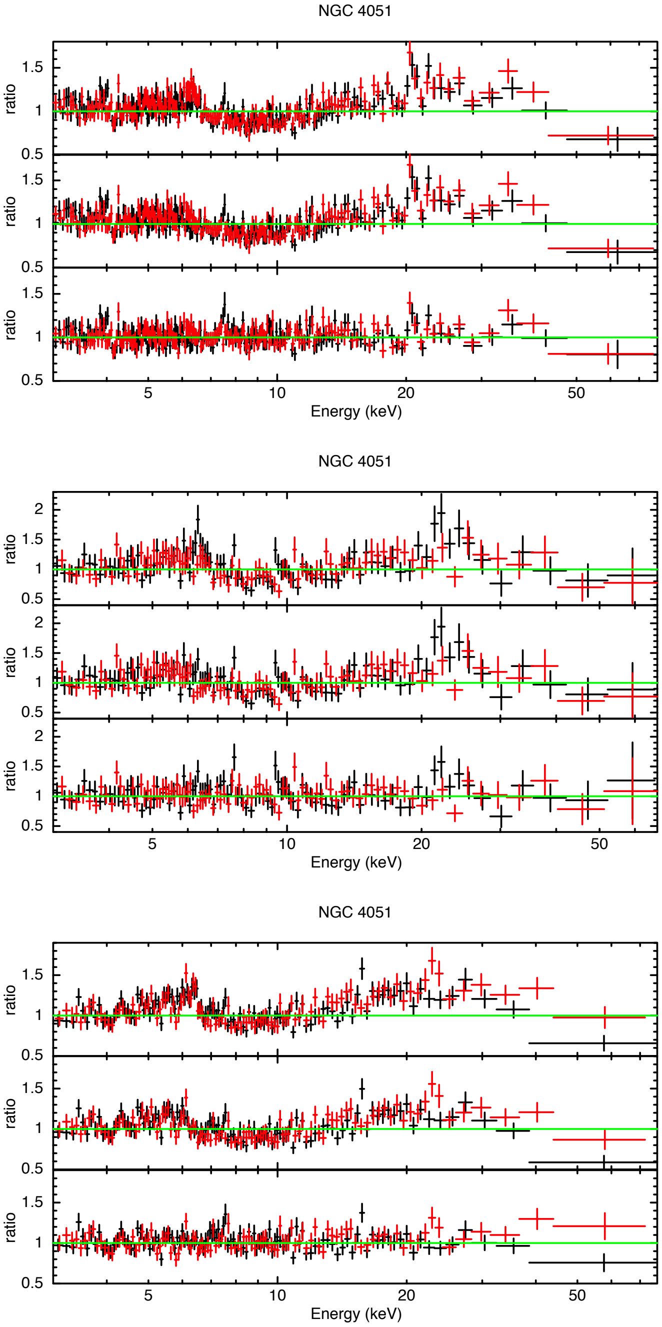

Figure 5.7: We present the *NuSTAR* data to model ratio in the 3 to 79 keV energy band for NGC 4051. The top panels show a model which includes a cut-off power law. The middle panels show the residuals when a narrow gaussian component is included in the previous model in order to fit the narrow Fe K$\alpha$ line. The bottom panels present the data to model ratios when the Relativistic Relline model is applied to the spectra. The observations are presented in temporal order.

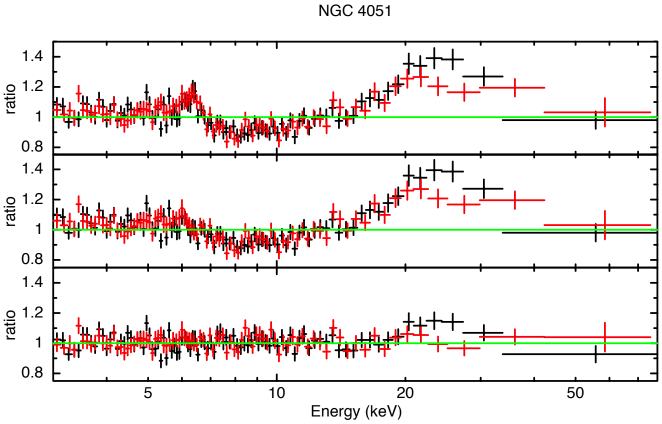

Figure 5.7: (Continued)

In order to model these residuals and to test whether the gravitational light bending is important, we applied to the *NuSTAR* data the Relativistic Relline Model: *pexrav+zgauss+relline*. This model includes a cut-off power law together with a reflection continuum (*pexrav*), a gaussian component to fit the narrow Fe K$\alpha$ line (*zgauss*) and a relativistic line component (*relline*). The energies of both the narrow and broad Fe K$\alpha$ line were fixed to 6.4 keV, while the width of the gaussian was fixed to $\sigma = 1$ eV. We assumed highly spinning black holes for both sources, fixing the spin parameter to 0.998 in the *relline* model.

In the case of MCG -6-30-15, we assume a broken power law parametrization for the emissivity profile of the disk as found by Fabian et al. (2002) and Vaughan & Fabian (2004). However due to the limited energy range of *NuSTAR* data at low energies (E $>$ 3 keV) and the broadness of the line profile which would extend below this limit, we cannot robustly constrain both emissivity indices and the break radius. Therefore we fix in our fits $q_{in}$ to 7, as derived by Fabian et al. (2002) and Vaughan & Fabian (2004) from a long *XMM-Newton* ($\sim$ 320 ks) observation which benefits from data at lower energies and a superior depth (see for details Section 5.4.1). The other parameters, the inner radius, the inclination of the disk, the break radius and the second emissivity index $q_{out}$ were left free to vary in our fit. For MCG -6-30-15, we initially allowed the Fe abundance to be free in the Relativistic Relline model. The analysis of the long *XMM-Newton* observation showed that the data were consistent with the Fe abundance being three times higher than the solar value (Fabian et al. 2002). We do not find a significant improvement in the fits and therefore, we fixed this parameter to unity.

In the case of NGC 4051, a simple power law was assumed for the emissivity profile of the disk, as in previous *XMM-Newton* observations was not possible to discriminate between a broken and a simple power law (Ponti et al. 2006). We therefore assumed $q_{out} = q_{in}$ for the emissivity indices, leaving the latter as a free parameter in the fits. The free parameters for this fit are the inner radius, the inclination of the disk and $q_{in}$. Also for this object, we fixed the Fe abundance to the solar value, because no improvement in the fits was found when leaving this parameter free.

The data-to-model ratios for each observation for the Relativistic Relline model are presented in the bottom panels of Figure 5.6 and 5.7 for MCG -6-30-15 and NGC 4051, respectively. This model reproduces the residuals around the relativistic Fe line at 6.4 keV and the Compton hump above 10 keV (see middle panels).

We present the best-fit parameters of this model in Table 5.3. Both sources exhibit strong reflection compared to the primary continuum flux detected ($R = 1.66$ for MCG -6-30-15 and $R = 2.67$ for NGC 4051), with values of $R$ slightly lower than those presented in Table 5.2 when the relativistic Fe K$\alpha$ line was not included in the model ($R = 1.91$ for MCG -6-30-15 and $R = 3.47$ for NGC 4051). This emission is produced in the inner regions of the accretion disk ($R_{in} < 5\ r_g$) around a maximally rotating Kerr black hole. The measured equivalent widths of the relativistic Fe component ($EW = 264$ eV in the case of MCG -6-30-15 and $EW = 258$ eV for NGC 4051) are also consistent with this scenario, and are greater than the value of ~100 eV, expected if light bending or differential variability effects are not important (George & Fabian 1991). The parameters associated with the relativistic Fe line component and with the reflection continuum indicate strong reflection compared to the standard picture (see Section 1.4 for more details). These results could be explained by the presence of gravitational light bending as presented above (see Section 5.4.2).

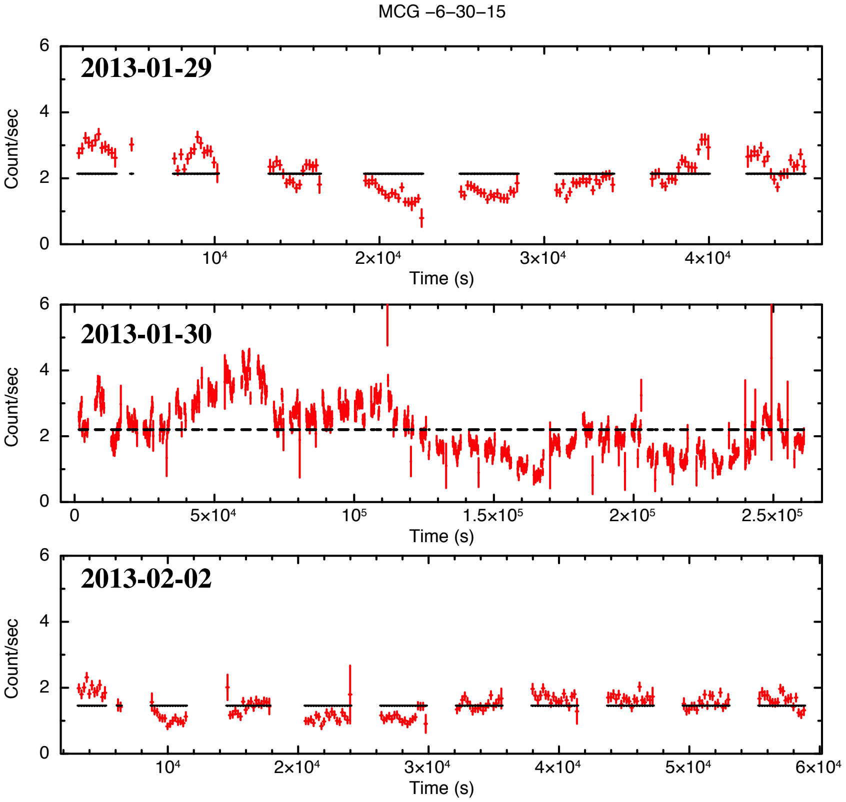

Figure 5.8: We present the light curves of each observation for MCG -6-30-15 in temporal order in the 3-10 keV energy band. We combined the light curves from the FPMA and FPMB instruments and the bins size is 200 s.

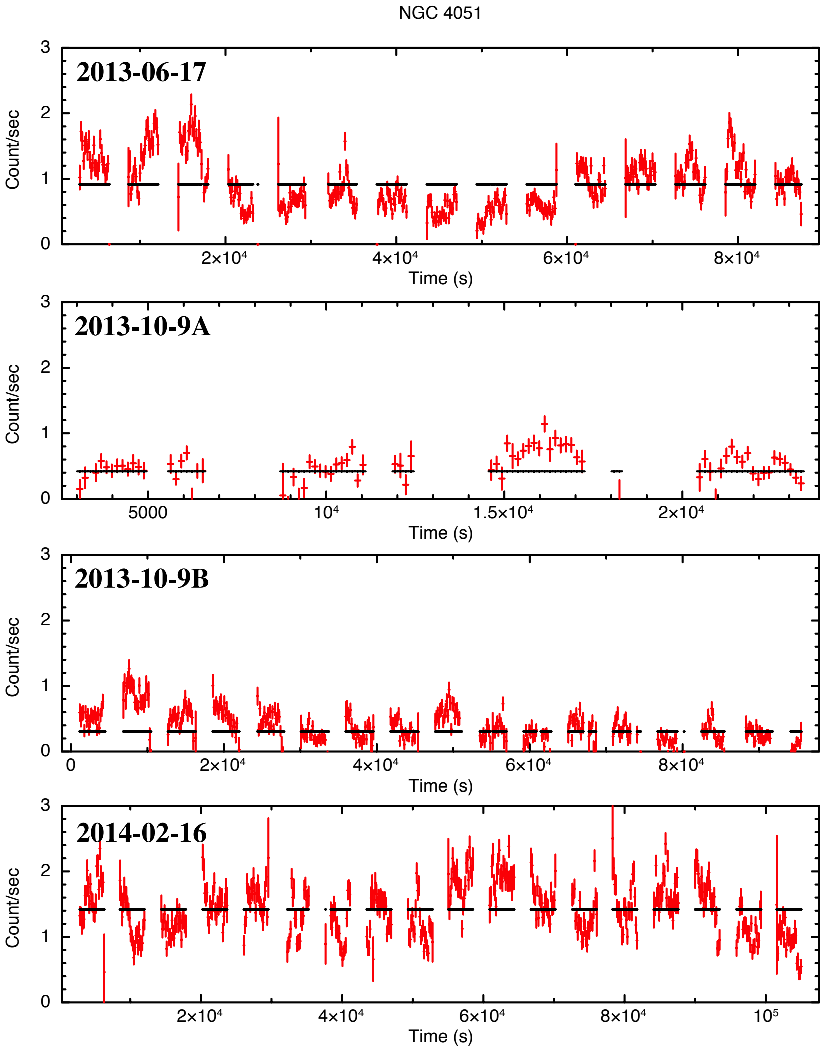

Figure 5.9: We present the light curves of each observation for NGC 4051 in temporal order in the 3-10 keV energy band. We combined the light curves from the FPMA and FPMB instruments and the bins size is 150 s.

Figure 5.8 and 5.9 show the light curves in the 3 to 10 keV energy band for MCG -6-30-15 and NGC 4051, respectively. The black line in the light curves shows the mean count rate (ct/s) for each observation. The light curves are background subtracted and the data from the FPMA and FPMB instruments are co-added. The bins for the light curves are 200 s for MCG -6-30-15 and 150 s for NGC 4051. MCG -6-30-15 shows important variability of the X-ray emission within each observation, with variation factors up to 4. The average count rates in each light curve are 2.14, 2.20 and 1.46, respectively, showing variability of a factor of 1.5 between the observations. An almost constant X-ray emission is detected in the second and third observations of NGC 4051, while a variation of a factor of 2 is present in the first and fourth observations. The average count rates in these observations

| Object | Observation | $\Gamma$ | $E_c$ | R | $A_{Fe}$ | $\theta$ | Norm | Flux$_{K\alpha}$ | EW$_{K\alpha}$ | Flux$_{3-10keV}$ | $r_{in}$ | $\theta_{disk}$ | q$_{in}$ | q$_{out}$ | $r_{break}$ | EW$_{Relline}$ | Constant | $\chi^2$/d.o.f. |
|---|---|---|---|---|---|---|---|---|---|---|---|---|---|---|---|---|---|---|
| MCG -6-30-15 | 2013-01-29 | $2.18^{+0.06}_{-0.05}$ | $129^{+68}_{-35}$ | $1.98^{+0.49}_{-0.40}$ | 1 fixed | 60° | $2.20^{+0.17}_{-0.14}$ | $< 2.22$ | $< 42$ | $3.55^{+0.01}_{-0.01}$ | $5.35^{+10.66}_{-1.37}$ | $34^{+4}_{-4}$ | 7 fixed | $3.34^{+1.25}_{-1.12}$ | 4 fixed | $253^{+80}_{-80}$ | $1.02^{+0.01}_{-0.01}$ | 611.72/649 |
| | 2013-01-30 | $2.10^{+0.02}_{-0.02}$ | $174^{+44}_{-30}$ | $1.33^{+0.14}_{-0.13}$ | 1 fixed | 60° | $2.04^{+0.06}_{-0.06}$ | $1.85^{+0.49}_{-0.49}$ | $36^{+10}_{-10}$ | $3.65^{+0.01}_{-0.01}$ | $2.95^{+0.84}_{-0.42}$ | $33^{+4}_{-3}$ | 7 fixed | $3.03^{+0.34}_{-0.30}$ | $< 4.35$ | $228^{+39}_{-39}$ | $1.03^{+0.01}_{-0.01}$ | 1358.97/1286 |
| | 2013-02-02 | $1.99^{+0.06}_{-0.03}$ | $172^{+122}_{-53}$ | $1.68^{+0.42}_{-0.34}$ | 1 fixed | 60° | $1.08^{+0.09}_{-0.06}$ | $< 0.91$ | $< 24$ | $2.41^{+0.01}_{-0.01}$ | $< 5.54$ r$_g$ | $35^{+3}_{-4}$ | 7 fixed | $4.65^{+2.05}_{-1.40}$ | $< 4.02$ | $310^{+51}_{-75}$ | $1.03^{+0.02}_{-0.02}$ | 662.07/659 |
| NGC 4051 | 2013-06-17 | $2.12^{+0.07}_{-0.06}$ | $402^{+2324}_{-195}$ | $2.72^{+0.65}_{-0.52}$ | 1 fixed | 60° | $0.81^{+0.08}_{-0.07}$ | $1.57^{+0.45}_{-0.45}$ | $75^{+21}_{-21}$ | $1.55^{+0.01}_{-0.01}$ | $< 5.36$ | $19^{+7}_{-7}$ | $3.72^{+0.92}_{-0.73}$ | =q$_1$ | 15 r$_g$ | $156^{+48}_{-48}$ | $1.05^{+0.02}_{-0.02}$ | 698.33/650 |
| | 2013-10-9A | $1.98^{+0.24}_{-0.18}$ | $157^{+2183}_{-80}$ | $3.46^{+2.88}_{-1.47}$ | 1 fixed | 60° | $0.43^{+0.01}_{-0.01}$ | $2.05^{+0.86}_{-0.86}$ | $135^{+57}_{-57}$ | $1.11^{+0.01}_{-0.01}$ | $<5.44$ | $< 30°$ | $4.45^{+1.81}_{-1.16}$ | =q$_1$ | 15 r$_g$ | $373^{+145}_{-145}$ | $1.07^{+0.04}_{-0.04}$ | 175.59/177 |
| | 2013-10-9B | $1.73^{+0.09}_{-0.08}$ | $97^{+39}_{-23}$ | $2.27^{+0.69}_{-0.53}$ | 1 fixed | 60° | $0.23^{+0.03}_{-0.02}$ | $1.05^{+0.35}_{-0.35}$ | $85^{+29}_{-29}$ | $0.84^{+0.02}_{-0.02}$ | $<4.20$ | $< 23°$ | $3.50^{+0.73}_{-0.59}$ | =q$_1$ | 15 r$_g$ | $370^{+79}_{-78}$ | $1.04^{+0.02}_{-0.02}$ | 621.68/550 |
| | 2014-02-16 | $2.23^{+0.04}_{-0.05}$ | $> 489$ | $2.21^{+0.42}_{-0.36}$ | 1 fixed | 60° | $1.55^{+0.01}_{-0.01}$ | $1.62^{+0.53}_{-0.53}$ | $51^{+17}_{-17}$ | $2.38^{0.01}_{-0.01}$ | $<4.37$ | $< 25°$ | $3.45^{+1.31}_{-0.92}$ | =q$_1$ | 15 r$_g$ | $133^{+41}_{-41}$ | $1.01^{+0.01}_{-0.01}$ | 812.06/778 |

Table 5.3: Best Fit parameters of the Relativistic Relline model. The high energy cut-off is expressed in keV, while the equivalent width in eV. The power law normalization is in units of $10^{-2}$ photons keV$^{-1}$ cm $^{-2}$ and the continuum flux in the 3 to 10 keV energy band is in $10^{-11}$ erg s$^{-1}$ cm$^{-2}$. The flux of the Fe K$\alpha$ line is quoted in $10^{-5}$ erg s$^{-1}$ cm$^{-2}$. The inner radius and the break radius are in units of $R_g$.

| Object | Observation | $\Gamma$ | $E_c$ | R$_{Narr}$ | R$_{broad}$ | $A_{Fe}$ | Norm | Flux$_{3-10keV}$ | $r_{in}$ | $\theta$ | q$_{in}$ | q$_{out}$ | $r_{break}$ | Constant | $\chi^2$/d.o.f. |
|---|---|---|---|---|---|---|---|---|---|---|---|---|---|---|---|
| MCG -6-30-15 | 2013-01-29 | $2.23^{+0.06}_{-0.05}$ | $162^{+93}_{-45}$ | $0.15^{+1.09}_{-0.31}$ | $1.72^{+0.46}_{-0.30}$ | 1 fixed | $2.36^{+0.16}_{-0.14}$ | $3.55^{+0.01}_{-0.01}$ | $2.89^{+9.92}_{-0.43}$ | $37^{+5}_{-5}$ | 7 fixed | $2.15^{+0.37}_{-0.33}$ | $< 4.90$ | $1.02^{+0.01}_{-0.01}$ | 609.22/649 |
| | 2013-01-30 | $2.15^{+0.02}_{-0.02}$ | $232^{+67}_{-43}$ | $0.17^{+0.12}_{-0.12}$ | $1.05^{+0.16}_{-0.16}$ | 1 fixed | $2.21^{+0.05}_{-0.05}$ | $3.66^{+0.01}_{-0.01}$ | $3.44^{+3.06}_{-0.63}$ | $35^{+2}_{-5}$ | 7 fixed | $2.11^{+0.19}_{-0.20}$ | $< 5.53$ | $1.03^{+0.01}_{-0.01}$ | 1379.72/1287 |
| | 2013-02-02 | $2.05^{+0.05}_{-0.05}$ | $233^{+64}_{-72}$ | $0.001^{+0.53}_{-0.26}$ | $1.50^{+0.34}_{-0.09}$ | 1 fixed | $1.19^{+0.04}_{-0.04}$ | $2.41^{+0.01}_{-0.01}$ | $3.07^{+2.59}_{-0.52}$ | $32^{+5}_{-6}$ | 7 fixed | $2.09^{+0.27}_{-0.19}$ | $< 5.00$ | $1.03^{+0.02}_{-0.02}$ | 676.46/660 |
| NGC 4051 | 2013-06-17 | $2.12^{+0.04}_{-0.04}$ | $> 370$ | $0.37^{+0.26}_{-0.26}$ | $1.59^{+0.34}_{-0.39}$ | 1 fixed | $0.82^{+0.04}_{-0.04}$ | $1.55^{+0.01}_{-0.01}$ | $4.47^{+1.77}_{-1.04}$ | $21^{+5}_{-4}$ | $2.64^{+0.48}_{-0.37}$ | =q$_1$ | 15 fixed | $1.05^{+0.02}_{-0.02}$ | 705.68/651 |
| | 2013-10-9A | $2.14^{+0.12}_{-0.12}$ | $> 172$ | $0.86^{+0.75}_{-0.78}$ | $2.75^{+1.19}_{-1.60}$ | 1 fixed | $0.54^{+0.06}_{-0.07}$ | $1.11^{+0.01}_{-0.01}$ | $4.53^{+5.20}_{-1.36}$ | $24^{+9}_{-9}$ | $2.94^{+1.35}_{-0.71}$ | =q$_1$ | 15 fixed | $1.07^{+0.04}_{-0.04}$ | 181.58/178 |
| | 2013-10-9B | $1.87^{+0.07}_{-0.07}$ | $162^{+111}_{-50}$ | $0.26^{+1.75}_{-0.33}$ | $1.86^{+0.45}_{-0.52}$ | 1 fixed | $0.29^{+0.02}_{-0.02}$ | $0.84^{+0.01}_{-0.01}$ | $5.82^{+3.17}_{-1.89}$ | $< 22$ | $2.74^{+0.31}_{-0.30}$ | =q$_1$ | 15 fixed | $1.04^{+0.02}_{-0.02}$ | 631.41/551 |
| | 2014-02-16 | $2.20^{+0.02}_{-0.01}$ | $> 427$ | $0.0001^{+0.38}_{-0.19}$ | $1.53^{+0.26}_{-0.08}$ | 1fixed | $1.50^{+0.01}_{-0.07}$ | $2.38^{+0.01}_{-0.01}$ | $4.00^{1.68}_{-1.04}$ | $23^{+5}_{-5}$ | $2.31^{+0.20}_{-0.15}$ | =q$_1$ | 15 fixed | $1.01^{+0.01}_{-0.01}$ | 826.29/779 |

Table 5.4: Best fit parameters of the Relativistic Pexmon Model. The high energy cut-off is expressed in keV, while the equivalent width in eV. The power law normalization is in units of $10^{-2}$ photons keV$^{-1}$ cm $^{-2}$ and the continuum flux in the 3 to 10 keV energy band is in $10^{-11}$ erg s$^{-1}$ cm$^{-2}$. The flux of the Fe K$\alpha$ line is quoted in $10^{-5}$ erg s$^{-1}$ cm$^{-2}$. The inner radius and the break radius are in units of $R_g$.

are 0.92, 0.43, 0.31 and 1.42, respectively. Also for this source, the variability of the X-ray emission detected for this source between the observations is important. From the light curves it is possible to note that the sources analyzed are highly variable from time scales of ∼ 200 s (bin size), within each single observation, to time scales of ∼5 days for MCG -6-30-15 and ∼8 months for NGC 4051. The latter correspond to the time scales spaced by the observations.

To further examine the evidence for light bending, we investigate the relation between the power law flux and the quantities associated with the reflection spectrum, namely the reflection fraction, the equivalent width and the flux of the relativistic Fe line. If the primary X-ray source is sufficiently close to the central black hole and thus the light bending effects are important, an anti-correlation between the primary continuum and the reflection component should be detected. Moreover, the one-to-one correlation between the Fe line flux and the power law component is modified. This is presented in Figure 5.1 and Figure 5.3 (Miniutti & Fabian 2004), for an inclination of 30°, appropriate for MCG -6-30-15 and NGC 4051 (Fabian et al. 2002, Vaughan & Fabian 2004, Ponti et al. 2006). As presented in Section 5.4.2, in the light bending model three regimes are identified. In each of them, the behaviour of the EW, PLC and RDC is clearly different, depending on the height of the primary source considered: Regime I corresponds to heights $h_s <$ 2-4 $r_g$, Regime II to a range of $h_s$ between 2-4 $r_g$ and 7-13 $r_g$, while Regime III is associated with heights $>$ 7-13 $r_g$ (see Miniutti & Fabian 2004 for further details).

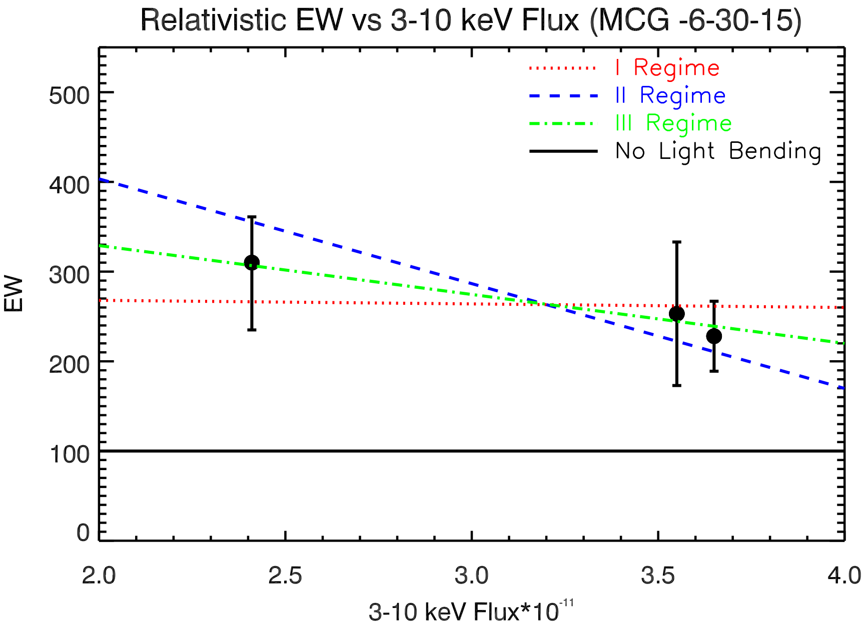

Figure 5.10: Relation between the Equivalent Width (in eV) of the relativistic Fe K$\alpha$ line and the flux of the continuum in the 3-10 keV band (in $10^{-11}$ $erg\ cm^{-2}\ s^{-1}$) for MCG -6-30-15. The coloured lines present the dependence of the Fe line EW on the primary source height expected in the three regimes defined in the light bending model.

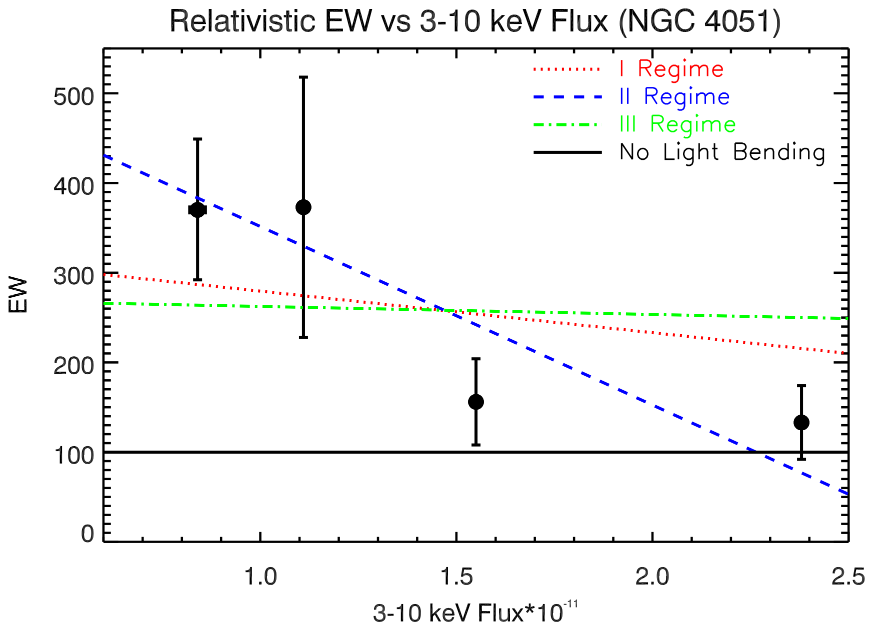

Figure 5.11: Relation between the Equivalent Width (in eV) of the relativistic Fe K$\alpha$ line and the flux of the continuum in the 3-10 keV band (in $10^{-11}$ $erg\ cm^{-2}\ s^{-1}$) for NGC 4051. The coloured lines present the dependence of the Fe line EW on the primary source height expected in the three regimes defined in the light bending model.

In order to test for the presence of light bending effects in MCG -6-30-15 and NGC 4051, we investigated the relation of the continuum flux in the 3-10 keV energy band with both the relativistic line EW and the Fe line flux, comparing our results with the trends expected from the model. As in Miniutti & Fabian (2004), we assumed that the primary X-ray source is located above the black hole and it has constant intrinsic luminosity. The variations in height of the corona above the black hole produce variability in the primary continuum. Therefore, it is possible to directly associate the variations of the flux in the 3-10 keV energy band observed in the spectra with the height of the corona in the source analyzed.

Figure 5.10 and 5.11 show the equivalent width of the relativistic Fe line as a function of the continuum flux in the 3 to 10 keV band for MCG -6-30-15 and NGC 4051, respectively. The equivalent width is expressed in eV and the flux is in $10^{-11}$ $erg\ cm^{-2}\ s^{-1}$. The continuum flux in these sources varies by a factor of 1.5 and 2.8, respectively for MCG -6-30-15 and NGC 4051. Using Figure 5.1, we derived the variation expected in EW for the observed flux changes, for each regime separately.

In Table 5.5, we present the ranges in corona height considered for each regime and source. The red dotted line corresponds to Regime I, the blue dashed to Regime II and the green dash-dot line to Regime III. The black solid line shows the constant value of the EW expected if the corona is placed far from the central black hole where light bending effects are negligible. In this case, the relativistic Fe line flux and the primary X-ray continuum

| Source | Regime I | Regime II | Regime III |
|---|---|---|---|
| MCG -6-30-15 | 1-1.5 | 5-7.5 | 12-17 |
| NGC 4051 | 1-2.8 | 4.5-12 | 12-30 |

Table 5.5: Ranges in corona height considered for each regime and source. The heights are in unit of $r_g$.

will vary with a 1:1 correlation, resulting in a constant EW, with an average value of $\sim$ 100 eV (George & Fabian 1991). The data for both sources are not consistent with this trend. Specifically, the values of the EW for MCG -6-30-15 and NGC 4051 are higher than the expected by a factor of 3 and 4, respectively. For MCG -6-30-15, the plot in Figure 5.10 shows that the dependences expected for each of the three Regimes can reproduce the data, while in the case of NGC 4051, the data are consistent with the source being observed in Regime II (Fig. 5.11).

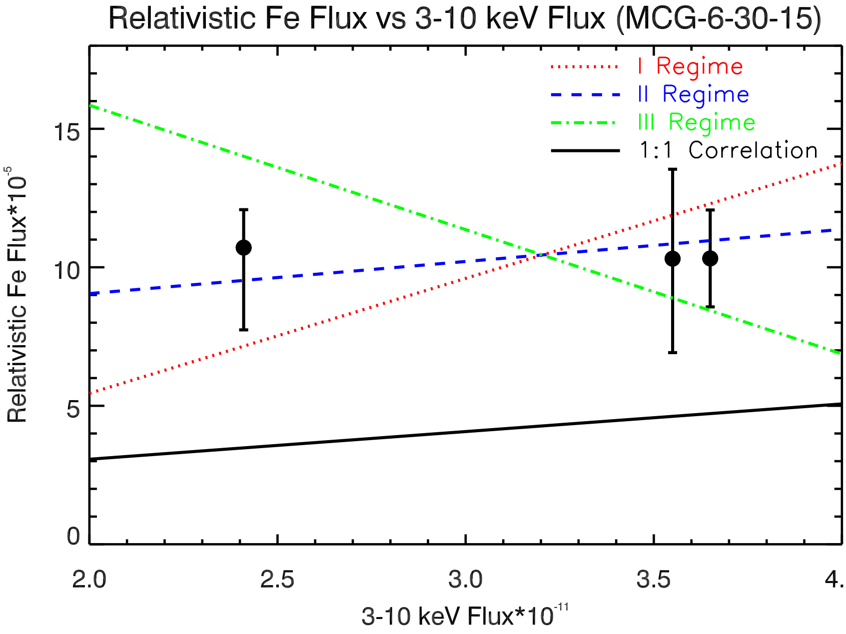

Figure 5.12: The figure presents the relativistic iron K$\alpha$ flux as a function of the primary continuum flux for MCG -6-30-15. The line flux and 3-10 keV flux are expressed in $erg\ cm^{-2}\ s^{-1}$. The coloured lines present the dependence of the relativistic Fe line flux on the primary source height expected in the three regimes as defined from the light bending model. The black line shows the one-to-one correlation expected when light bending effects are negligible.

Figure 5.12 and 5.13 show the relativistic Fe K$\alpha$ flux (in $10^{-5}\ erg\ cm^{-2}\ s^{-1}$) as a function of the continuum flux in the 3 to 10 keV band for MCG -6-30-15 and NGC 4051, respectively. As above, the red dotted line corresponds to the Regime I, the blue dashed to

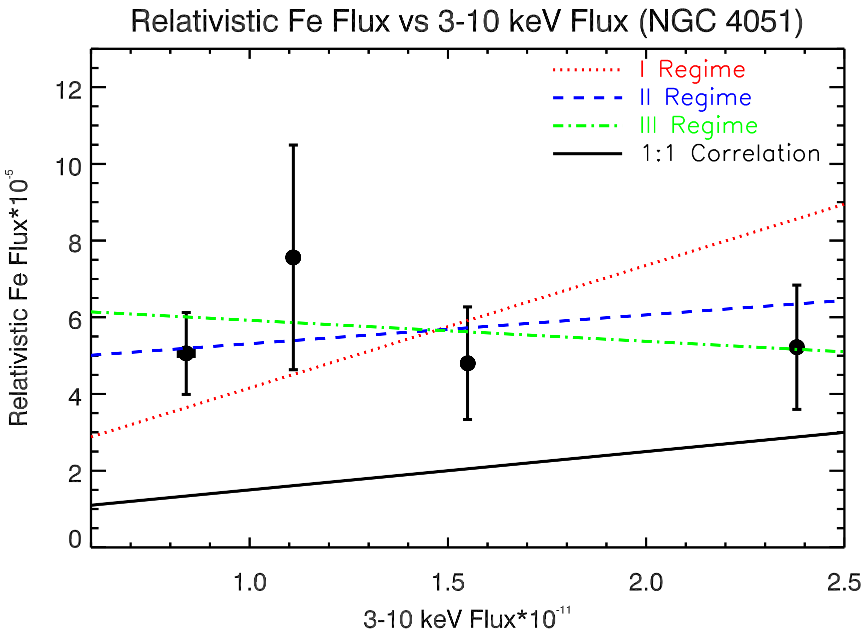

Figure 5.13: The figure presents the relativistic iron K$\alpha$ flux as a function of the primary continuum flux for the source NGC 4051. The line and 3-10 keV flux are expressed in erg cm$^{-2}$ s$^{-1}$. The coloured lines present the dependence of the relativistic Fe line flux on the primary source height expected in the three regimes as defined from the light bending model. The black line shows the one-to-one correlation expected when light bending effects are negligible.

the Regime II, the green dash-dot line to the Regime III and the black solid line corresponds to the one-to-one correlation. It is clear that the data are not consistent with the standard picture, where the Fe line flux is directly linked to the variations of the primary continuum. For both objects, the data are consistent with the relation expected in the Regime II.

The analysis presented so far for MCG -6-30-15 and NGC 4051 shows that the data are consistent with the sources being observed in the Regime II, as defined by Miniutti & Fabian (2004). This regime corresponds to a height of the primary source between 5 and 7.5 $r_g$ in the case of MCG -6-30-15 and between 4.5 and 12 $r_g$ for NGC 4051.

We now seek to further constrain the heights of the corona $h_s$ for these two sources, during the observations considered in this work. To achieve this, we use the relation between the reflection fraction $R_{broad}$ associated with the emission from the accretion disk and $h_s$, as derived in the light bending model (see Figure 5.5 in Section 5.4.2). To measure $R_{broad}$ we fitted the spectra with the Relativistic Pexmon model. This model includes a power law with a high energy cut-off (*cutoffpl* in *xspec*), a narrow *pexmon* component and a second *pexmon* convolved with a *relconv* model. The last two components reproduce the reflection spectra produced from distant material and from the accretion disk. The *relconv* model modifies the spectrum taking into account strong gravity effects present in the vicinity of the black hole in a similar way to the relline model. For both sources, we fixed the inclination of the narrow *pexmon* to 60° and the Fe abundance to the solar value. As for the Relativistic Relline model, we assumed a broken power law for the emissivity profile of MCG -6-30-15 by fixing $q_{in}$ to 7 and letting $q_{out}$ free to vary. In the case of NGC 4051, we assumed a single power law ($q_{out} = q_{in}$). Table 5.4 shows the best fit parameters of this model. The physically self-consistent model allowed us to constrain important parameters of the reflection spectrum. The inner radii of MCG -6-03-15 and NGC 4051 were measured to be $r_{in} = 3.13\ r_g$ and $r_{in} = 4.71\ r_g$, respectively. The inclinations for both sources are consistent with those found when the Relativistic Relline model was applied to the data. The emissivity indices were found to be well constrained but flatter than those measured using the Relativistic Relline model. This trend also appears in the case of the reflection fraction $R$. However, the reflection fraction associated to the emission from the disk remains higher than unity. These results could be explained considering that the Relativistic Pexmon model is reproducing self-consistently the entire reflection spectrum, linking the emission of the relativistic Fe line to that of the Compton hump, while the Relativistic Relline model fits the Fe line and the Compton hump independently. The parameters are more constrained in the first case.

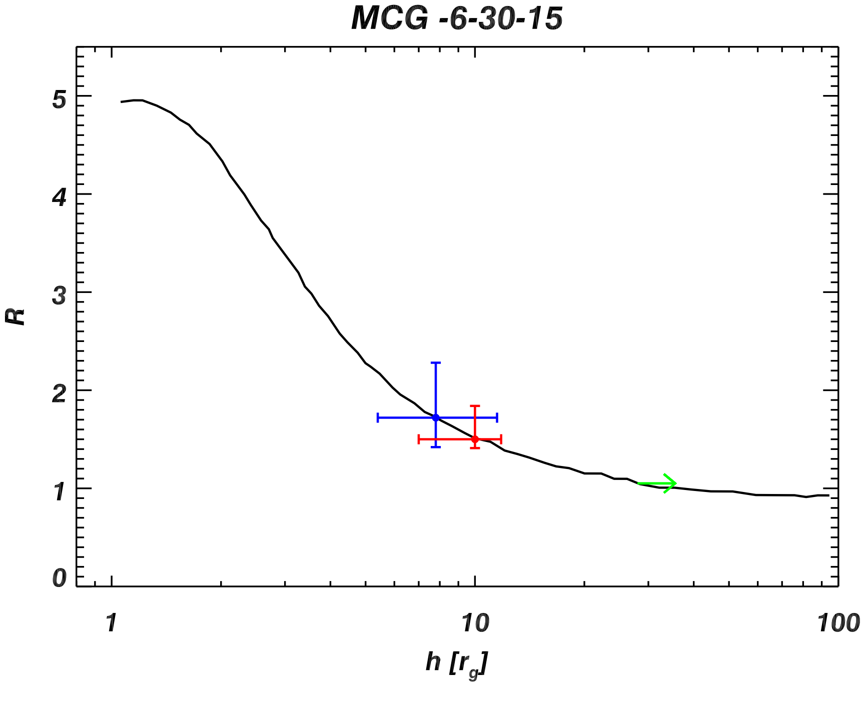

Figure 5.14: The plot shows the expected relation between the reflection fraction and the height of the primary source when light bending effects are present. We plotted for comparison the values of $R_{broad}$ from the fit of the spectra of MCG -6-30-15.

As presented above, both sources show strong reflection from the accretion disk $R_{broad} > 1$. Moreover, a hint of variability of this quantity is detected between the spectra of both objects. In Figure 5.14 and 5.15, we present the theoretical relation of the reflection fraction as a function of the height of the primary source above the black hole for a corotating source

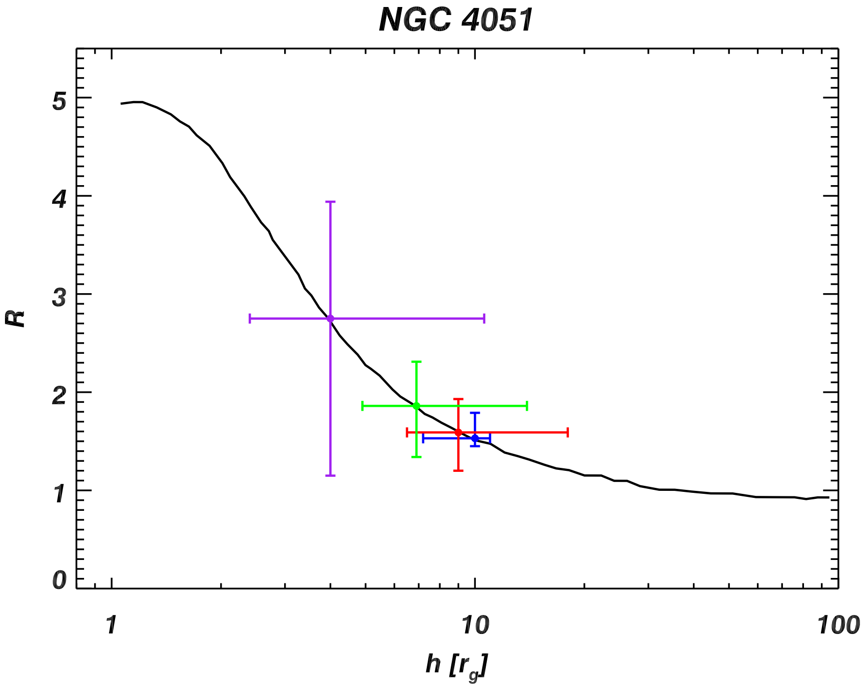

Figure 5.15: The plot shows the expected relation between the reflection fraction and the height of the primary source when light bending effects are present. We plotted for comparison the values of $R_{broad}$ from the fit of the spectra of NGC 4051.

placed at $2r_g$ from the axis (Miniutti & Fabian 2004). Assuming that gravitational light bending is present in MCG -6-30-15 and NGC 4051, the values of the reflection fraction can be turned into an estimate of the height of the primary source. Together with the expected function of $R$, we then over-plotted for comparison the values of the reflection fraction $R_{broad}$ presented in Table 5.4. The uncertainties on the x-axis are calculated from the error bars of the reflection fraction. From this, it was possible to estimate the height of the primary source above the black hole. We found that for MCG -6-30-15 it is in the 5-20 $r_g$ range, while for NGC 4051 in 2.5-20 $r_g$ range.

Another independent test of the presence of light bending, which allows us to measure the height of the corona, comes from the analysis of the simultaneous variations in the power law continuum flux and the reflection fraction $R$. To do so, we used the value of PLC from Figure 5.1 (Miniutti & Fabian 2004) for a given value of the corona height. The variation factor of PLC across two different observations is converted into a variation factor of the corona height for different initial values of $h$ (ranging from 1 to $\sim$ 15 $r_g$). This can be converted into a variation factor of $R$, using the model line in Figure 5.14. By using different variations factors of the PLC ranging within the maximum observed, we constructed the expected trend of the reflection fraction for different ranges of $h$, marked with lines of different colours and labeled accordingly, in Figures 5.16 and 5.17, for MCG -6-30-15 and NGC 4051, respectively. The power law flux in the 3-10 keV energy band is expressed in $10^{-11}$ erg cm$^{-2}$ s$^{-1}$. In order to select the height variation that best describes

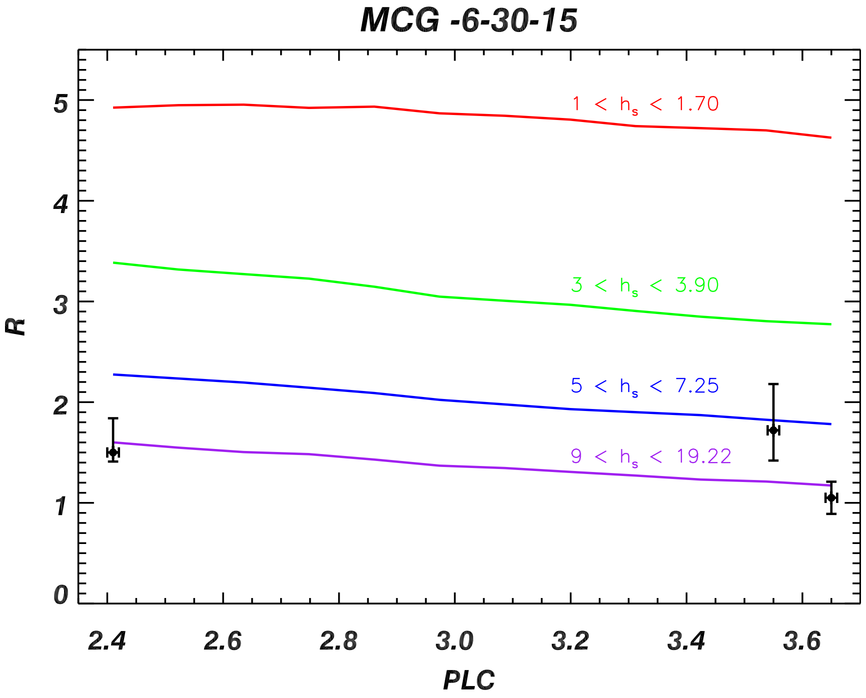

Figure 5.16: We present the relation between the reflection fraction and the power law flux in the 3-10 keV band for MCG -60-30-15. We compared the data (black points) with the relative variations of these quantities expected from the light bending model (coloured lines), for different initial heights values. For each line, we report the corresponding range of $h_s$.

the data points, we perform a $\chi^2$ minimization between the values of the reflection fraction extracted from the light bending model and the observed ones. We find that for MCG -6-30-15 the primary source height varies between 9 and 19 $r_g$, while for NGC 4051 between 5 and 20 $r_g$. These results are fully consistent with what it was found from the direct comparison between the reflection fraction and the heights of the corona for both sources. However, the analysis of the simultaneous variations in power law flux and reflection fraction gives tighter constrains on these measurements.

## 5.5 Discussion

In this chapter, we present the analysis of a sample of Seyfert 1 objects observed with *NuSTAR*. This instrument allows us to optimally study the high energy part of the X-ray spectrum above 10 keV. We choose the sources from the complete sample of Seyfert 1 galaxies analyzed in Nandra et al. (2007), and selected the objects with *NuSTAR* observations available in the archive. The aim of this work is to investigate the relation between the emission of both narrow and relativistic Fe K$\alpha$ lines and the associated reflection continuum above 10 keV.

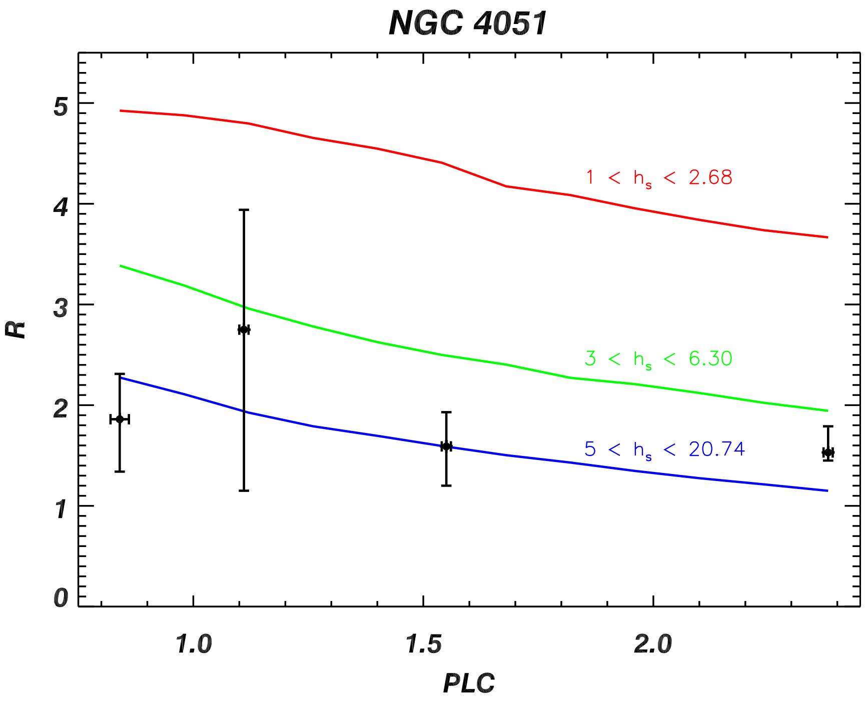

Figure 5.17: We present the relation between the reflection fraction and the power law flux in the 3-10 keV band for NGC 4051. We compared the data (black points) with the relative variations of these quantities expected from the light bending model (coloured lines), for different initial heights values. For each line, we report the corresponding range of $h_s$.

We first analyzed the entire sample with a simple model including a power law with high energy cut-off, together with a reflection component and a narrow Fe K$\alpha$ line. This analysis shows the peculiarity of two objects, namely MCG -6-30-15 and NGC 4051. A prominent reflection continuum at higher energies, parametrized with the reflection fraction $R$, was found in these sources ($R > 1$). We investigate whether this results can be explained by the presence of gravitational light bending effects. Previous works based on the analysis of *XMM-Newton* observations of these objects already revealed that the data are consistent with the light bending affecting the X-ray emission (Fabian et al. 2002, Vaughan & Fabian 2004, Ponti et al. 2006). In order to test this hypothesis, we investigate the relationship between the primary X-ray continuum and the quantities associated with the reflection component, namely the relativistic Fe line flux, its equivalent width and the reflection fraction $R$. As presented in Section 5.4.2, one of the indications of the presence of gravitational light bending is a different relation between the variations of the primary continuum and the changes in the Fe line flux (and its equivalent width), compared to what is expected when the corona is placed far from the black hole. Figures 5.10 and 5.11 show the relation between the continuum flux in the 3-10 keV band and the equivalent width of the relativistic Fe line. In the light bending model, when the variations of the relativistic Fe line flux and the reflection fraction are investigated as function of the flux in the 3 to 10 keV band, three regimes are identified, in which the behaviour is clearly different (see Figure 5.3). We also investigate the relation between the Fe line flux and the primary continuum as presented in Figures 5.12 and 5.13. We compared the data with the trends expected in the three regimes from the light bending model. The data are consistent with the sources being observed in the so-called Regime II. The subsequent analysis of the reflection fraction associated with the emission from the accretion disk (which is independent from the measure of the Fe line flux and the relativistic EW) confirms these results. From the relation between the reflection fraction and the height of the primary source $h_s$ expected from the light bending model, it was possible to estimate $h_s$ in both sources. In particular, $h_s$ is measured to be between 5 and 20 $r_g$ for MCG -6-30-15 and between 2.5 and 10 $r_g$ for NGC 4051, which correspond to the range expected from the model in the II regime. As a further independent test, we analyzed the simultaneous variations of the power law continuum flux and the reflection fraction $R$ expected from the light bending model (see Figure 5.1 and Figure 5.16) and compared this to the observed data (Figures 5.16 and 5.17). We did this by fixing the variation factor of the PLC from the observed one and for different initial values of $h_s$ (ranging from 1 to $\sim$ 15 $r_g$). The variations of height that best described the data for MCG -6-30-15 and NGC 4051 are 9 and 19 $r_g$ and 5 and 20 $r_g$, respectively, which are consistent with the values found analyzing the direct relation between the reflection fraction $R$ and the corona height.

The measurements of the corona height for these sources are in agreement with the sizes of the X-ray emitting region in AGN derived from different techniques. Microlensing observations of quasars constrained the size of the X-ray emitting region to be of the order of $\sim$ 10 $r_g$ (e.g. Chartas et al. 2002, Dai et al. 2010, Chartas et al. 2012). The analysis of soft time lags in a sample of Seyfert galaxies suggested that the X-ray sources was compact with a size of 10 $r_g$ (De Marco et al. 2013), which was later confirmed by studies of the Fe K lags (e.g. Kara et al. 2014, Uttley et al. 2014).

These results are also fully consistent with previous analysis of the same sources using *XMM-Newton* data, which proposed the presence of light bending effects in MCG -6-30-15 and NGC 4051. The presence of gravitational light bending can explain the variability of these objects and the relation between the primary X-ray continuum and several quantities of the reflection spectrum. Moreover, the *NuSTAR* data are consistent with the relativistic Fe K$\alpha$ line being produced in the inner parts of the accretion disk, with radii $< 6$ $r_g$. Thanks to the high quality data of the *NuSTAR* spectra at energies above 10 keV, it was possible to measure the reflection fraction of the emission produced from the disk with small uncertainties and convert this value into a robust estimate of the distance of the primary source above the black hole.

## 5.6 Conclusion

We analyzed *NuSTAR* archival observations of the Seyfert 1 MCG -6-30-15 and NGC 4051 galaxies. The aim of this work was to investigate the presence of gravitational light bending effects in these sources. In order to do so, we tested the spectral variability of these objects, comparing the data to the predictions of the light bending model.

The data are indeed consistent with the presence of gravitational light bending effects. Thanks to the *NuSTAR* broad energy band and its high quality data above 10 keV, it was possible to measure for the first time the variability ranges of the height of the corona above the black hole in both sources: 9-19 $r_g$ for MCG -6-30-15 and 5-20 $r_g$ for NGC 4051.

# Chapter 6

# Conclusions

The aim of this work was to investigate the relationship between the emission of both the narrow and the relativistic Fe K$\alpha$ lines and the reflection continua above 10 keV. Both these features are expected to be produced by reflection of the primary X-ray emission on neutral material, such as the accretion disk, and they should respond in the same way to the time-variation of the illuminating primary continuum (Lightman & White 1988, Haardt & Maraschi 1991, Nandra & Pounds 1994, Reynolds 1999). This is expected when the corona is located far from the black hole, where the strong gravity effects are negligible, and the geometry of the system is fixed. The study of their relationship is an important tool to probe the reflection model (George & Fabian 1991) against more complex scenarios involving absorption. We presented a systematic study of the relativistic Fe K$\alpha$ in a sample of Seyfert 1 galaxies. For this analysis, we took advantage of the extended energy band of the *Suzaku* and *NuSTAR* instruments (Mitsuda et al. 2007, Harrison et al. 2013). The spectra of the sources observed with those instruments allowed us to simultaneously fit and analyze the Fe emission lines and the Compton hump. When the reflection spectrum is produced in the inner parts of the accretion disk, close to the central black hole, strong gravity effects modify its shape. In particular, a relativistic Fe K$\alpha$ line, characterized by a broad and asymmetric profile, is produced (Fabian et al. 2000, Fabian & Miniutti 2005).

Several works statistically investigated the occurrence of such a line in samples of Seyfert 1 galaxies (Guainazzi et al. 2006, Nandra et al. 2007, de La Calle Pérez et al. 2010, Patrick et al. 2012). *XMM-Newton* and *Suzaku* provided the suitable tools for this analysis. Surprisingly, a significant fraction of sources and/or observations did not show the presence of a relativistic Fe K$\alpha$ line. In particular, this line was missing in 65% of objects in Guainazzi et al. (2006), 30% of observations in Nandra et al. (2007), 60% of sources in de La Calle Pérez et al. (2010) and 50% of objects in Patrick et al. (2012). The reason why some sources did not show this feature was poorly understood. Several hypotheses have been proposed to explain this puzzle. The results on the analysis of these samples of Seyfert 1 galaxies (Guainazzi et al. 2006, Nandra et al. 2007, de La Calle Pérez et al. 2010, Patrick et al. 2012) show that one of the main reasons for the lack of detection of a relativistic Fe line might be the low signal-to-noise ratio of the single observations.

We tested this hypothesis studying samples of AGN. If broad Fe lines are ubiquitous, but we lack detection because of low signal-to-noise ratio, we would expect higher fraction of detection in the brightest sources. Surprisingly, the bright Seyfert 1, IC 4329A was missing a relativistic Fe line component in previous *XMM-Newton* observations (Nandra et al. 2007). We therefore focused on this object, using *Suzaku* observations in order to investigate also the relation between the Fe line and the emission of the Compton hump. The analysis of the X-ray spectra shows that the relativistic Fe component is significantly detected only when the data are combined together (Mantovani et al. 2014, see also Chapter 3). This result is in agreement with the hypothesis that the high signal-to-noise ratio is important for the detection of such broad feature.

We then extended this analysis to a sample of Seyfert 1 galaxies which also did not show a relativistic Fe line component in previous *XMM-Newton* observations (Nandra et al. 2007). The aim was to investigate whether the broad line is truly absent in those sources or the lack of detection is due to the low statistics of the *XMM-Newton* observations (see Section 4.2). We systematically fitted the *Suzaku* spectra of all the sources in the sample with a series of models of varying complexity, testing the presence of relativistic Fe lines and their relation with the Compton hump. Our analysis shows that at least one observation of all the sources in our sample, and 12 out of 22 observations in total, shows a significant improvement when a relativistic line is added to the model, suggesting that this feature might be present in all the objects considered (Section 4.3.3). When the broad lines are detect in our sample, the typical equivalent widths are in the range of 50-100 eV. The overall picture shows that the relativistic Fe K$\alpha$ line is detected with high significance ($> 95\%$) only in spectra with high counts in the Fe energy band (Mantovani et al. 2016). This result is consistent with the idea that this spectral feature is ubiquitous in Seyfert 1 objects, but is, in some cases, not detected because of the low statistics.

Taking advantage of the broad band spectra of the *Suzaku* instrument, it was possible to simultaneously study the Fe line components and their associated emission at higher energies. We applied a self-consistent model (*pexmon*, Nandra et al. 2007) to the data, which reproduces the main features of the reflection spectrum produced by distant material and by the accretion disk. The latter might be affected by strong gravity effects which modify the shape of the entire spectrum, especially the profile of the Fe K$\alpha$ line (Fabian et al. 2000, Fabian & Miniutti 2005). For the vast majority of the observations (19/22), this self-consistent model gives a fit which is better than or comparable to the model where the strength of Fe line and the Compton hump flux are not linked. This shows that in general the line and reflection strengths in AGN are consistent with each other, in support of the idea that both arise from the same material (Mantovani et al. 2016, see also Chapter 4). In two cases, the self-consistent model leads to an inadequate fit, namely for MCG +8-11-11 and for one observation of IC 4239A. In MCG +8-11-11 strong evidence of a relativistic line was found, but no consistent emission above 10 keV was detected (Bianchi et al. 2010, Mantovani et al. 2016). A possible explanation for the lack of reflection in this source could be a low value of the high energy cut off (e.g. $\sim 50$ keV). This hypothesis could be tested using high energy data of higher quality, as can be expected from *NuSTAR*. The opposite situation pertains to one observation of IC 4329A. In this spectrum, strong reflection continuum was observed, while the relativistic line was not detected (Mantovani et al. 2016).

This could be due to sub-solar Fe abundance and/or variability of the geometry of the inner regions of the disk. However, a definitive interpretation remains elusive, especially when considered in context of other observations of IC 4329A with *Suzaku*. These do show both a relativistic line and a reflection continuum, with strengths consistent with each other.

Given the release of publicly available *NuSTAR* spectra on the sources of interest for this thesis, we included data from this new instrument in this work. Also in this case, we selected the Seyfert 1 objects in which a relativistic Fe line component was not detected in previous *XMM-Newton* observations (Nandra et al. 2007) using *NuSTAR* data available in the archive. The capability of this instrument to image the hard X-ray sky allows us to reduce the background above 10 keV and study the reflection spectrum with more precision. The analysis of the sample shows the peculiarity of two objects, namely MCG -6-30-15 and NGC 4051 (Section 5.3). A strong reflection continuum was detected in these sources together with broad Fe line components. These objects have been already analyzed using *XMM-Newton* observations, where they showed hints of the presence of a relativistic line and strong reflection component, through the presence of an intense Compton hump. These sources were also the first where hints of gravitational light bending were detected (Fabian et al. 2002, Vaughan & Fabian 2004, Ponti et al. 2006). Moreover, unusual behaviours between the variability of the primary X-ray continuum and the changes in the relativistic Fe K$\alpha$ line flux was observed in MCG -6-30-15 and NGC 4051 (Fabian et al. 2002, Guainazzi et al. 1998). A correlation is expected between these quantities if the primary source is sufficiently distant from the black hole and does not suffer the strong gravitational potential of the black hole. By using the broad band spectra of this revolutionary new *NuSTAR* instrument, we tested whether the X-ray emission of these sources is relativistically broadened and, in particular, we checked for the presence of light bending effects (Section 5.4.3).

We first fitted the data to investigate the presence of a relativistic Fe line component. In both sources, a strong broad Fe line was detected with average EW of 264 eV for MCG -6-30-15 and of 258 eV for NGC 4051 (Section 5.4.3). These lines are produced in the inner parts of the accretion disk at radii of $\sim 3\ r_g$ and $\sim 4\ r_g$, respectively, for the two objects. Moreover, a prominent reflection continuum was detected to be associated to these line component, parametrized with the reflection fraction $R$ ($R = 1.42 \pm 0.71$ for MCG -6-30-15 and $R = 1.93 \pm 0.98$ for NGC 4051).

In order to test the presence of light bending effects, we investigated the relationship between the variation of the primary X-ray continuum and the changes in the quantities associated to the reflection component, namely the relativistic Fe line flux, its equivalent width and the reflection fraction $R$. If the primary source is placed above the black hole at a few gravitational radii, the X-ray photons will be bent onto the disk (Miniutti & Fabian 2004). This produces an enhancement of the flux of the relativistic Fe line and a decrease of the primary X-ray flux detected at infinity. Assuming that the variability of the continuum is associated only with the variations of the corona height above the black hole placed at $2\ r_g$ from the rotating axis, it is possible to estimate the height of the primary source above the black hole. We compared the *NuSTAR* data with the trends expected in the light bending model for different ranges in corona height (Section 5.4.3, Figure 5.10 and

5.11). The analysis of the EW and the Fe line flux as functions of the primary continuum flux shows that the data are consistent with both sources being observed in the so-called II Regime (Miniutti & Fabian 2004). As a further test, we analyzed the simultaneous variations of the power law continuum flux and the reflection fraction $R$ expected from the light bending model (Section 5.4.3, Figure 5.16 and 5.17). We compared this to the observed data points. This test allowed us to measure for the first time in these objects the variations of the height of the corona above the black hole during the observations analyzed. We found that for MCG -6-30-15 the primary source is varying in the 9-19 $r_g$ range, while for NGC 4051 it is varying in the 5-20 $r_g$ range, consistently with the values expected from the light bending model to be associated with the II Regime.

The results of this work are in agreement with the predictions of the standard reflection model (George & Fabian 1991). Relativistic Fe lines are present in all Seyfert 1 objects and the reason why this feature is not always detected is mainly due to the low statistics of the single observations. Moreover, the spectra analyzed in this work showed that the strength of the reflection component is consistent with that of both the narrow and broad Fe K$\alpha$ line. This is in agreement with the idea that both arise from the same material and are parts of the same reflection spectrum. Exceptions to this picture are found in MCG -6-30-15 and NGC 4051, where gravitational light bending effects modify the expected relation between the primary X-ray flux and the reflection spectrum. We tested the light bending model predictions against the data.

Thanks to the superior sensitivity of *NuSTAR* (compared to previous studies using *XMM-Newton* data), it has been possible for the first time to derive robust constraints on the geometry and size of the X-ray emitting regions located at a few gravitational radii from the black holes.

# Bibliography

Akylas, A., Georgakakis, A., Georgantopoulos, I., Brightman, M., & Nandra, K. 2012, A&A, 546, A98

Anders, E., & Grevesse, N. 1989, Geochim. Cosmochim. Acta, 53, 197

Antonucci, R. R. J., & Miller, J. S. 1985, ApJ, 297, 621

Balbus, S. A., & Hawley, J. F. 1998, Reviews of Modern Physics, 70, 1

Ballantyne, D. R., & Fabian, A. C. 2005, ApJ, 622, L97

Ballantyne, D. R., Ross, R. R., & Fabian, A. C. 2001, MNRAS, 327, 10

Barcons, X., Mateos, S., & Ceballos, M. T. 2000, MNRAS, 316, L13

Basko, M. M. 1978, ApJ, 223, 268

Bearden, J. A. 1967, Reviews of Modern Physics, 39, 78

Beckmann, V., & Shrader, C. R. 2012, Active Galactic Nuclei

Bentz, M. C., Peterson, B. M., Netzer, H., Pogge, R. W., & Vestergaard, M. 2009, ApJ, 697, 160

Bentz, M. C., Peterson, B. M., Pogge, R. W., Vestergaard, M., & Onken, C. A. 2006, ApJ, 644, 133

Bhayani, S., & Nandra, K. 2011, MNRAS, 416, 629

Bianchi, S., Balestra, I., Matt, G., Guainazzi, M., & Perola, G. C. 2003, A&A, 402, 141

Bianchi, S., de Angelis, I., Matt, G., et al. 2010, A&A, 522, A64

Bianchi, S., Guainazzi, M., Matt, G., Fonseca Bonilla, N., & Ponti, G. 2009, A&A, 495, 421

Bianchi, S., & Matt, G. 2002, A&A, 387, 76

Bianchi, S., Matt, G., Balestra, I., Guainazzi, M., & Perola, G. C. 2004, A&A, 422, 65

Boldt, E. 1987, in IAU Symposium, Vol. 124, Observational Cosmology, ed. A. Hewitt, G. Burbidge, & L. Z. Fang, 611–615

Bondi, H. 1952, MNRAS, 112, 195

Branduardi-Raymont, G., Sako, M., Kahn, S. M., et al. 2001, A&A, 365, L140

Brenneman, L. W., Elvis, M., Krongold, Y., Liu, Y., & Mathur, S. 2012, ApJ, 744, 13

Brenneman, L. W., & Reynolds, C. S. 2006, ApJ, 652, 1028

Brenneman, L. W., Madejski, G., Fuerst, F., et al. 2014a, ApJ, 781, 83

—. 2014b, ApJ, 788, 61

Chartas, G., Agol, E., Eracleous, M., et al. 2002, ApJ, 568, 509

Chartas, G., Kochanek, C. S., Dai, X., et al. 2012, ApJ, 757, 137

Chen, M. H., Crasemann, B., & Mark, H. 1981, Phys. Rev. A, 24, 177

Clavel, J., Nandra, K., Makino, F., et al. 1992, ApJ, 393, 113

Corliss, C., & Sugar, J. 1982, Journal of Physical and Chemical Reference Data, 11, 135

Crummy, J., Fabian, A. C., Gallo, L., & Ross, R. R. 2006, MNRAS, 365, 1067

Dahari, O., & De Robertis, M. M. 1988, ApJS, 67, 249

Dai, X., Kochanek, C. S., Chartas, G., et al. 2010, ApJ, 709, 278

Dauser, T., Wilms, J., Reynolds, C. S., & Brenneman, L. W. 2010, MNRAS, 409, 1534

de La Calle Pérez, I., Longinotti, A. L., Guainazzi, M., et al. 2010, A&A, 524, A50

De Marco, B., Ponti, G., Cappi, M., et al. 2013, MNRAS, 431, 2441

De Rosa, A., Fabian, A. C., & Piro, L. 2002a, MNRAS, 334, L21

De Rosa, A., Piro, L., Fiore, F., et al. 2002b, A&A, 387, 838

Di Matteo, T. 1998, MNRAS, 299, L15

Done, C., Madejski, G. M., & Życki, P. T. 2000, ApJ, 536, 213

Dovčiak, M., Karas, V., & Yaqoob, T. 2004, ApJS, 153, 205

Eckart, A., & Genzel, R. 1996, Nature, 383, 415

Elvis, M., Wilkes, B. J., & Lockman, F. J. 1989, AJ, 97, 777

Evans, D. A., Lee, J. C., Turner, T. J., Weaver, K. A., & Marshall, H. L. 2007, ApJ, 671, 1345

Fabian, A. C., Iwasawa, K., Reynolds, C. S., & Young, A. J. 2000, PASP, 112, 1145

Fabian, A. C., Lohfink, A., Kara, E., et al. 2015, MNRAS, 451, 4375

Fabian, A. C., & Miniutti, G. 2005, ArXiv Astrophysics e-prints, astro-ph/0507409

Fabian, A. C., Rees, M. J., Stella, L., & White, N. E. 1989, MNRAS, 238, 729

Fabian, A. C., & Ross, R. R. 2010, Space Sci. Rev., 157, 167

Fabian, A. C., & Vaughan, S. 2003, MNRAS, 340, L28

Fabian, A. C., Vaughan, S., Nandra, K., et al. 2002, MNRAS, 335, L1

Fabian, A. C., Zoghbi, A., Ross, R. R., et al. 2009, Nature, 459, 540

Fermi, E., ed. 1950, Nuclear physics

Ferrarese, L., & Ford, H. 2005, Space Sci. Rev., 116, 523

Fukazawa, Y., Mizuno, T., Watanabe, S., et al. 2009, PASJ, 61, 17

Gallo, L. C. 2006, MNRAS, 368, 479

García, J., Dauser, T., Lohfink, A., et al. 2014, ApJ, 782, 76

Genzel, R., Eisenhauer, F., & Gillessen, S. 2010, Reviews of Modern Physics, 82, 3121

George, I. M., & Fabian, A. C. 1991, MNRAS, 249, 352

Ghisellini, G., Haardt, F., & Matt, G. 1994, MNRAS, 267, 743

Gliozzi, M., Titarchuk, L., Satyapal, S., Price, D., & Jang, I. 2011, ApJ, 735, 16

Gondoin, P., Barr, P., Lumb, D., et al. 2001, A&A, 378, 806

Green, A. R., McHardy, I. M., & Done, C. 1999, MNRAS, 305, 309

Greenstein, J. L., & Schmidt, M. 1964, ApJ, 140, 1

Guainazzi, M., Bianchi, S., & Dovčiak, M. 2006, Astronomische Nachrichten, 327, 1032

Guainazzi, M., Nicastro, F., Fiore, F., et al. 1998, MNRAS, 301, L1

Guainazzi, M., Matt, G., Molendi, S., et al. 1999, A&A, 341, L27

Gültekin, K., Richstone, D. O., Gebhardt, K., et al. 2009, ApJ, 698, 198

Haardt, F., & Maraschi, L. 1991, ApJ, 380, L51

Haardt, F., Maraschi, L., & Ghisellini, G. 1994, ApJ, 432, L95

Harrison, F. A., Craig, W. W., Christensen, F. E., et al. 2013, ApJ, 770, 103

House, L. L. 1969, ApJS, 18, 21

Iwasawa, K., Fabian, A. C., Young, A. J., Inoue, H., & Matsumoto, C. 1999, MNRAS, 306, L19

Iwasawa, K., Miniutti, G., & Fabian, A. C. 2004, MNRAS, 355, 1073

Iwasawa, K., Fabian, A. C., Reynolds, C. S., et al. 1996, MNRAS, 282, 1038

Kaastra, J. S., & Mewe, R. 1993, A&AS, 97, 443

Kaastra, J. S., Kriss, G. A., Cappi, M., et al. 2014, Science, 345, 64

Kara, E., Cackett, E. M., Fabian, A. C., Reynolds, C., & Uttley, P. 2014, MNRAS, 439, L26

Kaspi, S., Maoz, D., Netzer, H., et al. 2005, ApJ, 629, 61

Kaspi, S., Smith, P. S., Netzer, H., et al. 2000, ApJ, 533, 631

Kelley, R. L., Mitsuda, K., Allen, C. A., et al. 2007, PASJ, 59, 77

Khachikian, E. E., & Weedman, D. W. 1971, Astrofizika, 7, 389

Khachikian, E. Y., & Weedman, D. W. 1974, ApJ, 192, 581

Kokubun, M., Makishima, K., Takahashi, T., et al. 2007, PASJ, 59, 53

Kollatschny, W. 2003, A&A, 412, L61

Komossa, S., & Meerschweinchen, J. 2000, A&A, 354, 411

Koratkar, A. P., & Gaskell, C. M. 1991, ApJ, 370, L61

Koyama, K., Tsunemi, H., Dotani, T., et al. 2007, PASJ, 59, 23

Krolik, J. H. 1999, Active galactic nuclei : from the central black hole to the galactic environment

Krolik, J. H., & Kallman, T. R. 1987, ApJ, 320, L5

Lamer, G., McHardy, I. M., Uttley, P., & Jahoda, K. 2003, MNRAS, 338, 323

Lamer, G., Uttley, P., & McHardy, I. M. 2000, MNRAS, 319, 949

Laor, A. 1991, ApJ, 376, 90

—. 1998, ApJ, 505, L83

Lawrence, A., Watson, M. G., Pounds, K. A., & Elvis, M. 1987, Nature, 325, 694

Lee, J. C., Fabian, A. C., Brandt, W. N., Reynolds, C. S., & Iwasawa, K. 1999, MNRAS, 310, 973

Lee, J. C., Iwasawa, K., Houck, J. C., et al. 2002, ApJ, 570, L47

Lee, J. C., Ogle, P. M., Canizares, C. R., et al. 2001, ApJ, 554, L13

Leighly, K. M., Mushotzky, R. F., Yaqoob, T., Kunieda, H., & Edelson, R. 1996, ApJ, 469, 147

Lense, J., & Thirring, H. 1918, Physikalische Zeitschrift, 19, 156

Lightman, A. P., & White, T. R. 1988, ApJ, 335, 57

Lightman, A. P., & Zdziarski, A. A. 1987, ApJ, 319, 643

Liu, Y., Elvis, M., McHardy, I. M., et al. 2010, ApJ, 710, 1228

Lobban, A. P., Reeves, J. N., Porquet, D., et al. 2010, MNRAS, 408, 551

Longinotti, A. L., Bianchi, S., Santos-Lleo, M., et al. 2007, A&A, 470, 73

Lynden-Bell, D. 1969, Nature, 223, 690

Madejski, G. M., Zdziarski, A. A., Turner, T. J., et al. 1995, ApJ, 438, 672

Maeda, Y., Someya, K., & M., I. 2008, JX-ISAS

Magdziarz, P., & Zdziarski, A. A. 1995, MNRAS, 273, 837

Maiolino, R., & Rieke, G. H. 1995, ApJ, 454, 95

Mantovani, G., Nandra, K., & Ponti, G. 2014, MNRAS, 442, L95

—. 2016, MNRAS, 458, 4198

Marinucci, A., Matt, G., Miniutti, G., et al. 2014, ApJ, 787, 83

Markowitz, A., Edelson, R., & Vaughan, S. 2003a, ApJ, 598, 935

Markowitz, A., Reeves, J. N., & Braito, V. 2006, ApJ, 646, 783

Markowitz, A., Edelson, R., Vaughan, S., et al. 2003b, ApJ, 593, 96

Martocchia, A., Matt, G., & Karas, V. 2002, A&A, 383, L23

Mathews, W. G., & Capriotti, E. R. 1985, in Astrophysics of Active Galaxies and Quasi-Stellar Objects, ed. J. S. Miller, 185–233

Matsumoto, C., Inoue, H., Fabian, A. C., & Iwasawa, K. 2003, PASJ, 55, 615

Matt, G. 2000, A&A, 355, L31

—. 2002a, Philosophical Transactions of the Royal Society of London Series A, 360, 2045

—. 2002b, MNRAS, 337, 147

Matt, G., Fabian, A. C., & Reynolds, C. S. 1997, MNRAS, 289, 175

Matt, G., Fabian, A. C., & Ross, R. R. 1993, MNRAS, 262, 179

—. 1996, MNRAS, 278, 1111

Matt, G., Guainazzi, M., & Maiolino, R. 2003, MNRAS, 342, 422

Matt, G., Guainazzi, M., Perola, G. C., et al. 2001, A&A, 377, L31

Matt, G., Baloković, M., Marinucci, A., et al. 2015, MNRAS, 447, 3029

McConnell, N. J., & Ma, C.-P. 2013, ApJ, 764, 184

McHardy, I. M., Gunn, K. F., Uttley, P., & Goad, M. R. 2005, MNRAS, 359, 1469

McHardy, I. M., Koerding, E., Knigge, C., Uttley, P., & Fender, R. P. 2006, Nature, 444, 730

McHardy, I. M., Papadakis, I. E., Uttley, P., Page, M. J., & Mason, K. O. 2004, MNRAS, 348, 783

McKernan, B., & Yaqoob, T. 2004, ApJ, 608, 157

McLure, R. J., & Jarvis, M. J. 2002, MNRAS, 337, 109

Merloni, A., & Fabian, A. C. 2001, MNRAS, 328, 958

—. 2003, MNRAS, 342, 951

Meurs, E. J. A., & Wilson, A. S. 1984, A&A, 136, 206

Meyer, L., Ghez, A. M., Schödel, R., et al. 2012, Science, 338, 84

Miller, L., Turner, T. J., & Reeves, J. N. 2008, A&A, 483, 437

—. 2009, MNRAS, 399, L69

Miniutti, G., & Fabian, A. C. 2004, MNRAS, 349, 1435

Miniutti, G., Fabian, A. C., Goyder, R., & Lasenby, A. N. 2003, MNRAS, 344, L22

Miniutti, G., Fabian, A. C., Anabuki, N., et al. 2007, PASJ, 59, 315

Mitsuda, K., Bautz, M., Inoue, H., et al. 2007, PASJ, 59, 1

Molendi, S., Bianchi, S., & Matt, G. 2003, MNRAS, 343, L1

Murphy, K. D., & Yaqoob, T. 2009, MNRAS, 397, 1549

Mushotzky, R. F., Done, C., & Pounds, K. A. 1993, ARA&A, 31, 717

Nandra, K., Clavel, J., Edelson, R. A., et al. 1998, ApJ, 505, 594

Nandra, K., George, I. M., Mushotzky, R. F., Turner, T. J., & Yaqoob, T. 1997, ApJ, 477, 602

Nandra, K., Le, T., George, I. M., et al. 2000, ApJ, 544, 734

Nandra, K., O'Neill, P. M., George, I. M., & Reeves, J. N. 2007, MNRAS, 382, 194

Nandra, K., & Pounds, K. A. 1994, MNRAS, 268, 405

Noda, H., Makishima, K., Uehara, Y., Yamada, S., & Nakazawa, K. 2011, PASJ, 63, 449

Novikov, I. D., & Thorne, K. S. 1973, in Black Holes (Les Astres Occlus), ed. C. Dewitt & B. S. Dewitt, 343–450

Osterbrock, D. E. 1978, Proceedings of the National Academy of Science, 75, 540

—. 1989, Astrophysics of gaseous nebulae and active galactic nuclei

Osterbrock, D. E., & Mathews, W. G. 1986, ARA&A, 24, 171

Otani, C., Kii, T., Reynolds, C. S., et al. 1996, PASJ, 48, 211

Page, D. N., & Thorne, K. S. 1974, ApJ, 191, 499

Page, K. L., Reeves, J. N., O'Brien, P. T., & Turner, M. J. L. 2005, MNRAS, 364, 195

Palmeri, P., Mendoza, C., Kallman, T. R., & Bautista, M. A. 2003a, A&A, 403, 1175

Palmeri, P., Mendoza, C., Kallman, T. R., Bautista, M. A., & Meléndez, M. 2003b, A&A, 410, 359

Papadakis, I. E. 2004, MNRAS, 348, 207

Papadakis, I. E., & Lawrence, A. 1995, MNRAS, 272, 161

Papadakis, I. E., Petrucci, P. O., Maraschi, L., et al. 2002, ApJ, 573, 92

Parker, M. L., Marinucci, A., Brenneman, L., et al. 2014, MNRAS, 437, 721

Patrick, A. R., Reeves, J. N., Porquet, D., et al. 2012, MNRAS, 426, 2522

Perola, G. C., Matt, G., Cappi, M., et al. 2002, A&A, 389, 802

Perola, G. C., Piro, L., Altamore, A., et al. 1986, ApJ, 306, 508

Peterson, B. M. 1997, An Introduction to Active Galactic Nuclei

Peterson, B. M. 2006, in Lecture Notes in Physics, Berlin Springer Verlag, Vol. 693, Physics of Active Galactic Nuclei at all Scales, ed. D. Alloin, 77

—. 2014, Space Science Reviews, 183, 253

Peterson, B. M., Ferrarese, L., Gilbert, K. M., et al. 2004, ApJ, 613, 682

Petrucci, P.-O., Nandra, P., & Maraschi, L. 2003, in Astronomical Society of the Pacific Conference Series, Vol. 290, Active Galactic Nuclei: From Central Engine to Host Galaxy, ed. S. Collin, F. Combes, & I. Shlosman, 121

Petrucci, P. O., Haardt, F., Maraschi, L., et al. 2000, ApJ, 540, 131

Piconcelli, E., Jimenez-Bailón, E., Guainazzi, M., et al. 2005, A&A, 432, 15

Ponti, G., Miniutti, G., Cappi, M., et al. 2006, MNRAS, 368, 903

Pounds, K. A., Reeves, J. N., King, A. R., & Page, K. L. 2004, MNRAS, 350, 10

Pozdnyakov, L. A., Sobol, I. M., & Syunyaev, R. A. 1983, Astrophysics and Space Physics Reviews, 2, 189

Pringle, J. E. 1981, ARA&A, 19, 137

Protassov, R., van Dyk, D. A., Connors, A., Kashyap, V. L., & Siemiginowska, A. 2002, ApJ, 571, 545

Rees, M. J. 1984, ARA&A, 22, 471

Reeves, J. N., & Turner, M. J. L. 2000, MNRAS, 316, 234

Reynolds, C. S. 1999, in Astronomical Society of the Pacific Conference Series, Vol. 161, High Energy Processes in Accreting Black Holes, ed. J. Poutanen & R. Svensson, 178

Reynolds, C. S. 2000, ApJ, 533, 811

Reynolds, C. S., & Nowak, M. A. 2003, Phys. Rep., 377, 389

Reynolds, C. S., Wilms, J., Begelman, M. C., Staubert, R., & Kendziorra, E. 2004, MNRAS, 349, 1153

Risaliti, G., & Elvis, M. 2004, in Astrophysics and Space Science Library, Vol. 308, Supermassive Black Holes in the Distant Universe, ed. A. J. Barger, 187

Rivers, E., Markowitz, A., Rothschild, R., et al. 2014, ApJ, 786, 126

Ross, R. R., & Fabian, A. C. 1993, MNRAS, 261, 74

Rybicki, G. B., & Lightman, A. P. 1979, Radiative processes in astrophysics

Schmidt, M. 1963, Nature, 197, 1040

Schmidt, M., & Green, R. F. 1983, ApJ, 269, 352

Schnittman, J. D., Krolik, J. H., & Noble, S. C. 2013, ApJ, 769, 156

Serlemitsos, P. J., Soong, Y., Chan, K.-W., et al. 2007, PASJ, 59, 9

Seyfert, C. K. 1943, ApJ, 97, 28

Shakura, N. I., & Sunyaev, R. A. 1973, A&A, 24, 337

Shemmer, O., Romano, P., Bertram, R., et al. 2001, ApJ, 561, 162

Shih, D. C., Iwasawa, K., & Fabian, A. C. 2002, MNRAS, 333, 687

Sunyaev, R. A., & Truemper, J. 1979, Nature, 279, 506

Takahashi, T., Abe, K., Endo, M., et al. 2007, PASJ, 59, 35

Tanaka, Y., Nandra, K., Fabian, A. C., et al. 1995, Nature, 375, 659

Taylor, R. D., Uttley, P., & McHardy, I. M. 2003, MNRAS, 342, L31

Terashima, Y., Gallo, L. C., Inoue, H., et al. 2009, PASJ, 61, S299

Thorne, K. S. 1974, ApJ, 191, 507

Thorne, K. S., & Price, R. H. 1975, ApJ, 195, L101

Tombesi, F., Cappi, M., Reeves, J. N., et al. 2010, A&A, 521, A57

Treister, E., Urry, C. M., & Virani, S. 2009, ApJ, 696, 110

Treves, A., Maraschi, L., & Abramowicz, M. 1988, PASP, 100, 427

Turner, A. K., Fabian, A. C., Lee, J. C., & Vaughan, S. 2004, MNRAS, 353, 319

Turner, A. K., Fabian, A. C., Vaughan, S., & Lee, J. C. 2003, MNRAS, 346, 833

Uttley, P., Cackett, E. M., Fabian, A. C., Kara, E., & Wilkins, D. R. 2014, A&A Rev., 22, 72

Uttley, P., McHardy, I. M., Papadakis, I. E., Cagnoni, I., & Fruscione, A. 2000, MNRAS, 312, 880

Uttley, P., McHardy, I. M., Papadakis, I. E., Guainazzi, M., & Fruscione, A. 1999, MNRAS, 307, L6

Uttley, P., Taylor, R. D., McHardy, I. M., et al. 2004, MNRAS, 347, 1345

Vaughan, S., & Edelson, R. 2001, ApJ, 548, 694

Vaughan, S., & Fabian, A. C. 2004, MNRAS, 348, 1415

Vaughan, S., Fabian, A. C., & Nandra, K. 2003, MNRAS, 339, 1237

Vaughan, S., Uttley, P., Pounds, K. A., Nandra, K., & Strohmayer, T. E. 2011, MNRAS, 413, 2489

Véron-Cetty, M.-P., & Véron, P. 2001, A&A, 374, 92

Vestergaard, M., & Peterson, B. M. 2006, ApJ, 641, 689

Walton, D. J., Nardini, E., Fabian, A. C., Gallo, L. C., & Reis, R. C. 2013, MNRAS, 428, 2901

Wandel, A., Peterson, B. M., & Malkan, M. A. 1999, ApJ, 526, 579

Wilms, J., Reynolds, C. S., Begelman, M. C., et al. 2001, MNRAS, 328, L27

Wilson, A. S., & Penston, M. V. 1979, ApJ, 232, 389

Woo, J.-H., Treu, T., Barth, A. J., et al. 2010, ApJ, 716, 269

Yamaguchi, H., Nakajima, H., Koyama, K., et al. 2006, in Society of Photo-Optical Instrumentation Engineers (SPIE) Conference Series, Vol. 6266, Society of Photo-Optical Instrumentation Engineers (SPIE) Conference Series, 42

Young, A. J., Lee, J. C., Fabian, A. C., et al. 2005, ApJ, 631, 733

Zdziarski, A. A., Fabian, A. C., Nandra, K., et al. 1994, MNRAS, 269, L55

Zdziarski, A. A., Johnson, W. N., & Magdziarz, P. 1996, MNRAS, 283, 193

Zu, Y., Kochanek, C. S., & Peterson, B. M. 2011, ApJ, 735, 80

# Acknowledgements

I would like to say a few words to thank all the people who made this thesis possible and accompanied me through these years. First of all, I would like to thank Prof. Dr. Paul Nandra for giving me the opportunity to work in this environment and guide me through my PhD research. My deepest gratitude goes also to Dr. Gabriele Ponti, who was always available for discussions and taught me with enormous patience. Thanks for giving me advices through these intense years of PhD and stimulating me to finish when I needed the most.

I'm enormously grateful to my parents for their love, encouragement and help. Literally, this thesis wouldn't be finished without your help and I will always be thankful for that, because I learned that not everyone can have this kind of support form their family.

A special thanks goes to Barbara de Marco, for being not only a colleague, but also a good friend. Thanks to ”mamma” Mara Salvato for stimulating me especially in the last year of PhD and also for reminding me to bring the towel for pilates! I'm sorry not to take care of Paragon and Tintaglia again, I'm going to miss them, they are amazing! I'm also grateful to my lovely officemates. Marie thanks for creating the coffee corner in our office and providing always a piece of good chocolate! Li Ting thanks for the amazing Chinese food you prepared for us. I would like also to thank Margherita and Rob for the help in revising the english of this thesis and Torben for translating the abstract in German. Thanks to Alice for our breaks at the cantine which helped me releasing the stress of the working day (”ma son gialle cinque!”). I'm also grateful to Birgit, who was always available for helping me with the bureaucracy paperworks in German.

These years were made enjoyable in large part due to my friends, Matteo, Ale, Andrea and Lucrezia, that became part of my life here in Munich. Someone says that friends are the family that you choose, and you guys were my family here in Munich. Thanks for always being there (especially when Simone was back in Rome!) and ready to support and stimulate me to finish this PhD. I think that everyone of you helped me at least once with my poor Panda, bring me up and down to Halbergmoos or switching on the car with the cables. Matteo, I won't forget the amazing hiking and IDL coding teaching. Thanks to Ale for always being zen and helping me to see the scary situations from another point of view. Finally, I would like to thank Andrea and Lucrezia for providing excellent handmade pesto from Ligura. I won't forget Alessandro's discussions after Risiko, the poker-nights at Andrea's, Matteo's lasagna (the no-spicy one) and the arachnophobia of Lucrezia. I will keep all these memories hoping to keep in touch and see you again, maybe in Cogoleto!

A special thanks goes to my ”italian best-friends”, Sara and Francesca. I’m so grateful to still have you in my life after more than 20 years. Thank you for your moral support, I won’t forget ”keine Franziska” in my garden and Francesca saying ”Entschuldigung”. I thanks also Ornella which was always there from the high school when the professors forced us to sit together! Among the four of us, we have different lives, we don’t see each other so often, but every time I’m back in Rome it seems like the time has never passed.

Last, but not least, I would like to express my infinite gratitude to my boyfriend, Simone, who always supported me no matter what. Even if these years of distance relationship were not easy at all, you were always there for me whenever I needed you. We had our ups and downs but at the end we are still here, stronger than before. Thanks for your help and love in all the situations we faced. I will always remember our weekends in my tiny apartment, the horror movies on the couch and the amazing summer we spent together with Cheva. Thank you for everything!